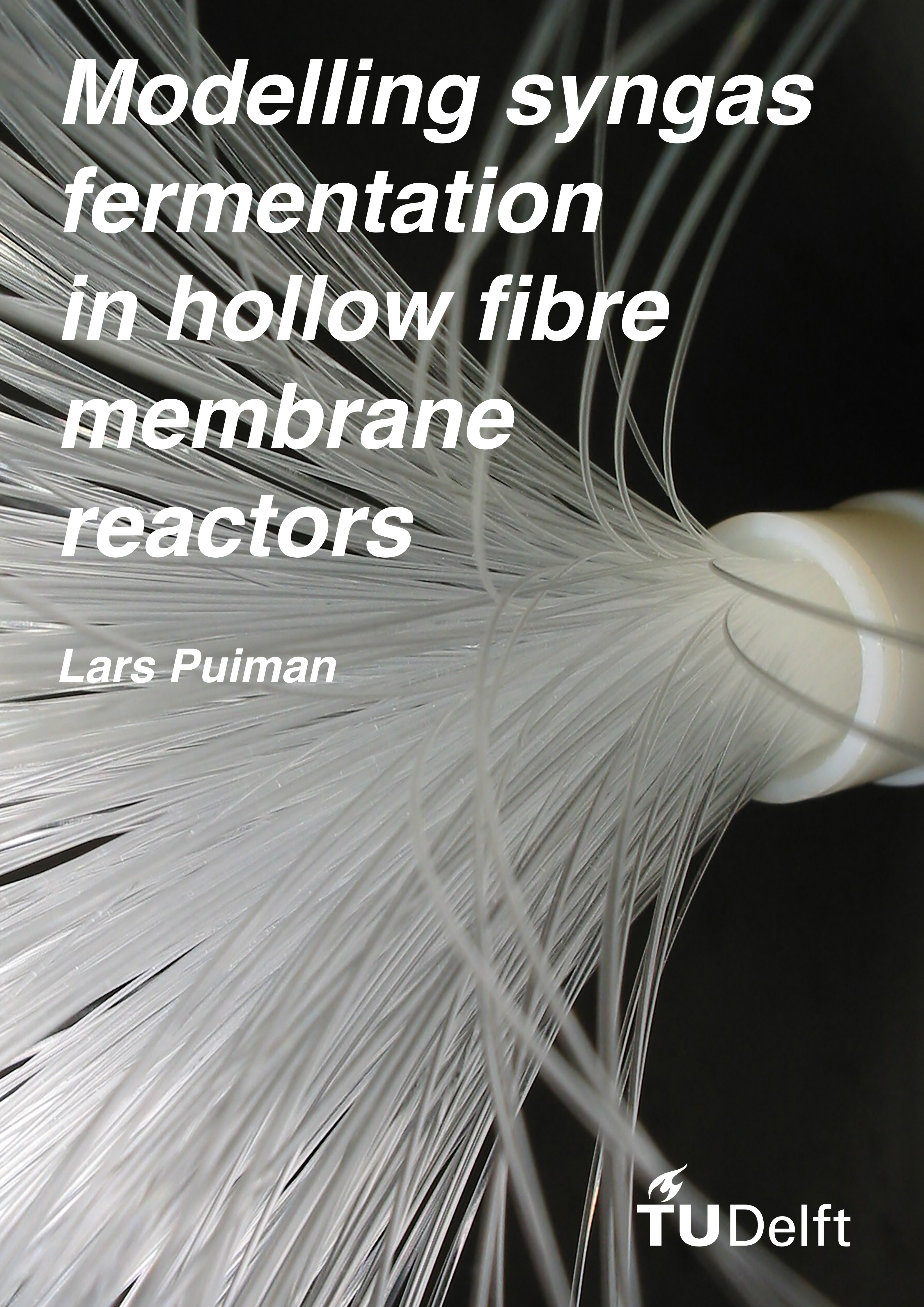

Modelling syngas fermentation in hollow fibre membrane reactors

Lars Puiman

TU Delft

Modelling syngas fermentation in hollow fibre membrane reactors

by

Lars Puiman

In partial fulfillment of the requirements for the degree of

Master of Science

in Life Science and Technology with an emphasis in Biochemical Engineering
at the Delft University of Technology,
to be defended publicly on Thursday February 20, 2020 at 02:00 PM.

Student number:	4312619	
Project duration:	August 19, 2019 – February 20, 2020	
Daily supervisor:	M. Perdigão Elisiário,	TU Delft
Thesis committee:	Dr. A. J. J. Straathof,	TU Delft, supervisor
	Dr. C. Picioreanu,	TU Delft
	Dr. L. Jourdin,	TU Delft

Abstract

Synthesis gas fermentation was recently established as a promising technology for the production of biofuels and chemicals. This is due to its potential to produce these compounds in a more sustainable and resource-efficient way than commonly used (bio-)chemical processes. The main limitations in the syngas fermentation process are the low solubility of syngas constituents (CO and H_2) in water, complicating gas-liquid mass transfer, and the limited biomass growth rate.

Hollow fibre membrane (HFM) reactors are known to have excellent mass transfer capabilities due to the large volumetric surface areas which can be obtained. Next to that, the HFM can act as support layer for a biofilm which could enable high cell densities without requiring biomass retention systems. HFM reactors are complex reactor types and can be used in multiple operational configurations. In this report, a computational model is developed to describe HFM reactors for syngas conversion to bioethanol via microbial fermentation by *Clostridium* spp.

With the development of such an model, a deep understanding was gained on the HFM reactor system and the underlying transport phenomena. This model made it possible to analyse the impact of process parameters on the volumetric productivity, the product concentration and the substrate transfer yield. With these analyses, it could be determined how these process parameters influence the syngas fermentation process from CO to ethanol.

The gas phase in the lumen was modelled first. Here, it was derived that modelling the gas phase required coupling between the gas velocity and the gas composition. Concentration and velocity differences were obtained along the axial direction of the HFM module, causing high local differences in mass transfer rates.

After implementing the membrane, it was found that these concentration differences lead to different concentrations at the membrane-biofilm interface. It was also determined that the lumen gas flow rate governs a trade-off between the mass transfer rate and mass transfer yield.

An abiotic configuration was modelled for the determination of the overall volumetric mass transfer coefficient of CO ($k_{L,CO}^{ov}a = 343\,\mathrm{h}^{-1}$), the main resistances were the membrane and, depending on the module flow rate, the liquid-side mass transfer. A biofilm attached to the membrane was modelled and compared with configurations with suspended biomass. From this analysis followed that biofilms could enable higher volumetric productivities in their respective operational windows.

Modelling a liquid recirculation reservoir showed that high ethanol concentrations could be reached (up to $35\,\mathrm{g\,L}^{-1}$). For the reservoir inflow rate, a trade-off was identified: high productivities can only be reached at low concentrations due to product inhibition.

It should be noted that these results were retrieved with a non-validated computational model and that values for some unpredictable variables as the biofilm thickness and the biomass concentration in the biofilm were assumed. Experimental model validation and justification of the assumptions are important next steps for the development and possible commercialization of syngas fermentation in HFM reactors.

Nomenclature

Latin alphabet

Symbol	Meaning	Unit
a	Specific surface area	m^{-1}
A_c	Cross sectional area	m^2
A_s	Surface area	m^2
C_S	Sutherland's constant	-
C_η	Viscosity constant	*variable*
C_{vp}	Antoine constant	*variable*
c	Concentration	$\mathrm{mol.m^{-3}}$ or $\mathrm{g.L^{-1}}$
c_x	Biomass concentration	$\mathrm{g.L^{-1}}$
d	Diameter	m
$\boldsymbol{d}$	Driving force	m^{-1}
D	Diffusion coeff.	$\mathrm{m^2.s^{-1}}$
f_B	Biofilm diffusivity ratio	-
F	Volumetric flow rate	$\mathrm{m^3.s^{-1}}$
g	Gravitational constant	$\mathrm{m^2.s^{-1}}$
H^{cp}	Henry coeff.	$\mathrm{mol\,m_l^{-3}\,atm^{-1}}$
ΔG	Gibbs free energy difference	$\mathrm{J.mol^{-1}}$
ΔH	Enthalpy difference	$\mathrm{J.mol^{-1}}$
$\Delta_{sol} H$	Dissolution enthalpy	$\mathrm{J.mol^{-1}}$
I	Inhibition constant	-
J	Flux	$\mathrm{mol.m^{-2}s^{-1}}$
k	Mass transfer coeff.	$\mathrm{m.s^{-1}}$
k_B	Boltzmann constant	$\mathrm{J.K^{-1}}$
k_L^{ov}	Overall mass transfer coeff.	$\mathrm{m.s^{-1}}$
$k_L^{ov}a$	Overall volumetric mass transfer coeff.	$\mathrm{s^{-1}}$
K^{lg}	Liquid-gas partition coeff.	$\frac{\mathrm{mol.m_l^{-3}}}{\mathrm{mol.m_g^{-3}}}$
K^{ml}	Memb.-liquid partition coeff.	$\frac{\mathrm{mol.m_m^{-3}}}{\mathrm{mol.m_l^{-3}}}$
K^{mg}	Memb.-gas partition coeff.	$\frac{\mathrm{mol.m_m^{-3}}}{\mathrm{mol.m_g^{-3}}}$
K_I	Inhibition constant	$\mathrm{mol.m^{-3}}$
K_p	Saturation constant	$\mathrm{mol.m^{-3}}$
L	Length	m
M	Molecular mass	$\mathrm{g.mol^{-1}}$
N	Number of moles	mol
N_f	Number of fibres	
n	Number of species	-
p	Absolute pressure	Pa
Δp	Pressure difference	Pa
P	Permeability	$\mathrm{m^2.s^{-1}}$
P_V	Volumetric productivity	$\mathrm{g}_i\mathrm{.L^{-1}.h^{-1}}$
P_x	Biomass productivity	$\mathrm{g}_i\mathrm{.g}_x^{-1}\mathrm{.h^{-1}}$
q	Specific rate	$\mathrm{mol}_i\mathrm{.g}_x^{-1}\mathrm{.s^{-1}}$
r	Position in radial direction	m
r_p	Particle radius	m
R	Universal gas constant	$\mathrm{J.mol^{-1}.K^{-1}}$
R	Reaction rate	$\mathrm{mol.s^{-1}}$

R^{MT}	Mass transfer resistance	s.m^{-2}
T	Temperature	K
T	Mass transfer rate	mol$_i$.m^{-3}.s^{-1}
$\boldsymbol{u}$	Convective flow vector	m.s^{-1}
u_s	Stefan velocity	m.s^{-1}
u_b	Biofilm velocity	m.s^{-1}
v	Average flow velocity	m.s^{-1}
v_{ms}	Maintenance flux	mol$_i$.mol$_x^{-1}$.s^{-1}
V	Volume	m^3
x	Mol fraction	mol$_i$.mol$_g^{-1}$
Y	Molar yield	mol$_i$.mol$_j^{-1}$
z	Position in axial direction	m

Greek alphabet

Symbol	Meaning	Unit
γ	Activity coeff.	-
η	Viscosity	Pa.s
λ_{cat}	Catabolism rate	-
μ	Growth rate	h^{-1}
ρ	Density	kg.m^{-3}
σ	Shear stress	Pa
$\sum_V$	Molecular diffusion volume	-
τ	Characteristic time	s
ϕ	Viscosity constant	-
ϕ	Packing density	-
ω	Mass fraction	kg$_i$.kg$_g^{-1}$

Sub- and superscripts

Symbol	Meaning
0	Reference
an	Anabolism
av	Average
bl,int	Biofilm-liquid interface
c	Critical
c	Characteristic
cat	Catabolism
f	Fibre
f	Formation
gm,int	Gas-membrane interface
i	First species
j	Other species
k	Location
mb,int	Membrane-biofilm interface
met	Metabolism
mod	Module
ref	Reference
R	Reaction
sol	Solubility
V	Volume
x	Biomass
$0T$	Temperature adjusted
01	Conc. and temp. adjusted
$\tilde{}$	Normalized

Phases

Symbol	Meaning
b	Biofilm
g	Lumen gas
l	Shell liquid
m	Membrane
l,res or g,res	Reservoir liquid/gas

Abbreviations

Abbreviation	Meaning
BCR	Bubble column reactor
CFD	Computational fluid dynamics
(C)STR	(Continuous) stirred tank reactor
FT	Fischer-Tropsch
HFM	Hollow fibre membrane
PBR	Packed-bed reactor
PDMS	Polydimethylsiloxane

Dimensionless numbers

Symbol	Meaning	Description
Gz	Graetz	Convection over radial diffusion
Pe	Peclet	Convection over axial diffusion
Re	Reynolds	Inert over viscous forces
Sc	Schmidt	Momentum over mass diffusivity
Sh	Sherwood	Total over diffusive mass transfer

Contents

1

Introduction

Global problems such as climate change, the depletion of fossil resources and agricultural land scarcity force humanity to shift from a fossil-based economy towards a circular, bio-based economy. Biotechnological techniques have already demonstrated their potential in decreasing greenhouse gas emissions while increasing circular resource utilization in comparison to, more conventional, petrochemical processes. For example, current techniques make it possible to produce biofuels in a sustainable way, without hampering agricultural productivity (Souza et al., 2017). Hermann et al. (2007) analyzed that significant savings in energy consumption and in greenhouse gas emissions are possible while producing bulk chemicals, with the help of biotechnological techniques. The production of renewable compounds as precursor for specialty chemicals is already commercially viable, as e.g. 1,3-propanediol, polylactic acid, succinic acid and 1,4-butanediol can be produced by sugar fermentation (Erickson et al., 2012). However, a lot of these products are produced from lignocellulosic biomass resources, which are derived from agricultural crops. Next to useful sugar-precursors as cellulose and hemicellulose, these crops contain lignin which cannot be used in fermentation processes (Williams et al., 2016). As natural biomass has an average lignin content of around 25 wt.% (Vassilev et al., 2012), there is an opportunity to increase substrate yields by developing commercial viable processes that fully utilize lignin sources (Lin and Tanaka, 2006). Recently, the development of processes which use synthesis gas (syngas) as a process intermediate emerged as a new field of research, since such processes offer the advantage of utilizing all lignocellulosic biomass as carbon source (Abubackar et al., 2011; Liew et al., 2016).

1.1. Syngas and its utilization

Syngas is a mixture with its main constituents being CO, CO_2, H_2 and N_2 and can be derived from multiple sources and can be converted into multiple products (Figure 1.1). Using thermochemical conversion, or gasification, coal, biomass and municipal solid waste streams can be converted to syngas (Klasson et al., 1992). During this process, the solids are dried first, then pyrolysis is done (solid decomposition in an inert environment between 300 and 500 °C) yielding gasses, tars and oils. At a certain moment oxidizing agents are added for the production of producer gas. After removal of the tars and oils from the producer gas, syngas is obtained. The syngas composition depends on the gasifier type, the solids source, the temperature used, and the oxidizing agents added (Munasinghe and Khanal, 2010; Abubackar et al., 2011). Other methods to produce syngas are partial oxidation of heavy liquids as fossil hydrocarbons and catalytic steam reforming of natural gas (Klasson et al., 1992). Off-gasses from steel mills contain high amounts of synthesis gas. CO_2 rich

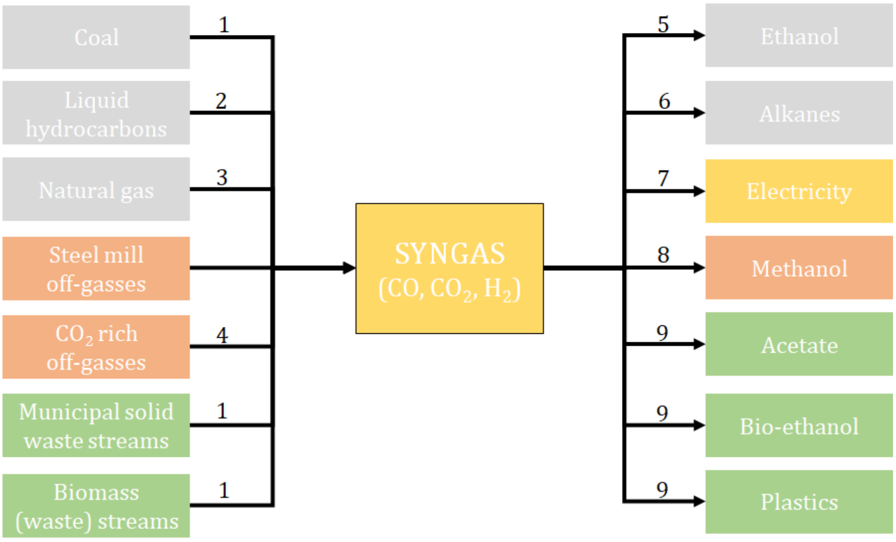

Figure 1.1: Schematic representation of the syngas sources (left), products (right) and the conversion processes. 1: gasification, 2: partial oxidation, 3: catalytic steam reforming, 4: electrolysis, 5: chemical conversion, 6: Fisher-Tropsch synthesis, 7: gas combustion, 8: methanol synthesis, 9: microbial fermentation. The grey boxes depict (petro)-chemical processes, the orange boxes industrial processes, and the green boxes biochemical processes.

off-gasses from industrial plants and water can be converted to CO and H_2, respectively, by electrolysis with (green) electricity.

After its production, syngas can be used to produce ethanol by chemical catalysis using rhodium catalysts (Lopez et al., 2015). With the Fischer-Tropsch (FT) process, syngas can be converted to alkanes, and subsequently to fuels as diesel and jet fuel (Ail and Dasappa, 2016). Syngas combustion in gas engines can be used for electricity generation (McKendry, 2002). Methanol and dimethyl ether are conventionally produced from syngas (Galadima and Muraza, 2015). In 1987, it was found that acetogenic bacteria are able to ferment synthesis gas into acetate and ethanol (Klasson et al., 1992). Lastly, micro-organisms have been found that are able to ferment synthesis gas into precursors of bioplastics (Drzyzga et al., 2015).

Bio-ethanol can be used, amongst others, as an additive to gasoline in combustion engines of cars. This way, greenhouse-gas emissions can be reduced as well as the emission of other environmental pollutants, like nitrogen oxides (Abubackar et al., 2011). The increasing market for ethanol as a biofuel (Brown, 2015), makes the sustainable production of ethanol an industrial and societal relevant research topic.

1.2. Syngas fermentation

Syngas can be fermented by acetogenic bacteria as *Clostridium ljungdahlii* (which was named after Dr. Lars Ljungdahl) (Klasson et al., 1992) or *C. autoethanogenum* (Abrini et al., 1994; Liew et al., 2016). These organisms convert syngas constituents anaerobically to ethanol (solventogenesis) or acetate (acidogenesis). The metabolic pathway (Figure 1.2) used for this conversion is the *Wood-Ljungdahl* pathway, which was by Fast and Papoutsakis (2012) determined to be "the most efficient non-photosynthetic carbon fixation mechanism" (Liew et al., 2016). Both CO and CO_2 can act as substrate in this pathway. The use of CO_2 requires an additional reduction step, for which reducing equivalents provided by H_2 hydrogenase can be used. In this pathway acetyl-CoA is produced from syngas (Abubackar et al., 2011; Liew et al., 2016).

During acidogenesis (which is coupled to cell growth), acetyl-CoA is converted to acetate and acetic acid. During solventogenesis, acetyl-CoA and acetic acid can be reduced to ethanol (Abubackar et al., 2011; Liew et al., 2016). The overall biochemical reactions (Figure 1.2) for both solventogenesis and acidogenesis depend

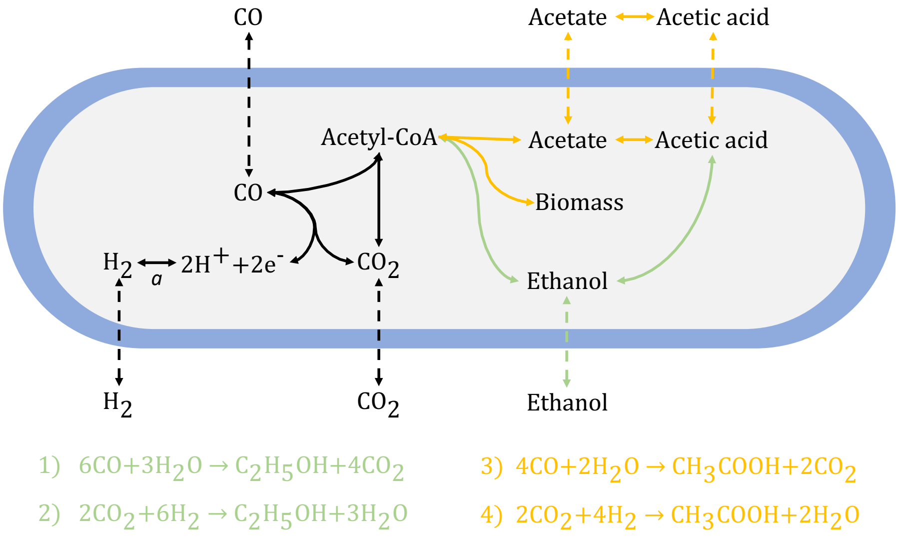

Figure 1.2: Schematic representation of the metabolism of acetogenic syngas fermenting organisms. The Wood-Ljungdahl pathway is depicted with black arrows. The arrows and the reactions for growth and acidogenesis reactions are displayed in yellow, while solventogenesis is depicted in green. Reactions 1 and 3 describe the case wherein only CO is present, while reactions 2 and 4 are valid in absence of CO. *a* depicts the H_2 hydrogenase enzyme. This figure has been adapted from Richter et al. (2016).

on the composition of the provided syngas (Liew et al., 2016). The shift from acidogenesis to solventogenesis is regulated by several factors, such as the medium pH and the presence of nutrients required for growth (Abubackar et al., 2011; Richter et al., 2016). With the help of strain evolution, these organisms can be adapted for commercial purposes, for example Molitor et al. (2016) stated that an ethanol productivity of $10\,\mathrm{g\,L^{-1}\,h^{-1}}$ could be reached.

One of the advantages of working with these organisms and their metabolic pathway is the wide substrate range they use, as they are also able to ferment sugars as glucose and xylose. Other advantages are their ability to work with different compositions of syngas and their tolerance to contaminants in producer gas (such as sulfur and tars) (Abubackar et al., 2011). The anaerobic environment decreases the probability of biological contamination and avoids flammability issues as syngas is a combustible gas (Liew et al., 2016).

Compared to the chemical conversion processes, microbial fermentation of syngas offers several advantages: (1) fermentations can be operated at ambient temperatures and pressure, (2) microbes are cheap catalysts which are resistant to contaminants, (3) no fixed ratio between CO and H_2 is required (as in the FT process), (4) microbes have higher specificity and lead to higher yields, and (5) biological conversions are irreversible. These advantages offer syngas fermentation the potential to become more attractive and environmental-friendly than the competing chemical processes for the production of fuels from syngas (Klasson et al., 1992; Munasinghe and Khanal, 2010; Abubackar et al., 2011).

Compared to the more traditional sugar-based ethanol fermentation, syngas fermentation offers some advantages: (1) potential increased substrate yields as lignin could be converted into ethanol, (2) the elimination of complex pretreatment steps to separate the lignin from biomass resources, and (3) the elimination of dedicated agricultural crop production sites as syngas fermentation could also be done using municipal solid waste or industrial off-gasses. All these advantages raised the interests for developing bioreactors for efficient ethanol production by syngas fermentation (Munasinghe and Khanal, 2010; Abubackar et al., 2011; Yasin et al., 2014).

The main bottlenecks observed in syngas fermentation are the low solubility of CO and H_2 in water, and the low growth rate of acetogens (Klasson et al., 1991; Yasin et al., 2019; Liew et al., 2016). The poor solubility hampers the transfer of these gasses to the micro-organism resulting in low dissolved gas concentrations. The low growth rate causes that biomass retention systems are necessary to obtain high biomass concentrations and to increase the conversion rate. These two factors cause a poor syngas mass transfer rate and the volumetric productivity. One other limitation of syngas fermentation is product inhibition. Solventogenic products (e.g. ethanol and butanol) are found to be inhibitory for *Clostridium spp.*, emphasizing the need for (in-situ) product removal (Huffer et al., 2011). Finally, there is a limited viable product spectrum for syngas fermentation: Only high titers of low-value products like ethanol and acetic acid were achieved. Higher value products like caproate, butyrate, butanol and hexanol are also achievable with co-cultures, but this is a very immature technology (Diender et al., 2016).

Piccolo and Bezzo (2009) performed a techno-economic analysis and stated that at that moment, the technology of biomass gasification combined with syngas fermentation was not mature enough to become profitable: Their ethanol selling price was estimated to be €1.20/L. Benalcázar et al. (2017) calculated the minimum selling price for ethanol production from different lignocellulosic biomass sources via gasification and syngas fermentation. They obtained a minimum selling price of $2/kg ethanol. At this moment, the market price of ethanol is around $0.5/kg, which means that this process is not profitable yet. Both techno-economic analyses suggested that process engineering methods (improving the yield, increasing the gas-liquid mass transfer rate and process intensification) could lead to profitable business cases (Piccolo and Bezzo, 2009; Benalcázar et al., 2017). Therefore, several reactor configurations have been used to increase the syngas mass transfer rate and to achieve high volumetric productivities (Yasin et al., 2015; Asimakopoulos et al., 2018).

1.3. Reactors for syngas fermentation

Several reactor configurations have been used for syngas fermentations. The best known reactor types for syngas fermentation are stirred tank reactors (STR), bubble column reactors (BCR), trickle bed reactors (TBR) and hollow fibre membrane (HFM) reactors (Figure 1.3), for these reactors some advantages and disadvantages are discussed. The reactors types can be compared in terms of the overall volumetric gas-liquid mass transfer coefficient k_L^{ov} and the ethanol productivity $P_{V,\text{EtOH}}$ (Table 1.1). Next to these, some less frequently used reactor types will shortly be discussed.

The STR is the most frequently studied reactor for syngas fermentation. This is due to its ease of use in lab-scale settings, and as it is the best choice for studying metabolic characteristics of micro-organisms (Yasin et al., 2019). Gas-liquid mass transfer is due to dispersion and break-up of syngas bubbles by the rotating impeller. However, for industrial use this is a less suitable technique as high stirrer speeds are required to

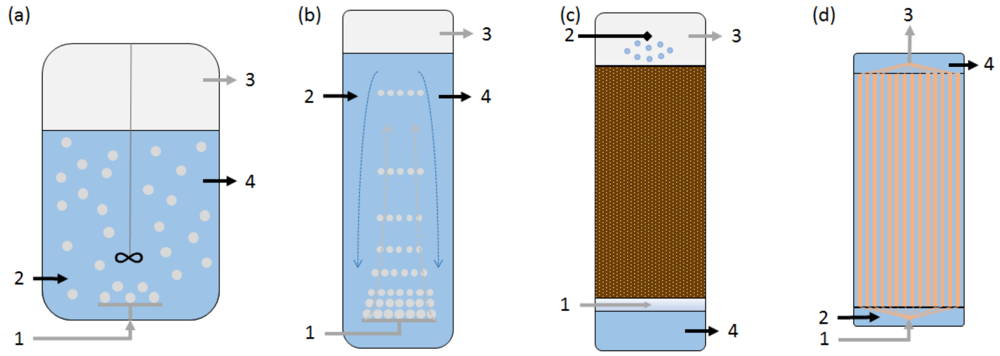

Figure 1.3: Schematic representation of different reactor systems studied in literature: (a) STR, (b) BCR, (c) TBR with a brown bed, (d) HFM reactor with the hollow fibre membranes in orange. The numbered arrows denote the gas (grey) and liquid (black) inlets (1 and 2) and the gas and liquid outlets (3 and 4).

Table 1.1: Comparison of different reactor types used for syngas fermentation in terms of possible advantages, disadvantages, mass transfer coefficient and ethanol productivity. Note that this is a general comparison and that the mass transfer rates and productivities were not obtained in the same experiments.

Reactor type	Advantages	Disadvantages	k_L^{ov} (h^{-1})	$P_{V,\mathrm{EtOH}}$ (gL^{-1}h^{-1})
STR	- Easy to use - Most studied configuration for syngas conversion	- High operational costs - Poor mixing in industrial tanks	10 - 500^{a}	0.0782^{c,d}
BCR	- High mass transfer area - Low capital and operational costs - Commercial use by LanzaTech	- Backmixing at high flow rates - Possible bubble coalescence	18 - 860^{a}	0.0642^{e}
TBR	- No agitation required - Plug flow behavior	- Difficult scale up - Small working volume and low production capacity	36 - 360^{a}	0.1578^{b,c}
HFM reactor	- Low energy consumption - High surface area - Easy scale up	- Pore-wetting or clogging - High replacement costs - High infrastructure and pumping costs	Up to 1096^{b}	0.143^{c,g}

a) Bredwell et al. (1999), b) Shen et al. (2014b). Note that it is not straightforward to compare k_L^{ov} values of HFM reactors (Yasin et al., 2019).
c) Asimakopoulos et al. (2018), d) Mohammadi et al. (2012), e) Shen et al. (2014a), f) Devarapalli et al. (2017), g) Shen et al. (2014b)

maintain high k_L^{ov} values. This leads to high power requirement and therefore large operational costs. Next to this, in large industrial tanks, mixing will be poor so that there will be large local differences in mass transfer and reaction rates (Abubackar et al., 2011; Yasin et al., 2015).

In a BCR, small gas bubbles are sparged from the bottom of the reactor. The density difference between the gas and liquid lets the bubbles rise. The bubble rising causes mixing in the liquid phase. As the bubble diameter is very low, the bubble volumetric surface area is large, so that high mass transfer rates can be achieved. This mass transfer rate is generally higher than in STR reactors. There will be back-mixing at larger flow rates and bubble coalescence can decrease the mass transfer rate. The simple design and the lack of moving parts in this system decreases the capital and operational costs (Munasinghe and Khanal, 2010; Abubackar et al., 2011; Yasin et al., 2019). The gas-lift reactor is a type of bubble column reactor, but with dedicated riser and downcomer areas (Yasin et al., 2019). It has been known that LanzaTech, the only company that successfully commercialized syngas fermentation by converting syngas from steel mills into ethanol with a proprietary *C. autoethanogenum* strain, uses these types of reactors for their processes (Valgepea et al., 2018; Chen et al., 2018; Yasin et al., 2019).

A TBR reactor most often consists of a counter-current gas-liquid phase over a solid bed of biomass and its carrier material. The liquid is trickled over the bed at the top, while the gas is supplied from the bottom. This liquid trickling causes a very thin liquid film layer that is in contact with the gas, minimizing the liquid phase mass transfer resistance (Orgill et al., 2013). The mass transfer rate is dominated by the packing size, the liquid recirculation rate and the gas flow rate (Abubackar et al., 2011). This set up was tested by Klasson et al. (1992) and he achieved higher productivities and CO conversion rates than in STR and BCR. Compared to STR's the power consumption is lower as no mechanical agitation is required, but the k_L^{ov} achieved is smaller than in a BCR (Bredwell et al., 1999; Munasinghe and Khanal, 2010). The main limitation of TBR is the low working volume (only 20% of the reactor was used), which decreases the production capacity and makes scale up difficult (Yasin et al., 2019).

Hollow fibre membranes (HFM) are often used for gas-liquid contacting applications due to the high volumetric surface areas that can be reached (Drioli et al., 2006). For syngas fermentations they can be used in different ways. Bredwell et al. (1999) used them for retaining biomass in the reactor. They can also be used in a submerged setup, so that they are effectively used as sparger, leading to energy savings (Yasin et al., 2015). Next to this, they can be used as biofilm carrier so that high cell concentrations can be reached (Reij et al., 1998; Abubackar et al., 2011). The continuous feed supply to the biofilm, offers potential for high yields and reaction rates (Munasinghe and Khanal, 2010). Shen et al. (2014b) used an external HFM reactor with biofilm growth and achieved higher substrate utilization efficiencies and productivities than in a BCR. This way, Anggraini et al. (2019) also achieved higher ethanol titers and yields compared to a STR. Potential disadvantages are the high replacement costs due to membrane and biofilm aging (Reij et al., 1998), possible pore clogging and -wetting and high operational costs for infrastructure and pumping to provide liquid recirculation (Yasin et al., 2019).

Some other reactors studied before are the moving bed biofilm reactor (Abubackar et al., 2011): Biomass is retained on a carrier (as in the trickle bed) and gas and liquid are added from the bottom, causing some turbulence and mixing. Shen et al. (2014a) examined syngas fermentation in a monolithic biofilm reactor, they achieved a higher k_L^{ov} and ethanol productivity ($0.0979\,\mathrm{g_{EtOH}\,L^{-1}\,h^{-1}}$) than in a BCR. Later, Shen et al. (2017) investigated the use of a rotating packed bed reactor, but found a lower k_L^{ov}, but a higher productivity ($0.279\,\mathrm{g_{EtOH}\,L^{-1}\,h^{-1}}$) than in a BCR. Most recently, Sathish et al. (2019) used a bulk-gas-to-atomized-liquid reactor. Using a spraying nozzle, they were able to saturate very small bubbles of liquid medium with syngas and achieved a k_L^{ov} of $3600\,\mathrm{h^{-1}}$ and an ethanol productivity of $0.746\,\mathrm{g\,L^{-1}\,h^{-1}}$. These configurations sound very promising, but scale-up of these configurations is not straightforward and therefore their industrial applicability can be disputed.

After considering all the advantages and disadvantages of the discussed reactor types, the HFM reactor emerges as an interesting configuration for syngas fermentation. This is due to the combination of the high mass transfer potential together with possible biomass retention in a biofilm and the ease of scale up.

1.4. Hollow fibre membrane reactors

As the HFM reactor offers potential for industrial syngas fermentation to ethanol, some additional research was done for these reactors. A HFM reactor can be operated in a multiple ways. An outside-in configuration can be used, wherein the gas flows through the shell and the liquid through the lumen (i.e. fibres). To prevent biofouling and resulting flow maldistributions and high pressure drops in the lumen side, the inside-out configuration is preferred: Gas flows through the lumen while the fermentation broth flows through the shell side (Yasin et al., 2015). In most cases in literature, the inside-out configuration was used (Yasin et al., 2015).

From the lumen, the syngas diffuses through the membrane, to which a biofilm can be attached to convert the syngas. The gasses will subsequently be consumed in the biofilm. In case of incomplete consumption, they also enter the liquid phase (Kumar et al., 2008; Atchariyawut et al., 2008). Using a reservoir, the broth can be recycled, enabling mixing, industrial flexibility and more control of process parameters. The lumen can be operated in open- or dead-end mode (Yasin et al., 2015), while the liquid phase can be operated in co-current, counter-current and in cross flow mode (Orgill et al., 2013; Robert et al., 2014).

Membrane types

Next to this, for gas-liquid membrane contacting, there are three different types of membranes which have been extensively described: (micro)porous, dense and composite membranes. For all these types, it can be chosen to use hydrophobic or hydrophilic membranes. Hydrophilic membranes can cause wetting or biofouling problems, which could reduce the mass transfer rate compared to hydrophobic membranes as these do not lead to wetting or biofouling problems (Orgill et al., 2013; Yasin et al., 2015).

Porous membranes can be divided in a class of microporous, mesoporous and macroporous membranes. The main difference between these membranes is their pore size, these differ, respectively, from smaller than 2 nm, to 2-50 nm to larger than 500 nm. The pores are deliberately filled with gas, so that gaseous compounds are able to diffuse through the pores to the liquid. With the pore size, the selectivity of the membrane can be tuned. But most often, porous membranes are used when selectivity is not required (Reij et al., 1998). Porous membranes are made of a polymer matrix (such polypropylene or Teflon) and have a thickness in the range of 30 to 100 μm (Reij et al., 1998).

Dense membranes are membranes with a thick polymer layer of materials like PDMS (polydimethylsiloxane) or polypropylene. Membrane thickness is between 100 μm and 1 mm (Reij et al., 1998). Their dense nature enables better resistance to higher pressures than porous membranes (Kumar et al., 2008). Dense membranes are more selective than porous membranes as all compounds need to permeate through the membrane. Compounds with low permeability (i.e. the product of membrane diffusivity and solubility) permeate in a lesser extent than compounds with higher permeability (Reij et al., 1998; Kumar et al., 2008).

Composite membranes are a combination of porous and dense membranes. This way,the best characteristics of both types of membranes are merged. A porous layer is used to achieve high mass transfer rates, while a thin dense layer (between 1 and 30 μm) is used for selectivity and biofilm support. To prevent wetting and biofouling, the porous layer should be used at the gas side (Kumar et al., 2008).

When selecting the right type of membrane in a HFM reactor, mechanical strength, permeability and selectivity needs to be balanced (Kumar et al., 2008). It was chosen to work with a dense, hydrophobic, PDMS membrane, as PDMS offers high permeability for syngas constituents (especially CO_2) and as commercial PDMS membrane modules are available. Although porous membranes would lead to higher mass transfer rates, membranes biofouling and pore wetting problems are prevented due to the use of dense membranes.

Modelling process parameters

In the HFM reactor configuration, there is a variety of process parameters which influence should be determined to enhance process performance: gas pressure, gas flow velocity and composition, the shell liquid flow pattern and inflow rate, reservoir inflow rate, membrane parameters like thickness, material and type (porous, dense or composite), and reactor parameters like fibre length, fibre diameter, spacing and total fibre number. All these parameters can be adjusted in order to tune the reactor performance.

With a computational model of a lab-scale HFM reactor, the influence of these process parameters on the process performance can be determined. This could lead to development of HFM reactors with higher productivity or conversion yields. An ideal window of operation can be derived by assessing possible trade-offs between productivity, titer and yield. A model can also enable comparison with other reactor types and guide scale-up. During the development of a model, the underlying transport phenomena will be determined, which will lead to a deeper understanding of these phenomena inside HFM reactors.

In literature, several computational models have been developed to assess mass transfer in membrane reactors. However, some models do not incorporate biomass formation (Kavousi et al., 2016; Orgill et al., 2019) or do not specify membrane characteristics (Atchariyawut et al., 2008). Next to these, some scholars present models that are developed by fitting experimental data in order to determine mass transfer coefficients (Munasinghe and Khanal, 2012; Orgill et al., 2013), an approach with little external validity. More comprehensive models were developed incorporating membranes and biofilms, but are not designed for syngas fermentation, but instead for wastewater treatment (Pavasant et al., 1996; Freitas Dos Santos et al., 1997; Ahmadi Motlagh et al., 2006; Matsumoto et al., 2007) and hydrogen-based denitrification (Martin et al., 2013, 2015). Edel et al. (2019) developed a simple 1D model for syngas fermentation to acetate in membrane reactors with attached biofilms. They conclude from their model that the biofilm thickness and the biomass concentration in the biofilm are the most important values that influence the productivity of the reactor.

1.5. Project scope

No comprehensive model has been developed for syngas fermentation to ethanol in a HFM reactor, thus far. Such a model can be used to assess the influence of process parameters on the performance of the HFM reactor. The performance of the reactor can be measured in terms of ethanol yield ($\mathrm{mol\,mol_{CO}^{-1}}$), productivity ($\mathrm{g L^{-1}\,h^{-1}}$), substrate utilization efficiency (%) and product concentration ($\mathrm{g L^{-1}}$).

In this master thesis, it is examined how the process parameters affect the performance of the syngas fermentation process and how they can be used to derive an ideal window of operation. By mathematical modelling, mass transfer characteristics and consumption and production patterns of CO, CO_2, H_2, biomass and ethanol, will be described, along the gas, membrane, biofilm, liquid phases and the reservoir. Furthermore, suggestions to validate the model will be delivered. This leads to the following research questions:

What is the impact of different input process parameters of a hollow fibre membrane biofilm reactor on the performance of the syngas fermentation process and how can they be used to improve the reactor performance? How can these effects be experimentally validated?

1.6. Thesis approach

Some initial choices were made prior to modelling the HFM module. An inside-out feed configuration was modelled: Syngas is provided through the lumen and the liquid flows through the shell. Co-current liquid and gas flow was used. Counter and co-current flow were not examined as it was hypothesized that the liquid and gas flow never contain the same compound that needs to be transferred. This means that the driving force over the membrane will never be harmed by the presence of the same compound in the liquid phase, as it is expected to be consumed in most of the cases.

The same lab-scale HFM module was used. Therefore, the dimensions and membrane properties were kept constant. This imposes consistency along different models and enables comparison between these models. The membrane module used was a dense hydrophobic PDMS membrane. A liquid recirculation reservoir was incorporated in the model. Isothermal, adiabatic conditions and a constant pH were assumed.

As both mass transfer and gas and liquid flow needs to be modelled, computational fluid dynamics (CFD) must be used to model the HFM reactor. In Chapter 2, the geometry, basic transport phenomena and equations which describe the HFM reactor model, are provided. In the subsequent chapters the model is consecutively developed, based on examined model results and operational conditions. In Chapter 3, the gas compartment is analyzed. It will be determined how syngas is transferred in the gas phase and from the gas phase through the membrane. Chapter 4 focuses on the membrane and its effect on the concentration of syngas species. In Chapter 5 the overall mass transfer coefficient is examined and the performance of the HFM reactor is evaluated in cases with and without biofilm formation. Then, in Chapter 6, the reservoir is implemented and its effect on the overall reactor system is discussed.

After completion of the model, the effect of the process parameters on the reactor performance is studied in Chapter 7. In this chapter, also operational trade-offs were analyzed and a sensitivity analysis was performed for assumed parameters. Suggestions for validation of the computational model are provided in Chapter 8. Future perspectives and conclusion is given in Chapters 9 and 10. In Appendix A, an overview is provided of the different models used in the different chapters. This overview includes a scheme which indicates the species and compartments that are included in these models.

2

Model description

In this chapter, the approach used for modelling the HFM reactor is described in detail. First, the geometry and the underlying assumptions which were made while modelling the HFM reactor is discussed. The relevant transport phenomena in the HFM module are then described. The equations and boundary conditions are explained that were used for solving this model. Lastly, the modelling method is explained as well as the different steps taken while modelling the system.

2.1. Model geometry

In Figure 2.1, some model geometries are depicted that could be used for modelling a HFM reactor. A 2D-axisymmetric configuration for the HFM module was used as this requires less computational effort than a 3D geometry of the whole module or of a single fibre and it provides the detailed radial and axial gradients which cannot be provided by 1D models.

Limitations of this geometry compared to a 3D whole module geometry are that the liquid flow pattern around the fibres could not be investigated and that the effect of the amount of fibres and their spacing is more difficult to investigate. However, for both modules needs to be assumed that all fibres are equally spaced and that a hexagonal or honeycomb structure can be maintained over the module length, which is in practice not achievable.

When modelling one single fibre, it needs to be assumed that the modelled fibre is representative for all fibres in the membrane module. This leads to subsequent assumptions that the gas flow rate and composition is equal in all fibres and that there is no maldistribution in liquid flow velocity. Kavousi et al. (2016) found, while modelling 3D HFM modules, that the flow velocity is high near the walls (as they placed no fibres there) and low between the fibres. However, it has been assumed that in the model used no such distributions in liquid flow pattern exists and that there is only laminar, unidirectional flow.

In a 2D-axissymetric geometry (Figure 2.1c), a symmetry axis is imposed in the middle of the fibre. This axisymmetric model makes it possible to develop 3D patterns around the fibre as it assumes that there is an equal distribution of all properties in the azimuthal direction. This also means that the surface areas at the interfaces, such as $A^{\text{int}}_{s,gm}$ and $A^{\text{int}}_{s,mb}$. In the case a planar 2D geometry would be used, these characteristics would not be taken into account.

In the case a 1D model would be used, one can only model transport phenomena in one direction. As differences in concentrations in the axial direction in the liquid and gas phases and in the radial direction in

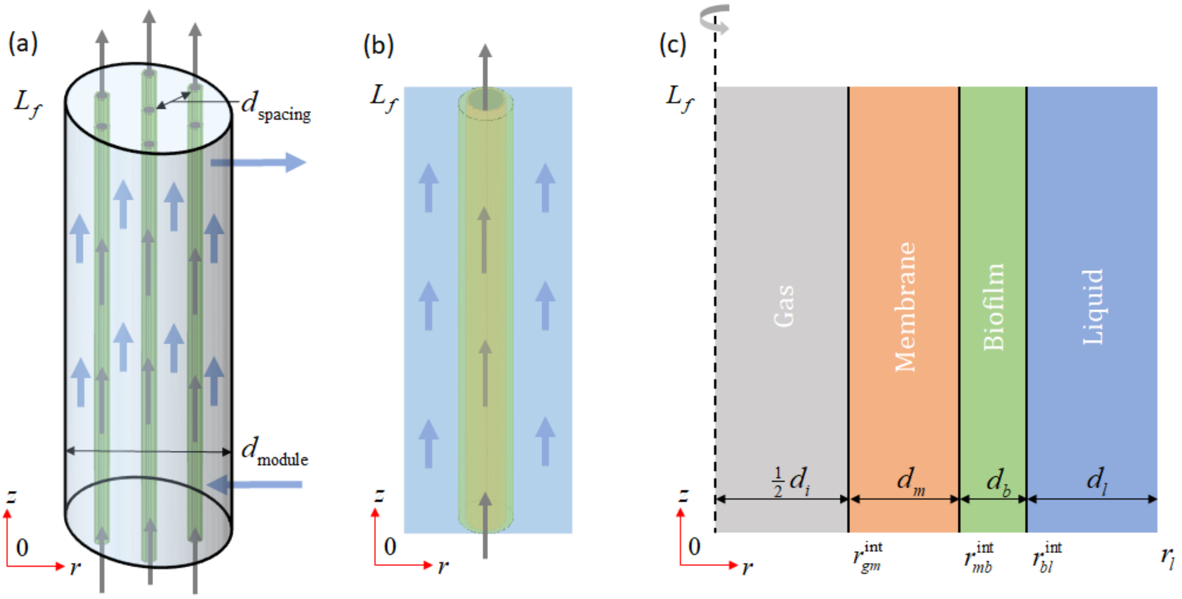

Figure 2.1: Schematic configurations used for designing the model of the HFM module. The schematic in (a) represents a 3D module of a HFM system with seven fibres, although the module used has 550 fibres. (b) depicts the approximation of this system, but with modelling only 1 fibre in 3D. (c) depicts the 2D axisymmetric system which was eventually used for modelling this system.

the membrane, biofilm and liquid phases are expected, this kind of model was considered to be inadequate for modelling a HFM reactor in detail.

The reservoir was described as a continuous STR. Assuming ideal mixing enables modelling the reservoir as a single point (or 0D), so that no dedicated geometry for the reservoir needs to be developed.

2.2. Transport phenomena

A schematic overview of the whole reactor system is provided in Figure 2.2a. For the HFM module, the most important transport phenomena were derived and depicted in Figure 2.2b. These transport phenomena were derived based on initial calculations of the characteristic times of these phenomena (see Appendix B). In the gas and liquid phases, radial diffusion and axial convection were considered, while in the membrane and biofilm only radial diffusion was taken into account for solutes transport. Partition was imposed between the gas phase and the membrane and the membrane and the biofilm, it was assumed that partition between membrane and biofilm can be described with the same partition function as partition between membrane and liquid. Fluxes are depicted for species transport across interfaces and the notations used for concentrations in the phases.

For both the HFM module and the reservoir, the inflow and outflow streams are provided, which were used to couple both. Nitrogen gas is purged into the reservoir via a separate gas inflow in order to prevent accumulation of dissolved gasses. A 4 °C gas condenser is added to the gas outlet to limit evaporation of water and ethanol.

2.3. Model equations

The modelled HFM module was based on initial specifications provided by OxyMem, the supplier of the membrane module. The most important membrane specifications are given in Table 2.1. A detailed picture of the model geometry combined with locations and values of parameters as the surface areas, cross sectional areas and locations of the geometry in the model are provided in Appendix C.

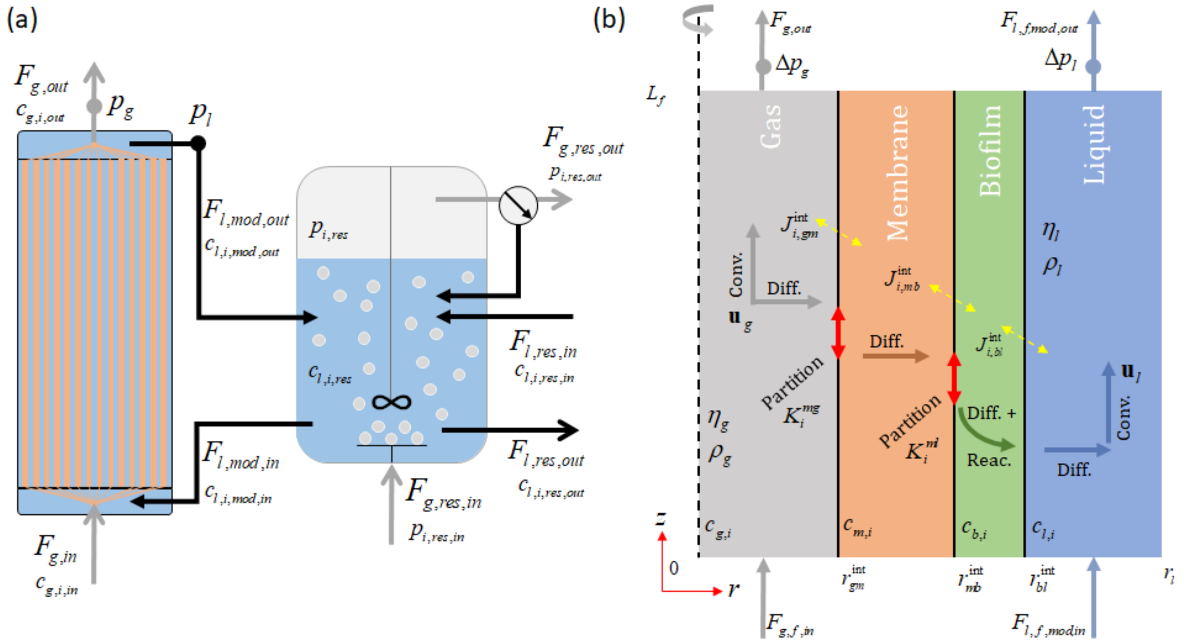

Figure 2.2: Schematic overview of (a) the lab-scale set up of a HFM module with a liquid recirculation reservoir. The symbols for the most important parameters of this system are depicted in this scheme. In (b) an overview is provided of the most important transport phenomena in the HFM module, together with their symbols.

In this section, the equations used for modelling the HFM module and the reservoir are provided. All non-compound-specific parameters used are provided in Table 2.1, while parameters which differ per compound are provided in Table 2.2. Some parameters were derived from literature, others were assumed, or have a flexible range of operation. In several cases, initial calculations were necessary to derive the values of these parameters, these calculations are provided in the mentioned appendix section. First the material balances for the chemical species are described for all compartments in the HFM module, after which the balances are described that govern liquid and gas flow in the HFM module. In the last subsection, the equations behind the liquid recirculation reservoir are described.

2.3.1. Species material balances

Chemical species transport in the gas phase is governed by axial convection and radial diffusion (Equation 2.1). The density and the concentration change as result of composition changes, by assuming ideal gas behaviour (Equation 2.2). Diffusion was described with Maxwell-Stefan diffusion (Equation 2.3) as the gas species molar fractions were considered to be in the same order of magnitude as there is no gaseous solvent. This lack of solvent, makes it impossible to model gas phase diffusion with Fick's law (Krishna and Wesselingh, 1997). For calculating the diffusive flux (Equation 2.3), it was assumed that the sum of the diffusive fluxes $J^{\text{diff}}_{g,i}$ and the sum of the driving forces $\boldsymbol{d_j}$, is 0 (Bothe, 2011). As reference compound, the compound with the largest mole fraction was used. The diffusion coefficients were the Maxwell-Stefan diffusion coefficients (see Appendix D.1). Thermal diffusion coefficients were not taken into account, as isothermal conditions were assumed.

$$\frac{\partial c_{g,i}}{\partial t} = -\boldsymbol{u_g} \cdot \nabla c_{g,i} - \nabla \cdot J^{\text{diff}}_{g,i} \tag{2.1}$$

$$\rho_g = \frac{p_g}{RT} M_{av} = \frac{p_g}{RT} \left(\sum_{i=1}^{n} \frac{\omega_{g,i}}{M_i} \right)^{-1} \quad \text{and} \quad c_{g,i} = \frac{\rho \omega_{g,i}}{M_i} = x_{g,i} \frac{p_g}{RT} \tag{2.2}$$

$$J_{g,i}^{\text{diff}} = -c_{g,i}\sum_{j=1}^{n} D_{i,j}\boldsymbol{d_j} \quad \text{with} \quad \boldsymbol{d_j} = \nabla x_j + \frac{(x_{g,j} - \omega_{g,j})\nabla p_g}{p_g} \tag{2.3}$$

As boundary condition at the fibre inlet was assumed that the concentrations of the gas species are known (from the syngas composition) and remain constant (Equation 2.4). In cases with evaporation from the liquid side to the gas phase, this inlet boundary was changed into a Danckwerts-type boundary (Equation 2.5). Symmetry was imposed to represent the middle of the fibre (Equation 2.6). At the end of the fibre, a no flux condition was imposed (Equation 2.7). The species flux across the membrane was modelled according to Equation 2.8. By imposing flux continuity, the radial gas phase flux equals the flux through the membrane. The convective flux was calculated with Equation 2.9. This convective flux is based on the Stefan velocity, which can be described as the velocity, normal to the membrane, associated with mass transfer (Raja et al., 2000).

$$c_{g,i}(z=0) = c_{g.i,in} \tag{2.4}$$

$$\boldsymbol{u_g} c_{g,i}(z=0) = \boldsymbol{u_g} c_{g.i,in} - J_{g,i}^{\text{diff}} \tag{2.5}$$

$$J_{g,i}^{\text{diff}}(r=0) = 0 \tag{2.6}$$

$$J_{g,i}^{\text{diff}}(z=L_f) = 0 \tag{2.7}$$

$$J_{i,gm}^{\text{int}} = J_{g,i}^{\text{diff}} + J_{g,i}^{\text{conv}} = -D_{m.i}\frac{\mathrm{d}c_{m,i}}{\mathrm{d}r} \tag{2.8}$$

$$J_{i,g}^{\text{conv}} = c_{g,i}u_s \quad \text{with} \quad \frac{p_g}{RT}u_s = \sum_{i=1}^{n}\left(J_{i,g}^{\text{diff}} + c_{g,i}u_s\right) \tag{2.9}$$

In a dense PDMS membrane, species transport can be modelled according to the solution-diffusion model and can therefore be described according to Fick's law (Equation 2.10) as it can be assumed that all compounds are dissolved in the membrane (Kumar et al., 2008). No convection was imposed in the membrane. Diffusion was assumed to be isotropic (omnidirectional). No flux ($J_i = 0$) was imposed at $z = 0$ and $z = L_f$. At the gas-membrane interface, the species concentration in the membrane was coupled with the gas phase concentrations, while taking partition between the gas and membrane into account (Equation 2.11). The flux through the membrane was coupled to the flux in the biofilm, assuming flux continuity (Equation 2.12). The membrane diffusion and partition coefficients of the dissolved species are calculated in Appendix D.2. The biofilm species diffusion coefficient was calculated from the liquid diffusion coefficient (Appendix D.3), while assuming a biofilm diffusivity factor f_B (Kumar et al., 2008).

$$\frac{\partial c_{m,i}}{\partial t} = -D_{m.i}\nabla^2 c_{m,i} \tag{2.10}$$

$$c_{m,i}^{\text{gm,int}} = K_i^{mg} \times c_{g,i}^{\text{gm,int}} \tag{2.11}$$

$$J_{i,mb}^{\text{int}} = -D_{b.i}\frac{\mathrm{d}c_{b,i}}{\mathrm{d}r} \quad \text{with} \quad D_{b,i} = f_B \times D_{l,i} \tag{2.12}$$

The biofilm thickness d_b and its biomass concentration $c_{b,x}$ were assumed to remain constant. Solutes transport can be described with Fick's law and reaction (Equation 2.13), as no convection was imposed in the biofilm. No flux ($J_i = 0$) was imposed at $z = 0$ and $z = L_f$. Flux continuity was imposed at the biofilm-liquid interface (Equation 2.14). Biofilm growth and detachment has been modelled (Equation 2.15) (Horn and Lackner, 2014), and was only taken into account cases with liquid recirculation. Details on biofilm growth and detachment can be found in Appendix G. At the membrane-biofilm interface, the solutes concentrations were coupled to the concentrations in the biofilm, while taking partition into account (Equation 2.16). However, for larger pressures, supersaturation and subsequent bubble formation could occur in the biofilm. It was assumed that in these cases the concentration of solutes in the biofilm equals the maximum solubility (calculated in Appendix D.3).

$$\frac{\mathrm{d}c_{b,i}}{\mathrm{d}t} = -D_{b,i}\nabla^2 c_{b,i} + q_i c_{b,x} \tag{2.13}$$

$$J_i^{\text{bl,int}} = -D_{l.i}\frac{\mathrm{d}c_{l,i}}{\mathrm{d}r} \tag{2.14}$$

$$J_x^{\text{bl,int}} = c_{b,x}u_g = c_{b,x}\int\limits_{r_{mb}^{\text{int}}}^{r_{bl}^{\text{int}}} \mu\,\mathrm{d}r \tag{2.15}$$

$$c_{b,i}^{\text{mb,int}} = \begin{cases} c_{m,i}^{\text{ml,int}} \Big/ K_i^{ml} & \text{when } c_{m,i}^{\text{ml,int}} \Big/ K_i^{ml} < c_{l,i}^{sol} \\ c_{l,i}^{sol} & \text{when } c_{m,i}^{\text{ml,int}} \Big/ K_i^{ml} > c_{i,l}^{sol} \end{cases} \tag{2.16}$$

Transport in the shell liquid phase was governed by axial convection and radial diffusion. Microbial conversion of CO was also taken into account when suspended biomass was present (Equation 2.17). At the liquid inlet, a Danckwerts boundary condition was imposed (Equation 2.18) as this takes axial dispersion into account (Danckwerts, 1953). At the liquid outflow, a no-flux condition was applied (Equation 2.19). No partition was imposed at the biofilm-liquid boundary (Equation 2.20). Lastly, symmetry was applied in the middle of the liquid phase (Equation 2.21).

Evaporation of water and ethanol from the liquid to the gas phase has been modelled as well. In these cases it has been assumed that the driving force for evaporation is the partial pressure gradient over the membrane, which was based on the saturation pressure in the gas phase and the concentration in the liquid phase. Evaporation modelling is described and discussed in Appendix E in more detail.

$$\frac{\mathrm{d}c_{l,i}}{\mathrm{d}t} = -\boldsymbol{u_l}\cdot\nabla c_{l,i} - D_{l,i}\nabla^2 c_{l,i} + q_i c_{l,x} \tag{2.17}$$

$$\boldsymbol{u_l} c_{l,i}(z=0) = \boldsymbol{u_l} c_{l,i,in} + D_{l,i}\frac{\mathrm{d}c_{l,i}}{\mathrm{d}z} \tag{2.18}$$

$$\frac{\mathrm{d}c_{l,i}}{\mathrm{d}z}(z=L_f) = \boldsymbol{u_l}\nabla c_{l,i} \tag{2.19}$$

$$c_{l,i}^{\text{bl,int}} = c_{b,i}^{\text{bl,int}} \tag{2.20}$$

$$\frac{\mathrm{d}c_{l,i}}{\mathrm{d}r}(r=r_l) = 0 \tag{2.21}$$

Microbial conversion of CO was modelled according to Equation 2.22. This equation is based on the CO uptake kinetics which were derived by (Mohammadi et al., 2014) and a linear fit of ethanol inhibition data from Fernández-Naveira et al. (2016). When the ethanol concentration is higher than $45\,\mathrm{g\,L^{-1}}$, $I_{EtOH} = 0$. By derivation of a black-box stoichiometric model for *Clostridium spp.* (Kleerebezem and Van Loosdrecht, 2010) for the metabolic and catabolic reactions, the reaction stoichiometry was determined. By correcting for the maintenance requirement v_{ms}, the microbial-specific growth rate was calculated (Equation 2.23). With the Herbert-Pirt relationship, the compound-specific reaction rates were calculated (Equation 2.24). Details on the derivation of the kinetic model for CO uptake, ethanol inhibition and the reaction stoichiometry can be found in Appendix F.

$$-q_{CO} = -q_{CO}^{max} I_{CO} I_{EtOH} = -q_{CO}^{max} \times \frac{c_{k,CO}}{K_{p,CO} + c_{k,CO} + \frac{c_{k,CO}}{K_{I,CO}}}\left(1 - \frac{c_{k,EtOH}}{K_{I,EtOH}}\right) \quad \text{with} \quad k = [b,l] \tag{2.22}$$

$$\mu = \frac{q_{CO} - v_{ms}}{Y_{CO}^{met}} \tag{2.23}$$

$$q_i = Y_i^{met}\mu + \frac{v_{ms}Y_{CO}^{cat}}{Y_i^{cat}} \tag{2.24}$$

2.3.2. Flow balances

Syngas flow through the fibre was assumed to be a compressible, laminar flow. Laminar flow was assumed after calculation of the Reynolds number ($Re \approx 6.7$, Appendix D.1). Gravity was not included due to the low gas density and the short length of the fibre. The viscosity η_g of the syngas with the composition at the inlet was calculated in Appendix D.1 and assumed not to change along the fibre length.

Mass continuity (Equation 2.25) and momentum continuity, which is modelled by the constitutive Navier-Stokes equations, (Equation 2.26) were coupled, while taking into account a varying density (Equation 2.2) (Haddadi et al., 2018). In these equations, $\boldsymbol{I}$ was used to describe the identity matrix. In the Navier-Stokes equation, $-\rho_g\left(\boldsymbol{u_g}\cdot\nabla\right)\boldsymbol{u_g}$ is a term to describe momentum changes caused by advection, $\nabla\cdot\left(-p_g\boldsymbol{I}\right)$ describes changes due to pressure differences, $\nabla\cdot\left(\eta_g\left(\nabla\boldsymbol{u_g}+\left(\nabla\boldsymbol{u_g}\right)^T\right)\right)$ describes viscosity effects, and the term $\nabla\cdot\left(\frac{2}{3}\eta_g\left(\nabla\cdot\boldsymbol{u_g}\right)\boldsymbol{I}\right)$ describes velocity divergence effects caused by the compressibility of the gas flow.

$$\frac{\partial\rho_g}{\partial t} = -\nabla\cdot\left(\rho_g\boldsymbol{u_g}\right) \tag{2.25}$$

$$\frac{\partial\rho_g\boldsymbol{u_g}}{\partial t} = -\rho_g\left(\boldsymbol{u_g}\cdot\nabla\right)\boldsymbol{u_g} + \nabla\cdot\left(-p_g\boldsymbol{I} + \eta_g\left(\nabla\boldsymbol{u_g} + \left(\nabla\boldsymbol{u_g}\right)^T\right) - \tfrac{2}{3}\eta_g\left(\nabla\cdot\boldsymbol{u_g}\right)\boldsymbol{I}\right) \tag{2.26}$$

Symmetry was imposed at $r = 0$ (Equation 2.27). At the gas-membrane interface a no-slip condition was imposed (Equation 2.28). The pressure was regulated at the fibre outlet with a pressure controller (Equation 2.29), which suppresses the backflow. The fibre gas flow at the inlet was assumed to be fully developed (as the length of the fibre is much larger than the diameter of the fibre (Wang et al., 2017a)) and equals the total gas flow into the lumen divided by the number of fibres (Equation 2.30).

$$u_{g,r}\Big|_{r=0} = 0 \quad \text{and} \quad \frac{\partial u_{g,z}}{\partial r}\Big|_{r=0} = 0 \tag{2.27}$$

$$\boldsymbol{u_g}(r = r_{gm}^{\text{int}}) = 0 \tag{2.28}$$

$$p_g(z = L_f) = p_{ref} + \Delta p_g \tag{2.29}$$

$$F_{g,f,in}(z=0) = \frac{F_{g,in}}{N_f} \tag{2.30}$$

The shell liquid flow was modelled by assuming laminar flow as the maximum Reynolds number was calculated to be around 15 (Appendix D.3). As the liquid density is around 1000 times higher than the gas density, gravity was included while modelling the liquid phase. The viscosity was calculated based on the viscosity of water (Appendix D.3). Effects of the solutes (nutrients, ethanol, dissolved gasses and biomass) on the viscosity and the density of the liquid phase were always neglected.

Mass continuity was modelled (Equation 2.31) as well as momentum continuity (Equation 2.32). For the constitutive Navier-Stokes equations, incompressible liquid flow was assumed. The term $\rho_l\left(\boldsymbol{u_l}\cdot\nabla\right)\boldsymbol{u_l}$ describes the advective effects on momentum. The second term, $\nabla\cdot\left(-p_l\boldsymbol{I}\right)$ describes pressure effects, the third term $\nabla\cdot\left(\eta_l\left(\nabla\boldsymbol{u_l}+\left(\nabla\boldsymbol{u_l}\right)^T\right)\right)$ viscosity effects, and the last term $\rho_l\boldsymbol{g}$ gravitational effects. Note that the gravitational constant is a vector as the gravitational constant only applies in the axial direction.

$$\rho_l\nabla\cdot\boldsymbol{u_l} = 0 \tag{2.31}$$

$$\frac{\partial\rho_l\boldsymbol{u_l}}{\partial t} = -\rho_l\left(\boldsymbol{u_l}\cdot\nabla\right)\boldsymbol{u_l} + \nabla\cdot\left(-p_l\boldsymbol{I} + \eta_l\left(\nabla\boldsymbol{u_l} + \left(\nabla\boldsymbol{u_l}\right)^T\right)\right) + \rho_l\boldsymbol{g} \tag{2.32}$$

As boundary conditions, a no-slip condition was applied at the liquid-biofilm interface (Equation 2.33). Flow symmetry was applied at r_l, as this way only the half of the liquid phase needs to be modelled, saving computational effort (Equation 2.34). At the liquid outlet, the pressure was controlled, backflow was suppressed and the pressure was compensated for the hydrostatic pressure (Equation 2.35). At the inlet, the liquid flow to the shell was divided by the amount of fibres (2.36).

$$\boldsymbol{u_l}(r = r_{bl}^{\text{int}}) = 0 \tag{2.33}$$

$$u_{l,r}\Big|_{r=r_l} = 0 \quad \text{and} \quad \frac{\partial u_{l,z}}{\partial r}\Big|_{r=r_l} = 0 \tag{2.34}$$

$$p_l(z = L_f) = p_{ref} + \Delta p_l + \rho_l \boldsymbol{g} L_f \tag{2.35}$$

$$F_{l,f,in}(z = 0) = \frac{F_{l,mod,in}}{N_f} \tag{2.36}$$

2.3.3. Reservoir equations

The equations describing the liquid recirculation reservoir are the total and solute-specific mass balances over both the liquid and the gas phases. In order to solve these mass balances, it has been assumed that the reservoir is ideally mixed, that reaction can be neglected (for justification see Appendix H), that the reservoir volume is constant (i.e. steady-state) and that the pressure and temperature in the reservoir are constant at 1 atm and 37 °C. Whereas the balances for the HFM module can be solved in both time-dependent and in stationary studies, the reservoir balances were solved only for stationary studies.

In the liquid phase the total mass balance (Equation 2.37) was set up. It was assumed that the density of the liquid does not change and that therefore the reservoir inflow rate equals the reservoir outflow rate. The solute-specific mass balance has terms for flows in and out of the reservoir, flows from and to the module and mass transfer to the gas phase. The last term was not incorporated for biomass. By assuming ideal mixing and steady-state behaviour, this balance was rewritten for the concentration in the reservoir (Equation 2.38).

$$F_{l,res,in}\rho_{H2O} = F_{l,res,out}\rho_{H2O} \tag{2.37}$$

$$c_{l,i,res} = \frac{F_{l,res,in}c_{l,i,res,in} + F_{l,mod,out}c_{l,i,mod,in} + \left(k_{L,i}^{ov}a\right)_{res} V_{res}\frac{p_{i,res}}{RT}K_i^{lg}}{F_{l,mod,in} + F_{l,res,out} + k_{L,i}^{ov}aV_{res}} \tag{2.38}$$

The total gas phase mass balance was set up: this balance consists of an inflow term, outflow term and a the transport term for mass transfer from the liquid phase to the gas phase (Equation 2.39). Following this, also the component-specific balance was written, consisting these terms (Equation 2.40. By assuming steady-state, ideal mixing and ideal gas behaviour, this balance was rewritten in terms of the partial pressures in the reservoir and its outlet (Equation 2.41).

$$F_{g,res,out}\rho_{res,out} = F_{g,res,in}\rho_{res,in} + M_{av}\sum_{i=1}^{n}\left(k_{L,i}^{ov}a\right)_{res}V_{res}\left(K_i^{lg}\frac{p_{i,res}}{RT} - c_{l,i,res}\right) \tag{2.39}$$

$$\text{with} \quad \rho_{res} = \sum_{i=1}^{n}\frac{p_i}{RT}M_i \quad \text{and} \quad M_{av} = \sum_{i=1}^{n}\frac{p_{i,res}}{\sum\limits_{i=1}^{n}p_{i,res}}M_i$$

$$F_{g,res,in}\frac{p_{i,res,in}}{RT} = F_{g,res,out}\frac{p_{i,res,out}}{RT} + \left(k_{L,i}^{ov}a\right)_{res}V_{res}\left(K_i^{lg}\frac{p_{i,res}}{RT} - c_{l,i,res}\right) \tag{2.40}$$

$$p_{i,res} = RT\frac{F_{g,res,in}\frac{p_{i,res}}{RT} + \left(k_{L,i}^{ov}a\right)_{res}V_{res}c_{l,i,res}}{F_{g,res,out} + F_{l,res,out} + \left(k_{L,i}^{ov}a\right)_{res}V_{res}K_i^{lg}} \tag{2.41}$$

From the development of these mass balances became clear that the reservoir liquid concentrations and partial pressure and the gas outflow rate are all dependent on each other (Equations 2.38, 2.41, 2.39). The equations for the concentrations and the pressures can be solved in terms of each other, with the MATLAB symbolic solver (see Appendix H), but the gas outflow rate could not be solved for this way. Therefore, it has been assumed that the gas outflow rate is equal to the gas inflow rate: $F_{g,res,out} = F_{g,res,in}$. To justify this assumption, the gas outflow rate was recalculated after the pressures and concentrations were calculated (see Appendix H). Water evaporation in the reservoir was considered to be negligible (Appendix H) due to usage of a 4 °C condenser at the gas outlet.

2.4. Model solution

All models described were developed in the same simulation software package, COMSOL Multiphysics® 5.4. This software package enables finite-element analysis, which can be used to solve (partial) differential equations numerically in complex geometries. For finite-element analysis, the geometry is divided in small elements, which is the so-called mesh. The mesh used in the models described in this report (Figure 2.3) is made using a mapping-strategy. This way, small rectangles are created in the different compartments or domains. Near the domain boundaries (the interfaces between the phases), the mesh is refined. With this refinement, the fluxes at the interfaces in both domains can be calculated more precise, so that the chance of numerical errors will be decreased. For the whole reactor geometry, 6750 grid points were created. At each grid point, COMSOL will solve the provided equations and interpolates the results between these grid points.

COMSOL Multiphysics works with several user interfaces which can be used to describe certain physical phenomena. In these interfaces, model parameters need to be provided together with the boundary conditions. The equations and boundary conditions used for solving these transport phenomena in the specified domains and interfaces, are always mentioned in the remaining chapters of this report.

The models were solved using the *fully coupled* nonlinear solver, with the automatic highly nonlinear (Newton) solver option and the MUMPS linear solver. The default *fully coupled* solver was slightly modified: The minimum damping factor was increased to 1×10^{-4}, the initial damping factor was increased to 1 and the amount of iterations was increased to 100. The relative tolerance for convergence was always maintained at 0.001. This solver was used as this could solve nonlinear, iterative problems faster than the other solvers like the *segregated* solver.

In cases where the non-linearity of the system increased, for example after incorporating the reservoir, the previous solution was used as initial values for new solutions. In that case, boundary conditions for each species in the liquid inlet were consecutively added and solved for. This way the system converged easier and faster. When performing parametric studies, the solution of a previous parameter was used as initial value for the subsequent parameter.

The model was solved at a 4-core computer with 8GB RAM. The amount of memory used for solving one study was around 2.4 GB. The solution time heavily depends on the complexity and the deviation from the initial values used, but per simulation it was between 20 seconds and 3 minutes.

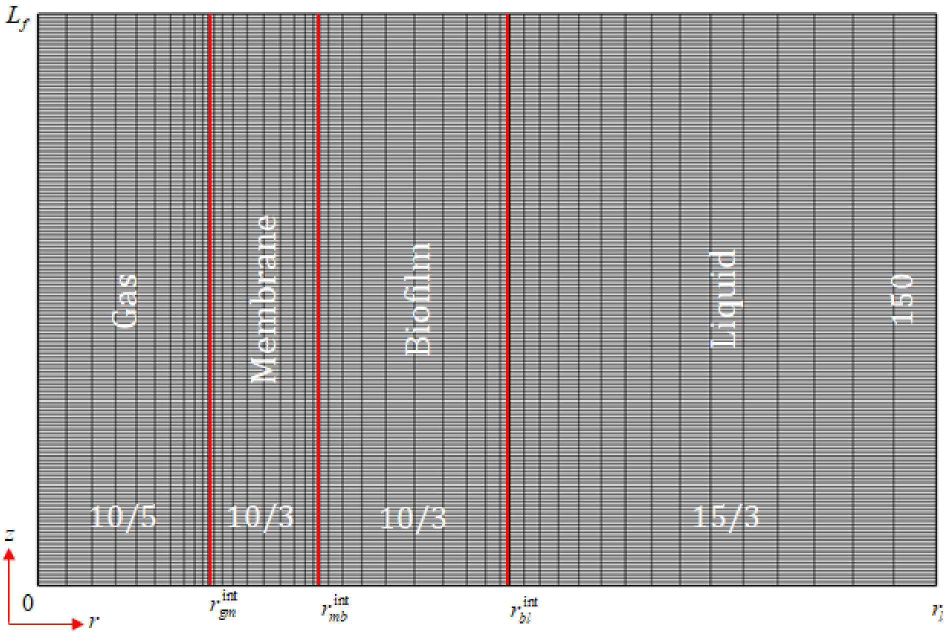

Figure 2.3: The mesh used for modelling the HFM reactor in COMSOL Multiphysics. For all domains, or compartments, the number of elements are provided. The amount of elements in the radial direction in each compartment is given at the bottom of each compartment, together with the refinement factor (after the slash). This refinement factor equals the factor by which the smallest element is smaller than the largest element: 10/5 means 10 elements in the radial direction with refinement factor 5. In all compartments, there are 150 elements in the axial direction.

2.5. Modelling steps

After making these assumptions, the modelling approach was defined. As the HFM reactor consists out of multiple different compartments, it became clear that the complexity of the whole model increases rapidly after the incorporation of more compartments. It was decided to start by modelling only the gas compartment flow and material balances and imposing a flux to the membrane. After this model was developed successfully, it could be extended with the neighbouring compartment - the membrane. Decisions could be made for developing the next model, based on the derived model results and the different examined operational conditions.

The same approach was used for modelling the biofilm and liquid compartments and the circulation reservoir, respectively. To check whether the model solves correctly, mass balances were introduced for each compartment. By calculating, per compound, the inflow, outflow, flux and reaction terms, these mass balances were checked. When the residuals of the mass balance were below a certain percentage (2% of the inflow) it was decided that the model was solved successfully.

After the gas phase model was developed and studied (Chapter 3), the membrane (Chapter 4) was incorporated. Then, the open-end fibre gas phase model was extended with a biofilm and liquid phase (Chapter 5). This model was subsequently extended with a reservoir to enable liquid recirculation (Chapter 6). After that, the effects of the process parameters could be determined (Chapter 7).

Table 2.1: Non-compound-specific parameters used for modelling the HFM membrane module. Some parameters were provided by the membrane producing company (OxyMem), others were calculated in an appendix or derived from literature. The process parameters were listed as well.

Parameter	**Symbol**	**Value**	**Unit**	**Reference**
General parameters				
Gravitational constant	$\boldsymbol{g}$	-9.81	m.s^{-2}	-
Universal gas constant	R	8.314	J.mol^{-1}.K^{-1}	-
Temperature	T	37	°C	-
Reference pressure	p_{ref}	1	atm	-
HFM module parameters				
Inner diameter	d_i	340	μm	Provided by OxyMem.
Membrane thickness	d_m	110	μm	Provided by OxyMem.
Fibre and module length	L_f	40	cm	Provided by OxyMem.
Number of fibres	N_f	550	-	Provided by OxyMem.
Shell volume	V_{shell}	500	mL	Provided by OxyMem.
Fibre spacing	d_{spacing}	0.123	cm	Calc. in Appendix C.
Volume-specific surface area	a	774	m^{-1}	Calc. in Appendix C.
Gas phase parameters				
Lumen gas flow rate^a	$F_{g,in}$	4 - 400	mL.min^{-1}	*Process parameter*
Fibre gas flow rate	$F_{g,f,in}$	0.0073 - 0.727	mL.min^{-1}	*Process parameter*
Lumen gas overpressure^b	Δp_g	0.5	bar	*Process parameter*
Syngas viscosity at inlet	η_g	1.1×10^{-5}	Pa.s	Calc. in Appendix D.1.
Syngas density at inlet	ρ_g	1.68	kg.m^{-3}	Calc. in Appendix D.1.
CO gas viscosity at inlet	η_g	1.8×10^{-5}	Pa.s	Calc. in Appendix D.1.
CO gas density at inlet	ρ_g	1.63	kg.m^{-3}	Calc. in Appendix D.1.
Biofilm and reaction parameters				
Diffusivity factor^c	f_B	0.8	-	Assumed
Biofilm thickness^c	d_b	100 or 190	μm	Assumed
Biomass concentration^c	$c_{b,x}$	15	kg.m^{-3}	Assumed
Maintenance requirement	$-v_{ms}$	0.066	mol$_{\text{CO}}$.mol$_x^{-1}$.h^{-1}	Calc. in Appendix F.
Max. CO uptake rate	$-q_{CO}^{max}$	0.0344	mol$_{\text{CO}}$.g$_x^{-1}$.h^{-1}	Mohammadi et al. (2014).
CO saturation constant	$K_{p,CO}$	0.0178	mol$_{\text{CO}}$.m^{-3}	Mohammadi et al. (2014).
CO inhibition constant	$K_{I,CO}$	0.510	mol$_{\text{CO}}$.m^{-3}	Mohammadi et al. (2014).
Ethanol inhibition constant	$K_{I,\text{EtOH}}$	978	mol$_{\text{EtOH}}$.m^{-3}	Calc. in Appendix F.
Liquid phase parameters				
Shell liquid flow rate^a	$F_{l,mod,in}$	10 - 500	mL.min^{-1}	*Process parameter*
Shell liquid flow rate per fibre	$F_{l,f,mod,in}$	0.00036 - 0.909	mL.min^{-1}	*Process parameter*
Liquid overpressure^b	Δp_l	0	atm	*Process parameter*
Liquid viscosity	η_l	7.08×10^{-4}	Pa.s	Calc. in Appendix D.3.
Liquid density	ρ_l	993.6	kg.m^{-3}	Janssen and Warmoeskerken (2006)
Reservoir parameters				
Gas inflow rate^a	$F_{g,res,in}$	1 - 100	mL.min^{-1}	*Process parameter*
Inlet pressure	$p_{res,in}$	1	atm	-
Liquid inflow rate^a	$F_{l,res,in}$	0.025 - 2	mL.min^{-1}	*Process parameter*
Reservoir volume^a	V_{res}	0.5	L	*Process parameter*
Volumetric mass transfer coeff.	$\left(k_{L,i}^{ov}a\right)_{res}$	30	h^{-1}	Assumed for all compounds

a) Different values for these parameters were used in the different models. The used values will be mentioned while discussing these models.

b) The used gas and liquid overpressures are 0.5 bar and 0 atm, unless mentioned otherwise. The used gas overpressure is, according to OxyMem, the maximum operating pressure.

c) The biofilm thickness, its biomass concentration, and the biofilm diffusivity factor are unknown and were assumed. Different values for the biofilm thickness were used and will be mentioned while discussing the different models with biofilms.

Table 2.2: Compound-specific parameters used for modelling the HFM membrane module. Partition and membrane diffusion values for ethanol and water are calculated in Appendix E for 37 °C, while the values of the gasses were calculated in Appendix D.2 for a temperature of 35 °C. All the other parameters were calculated for a temperature of 37 °C.

Parameter	**Symbol**	**Unit**	CO	CO_2	H_2	N_2	EtOH	H_2O	Biomass[a]	**Reference**
General parameters										
Molecular mass	M_i	$g.mol^{-1}$	28	44	28	2	46	18	24.6	-
Gas phase parameters										
Syngas mixture composition	$x_{g,i,in}$	$mol_i.mol_{gas}^{-1}$	0.15	0.21	0.10	0.54	-	-	-	Calc. in Appendix D.1.
CO gas inlet composition	$x_{g,i,in}$	$mol_i.mol_{gas}^{-1}$	1	10^{-8}	10^{-8}	10^{-8}	-	-	-	-
Maxwell-Stefan diffusion coeff.	$D_{g,i,av}$	$m.s^{-2}$	1.5×10^{-5}	1.2×10^{-5}	6.0×10^{-5}	1.6×10^{-5}	$\sim 10^{-5}$	$\sim 10^{-5}$	-	Calc. in Appendix D.1.
Membrane parameters and partition coefficients										
Membrane permeability	P_i	$m^2.s^{-1}$	3.82×10^{-10}	2.93×10^{-9}	7.23×10^{-10}	3.16×10^{-10}	3.41×10^{-8}	5.41×10^{-6}	-	Calc. in Appendix D.2 and E.
Diffusion coefficient	$D_{m,i}$	$m^2.s^{-1}$	3.40×10^{-9}	2.20×10^{-9}	1.40×10^{-8}	3.40×10^{-9}	1.46×10^{-9}	4.87×10^{-9}	-	Calc. in Appendix D.2 and E.
Membrane-gas partition coeff.	K_i^{mg}	-	0.1122	1.3333	0.0517	0.0930	23.36	1111	-	Calc. in Appendix D.2 and E.
Membrane-liquid partition coeff.	K_i^{ml}	-	5.201	2.048	2.731	6.752	0.0024	1.59×10^{-4}	-	Calc. in Appendix D.2 and E.
Liquid-gas partition coeff.	K_i^{lg}	-	2.16×10^{-2}	0.651	1.89×10^{-2}	1.38×10^{-2}	9721	22647	-	Calc. in Appendix D.2 and E.
Biofilm and reaction parameters										
Diffusion coefficient	$D_{b,i}$	$m^2.s^{-1}$	2.17×10^{-9}	2.05×10^{-9}	4.81×10^{-9}	2.01×10^{-9}	0.97×10^{-9}	-	-	Calc. in Appendix D.3.
Catabolic reaction yield	Y_i^{cat}	$mol_i.mol_{EtOH}^{-1}$	−6	4	0	0	1	−3	0	Calc. in Appendix F.
Metabolic reaction yield	Y_i^{met}	$mol_i.mol_x^{-1}$	−46.06	30.41	0	0	7.33	−22.58	1	Calc. in Appendix F.
Liquid parameters										
Diffusion coefficient	$D_{l,i}$	$m^2.s^{-1}$	2.71×10^{-9}	2.56×10^{-9}	6.01×10^{-9}	2.51×10^{-9}	1.21×10^{-9}	-	1.98×10^{-13}	Calc. in Appendix D.3.
Solubility	$c_{l,i}^{sol}$	$mol.m^{-3}$	0.85	25.6	0.74	0.54	-	-	-	Calc. in Appendix D.3.
Reservoir parameters										
Inlet partial pressure	$p_{i,res,in}$	atm	0	0	0	1	0	0	0	-
Liquid inlet concentration	$c_{l,i,res,in}$	$mol.m^{-3}$	0	0	0	0	0	55555.5	0	-

a) Considering a biomass composition of $CH_{1.8}O_{0.5}N_{0.2}$.

3

Gas phase

The model of the HFM module is developed in different stages, so that model complexity step-wise increases. Following this method, the gas phase was modelled and studied prior to implementing other phases and reactor configurations. In this chapter, a steady-state model of an open-end fibre containing only the gas compartment, was developed, solved and discussed. The gas phase model (M_gasphase) was developed to describe mass transfer inside the gas phase, to describe the flux to the membrane and its effects on the composition, velocity and density along the radial and axial direction of the gas phase. This will lead to concentration profiles of the different syngas constituents in the gas phase, which can be used to predict the distribution of the different syngas constituents in the lumen and in other compartments of the the HFM module.

3.1. Theory

The gas phase is expected to be dominated by both convection and radial diffusion, as was demonstrated by the calculation of the characteristic times in the Appendix B. When transport to other phases is neglected, the velocity profile is expected to be laminar due to the very small inner fibre diameter and the low gas density. This laminar velocity profile is expected to create a hydrodynamic boundary layer through which diffusion to the membrane takes place. However, as gas phase diffusion is several orders of magnitude larger than diffusion through the membrane (10^{-5} compared to $10^{-8}\,\mathrm{m^2\,s^{-1}}$), gas diffusion is not expected to be a limiting factor for mass transfer (Orgill et al., 2019).

The low characteristic times of radial diffusion phenomena do not mean that diffusion-related phenomena can entirely be neglected, as mass transfer to the membrane will depend on radial diffusion. Common theories to describe diffusion are the film theory combined with Fick's law (Lewis and Whitman, 1924) and Maxwell-Stefan diffusion (Krishna and Wesselingh, 1997). As there is not a specific solvent in the gas phase, since the mole fractions of syngas constituents are in the same order of magnitude, Fick diffusion is not valid and Maxwell-Stefan diffusion is regarded to be a better approximation for gas diffusion (Krishna and Wesselingh, 1997).

There has been research on the calculation of the gas phase mass transfer coefficient. The mass transfer coefficient is often described by the Sherwood number (Equation 3.1) in order to compare results for different reactor configurations. The gas flow velocity and fibre diameter heavily influence the mass transfer boundary layer and are thus essential parameters for the prediction of the mass-transfer coefficient. This can be taken into account with the Graetz number (Equation 3.2), which describes the ratio between convection and radial diffusion. Leveque derived solutions for cases with low and high Graetz numbers (Equation 3.3), by assuming a fully developed laminar fluid flow and constant interface concentrations (Kumar et al., 2003; Hashemifard et al., 2015).

$$Sh_{g,i} = \frac{k_{g,i} d_i}{D_{g,i,av}} \tag{3.1}$$

$$Gz_{g,i} = \frac{d_i}{L_f} Re_g Sc_g = \frac{d_i}{L_f} \frac{\rho_g v_g d_i}{\eta_g} \frac{\eta_g}{\rho_g D_{g,i,av}} = \frac{d_i^2 v_g}{L_f D_{g,i,av}} \tag{3.2}$$

$$Sh_{g,i} = \begin{cases} 3.67 & \text{when } Gz_{g,i} < 10 \\ 1.62 Gz_{g,i}^{1/3} & \text{when } Gz_{g,i} > 20 \end{cases} \tag{3.3}$$

Orgill et al. (2019) proposed a model to calculate the k_L^{ov} for the different syngas constituents in a HFM reactor. In their model, they assumed constant bulk concentrations of gaseous compounds, which could be an unrealistic assumption when mass transfer takes place. Other authors who modelled HFM reactors either assumed that gas phase concentrations were constant (Ahmadi Motlagh et al., 2006), or uniform gas flow velocity (Atchariyawut et al., 2008). Ghidossi et al. (2006) and Haddadi et al. (2018) recognized that the gas flow rate changes due to transmembrane flux and proposed an iterative algorithm in HFM modules to take both hydrodynamics and flux into account. Shirazian et al. (2009) developed a 2D model for CO_2 absorption in gas-liquid membrane contactors, but did not couple the gas flow with mass transfer. Thus far, no 2D model has been developed which describes syngas mass transfer in a HFM reactor while taking hydrodynamics, transmembrane flux and Maxwell-Stefan diffusion into account.

It can be expected that due to mass transfer to the membrane, the total amount of mass in the gas phase will decrease along the fibre length. This will influence the density and velocity of the gas phase. Maxwell-Stefan diffusion will result in gradients next to the membrane, causing that some compounds will diffuse against their gradient while others diffuse according to their gradient. For dense PDMS membranes, the compound-specific flux depends on the permeability of the compound inside the membrane (Kumar et al., 2008; Orgill et al., 2019). Therefore, the flux is expected to be the largest for compounds with high membrane permeability (like CO_2) while it should be lower for CO (Table 2.2). As liquid phase mass transfer is not incorporated in this model, mass transfer is expected to be limited by the membrane as mass transfer in the gas phase is much faster than in the membrane phase.

3.2. Model development

In Appendix D.1, the gas phase Reynolds, Peclet and Graetz numbers were calculated. From this analysis became clear that the gas flow is laminar ($Re \approx 6.7$), that axial convection dominates axial diffusion ($Pe \approx 5200$), and radial diffusion dominates axial convection ($Gz \approx 3.7 \times 10^{-3}$). While taking this into account, the model was developed in COMSOL Multiphysics. The model has the following additional characteristics as compared to the model described in Chapter 2.

- The syngas flow rate $F_{g,in}$ was set to be $400\,\mathrm{mL\,min^{-1}}$.
- The syngas mixture was used while modelling the gas flow.
- Concentrations of all compounds at the membrane outer side (r_{mb}^{int}) are $0\,\mathrm{mol\,m^{-3}}$.

The COMSOL *transport of concentrated species* interface is used to simulate transport of gaseous compounds. N_2 was used as reference compound, as it has the highest the mole fraction in the syngas used. This interface solves at all mesh nodes the solute-specific mass balances as described by Equation 2.1, based on the mass fractions of all compounds. The boundary conditions are described by Equations 2.4 (using a constant syngas composition), 2.6 and 2.7. The flux to the membrane was calculated using Equation 3.4. By imposing partition between gas phase and membrane phase, the flux becomes a function of the gas phase concentration.

The gas flow was simulated using the COMSOL *laminar flow* interface, which solves the Navier-Stokes and continuity equations at each mesh node (Equations 2.25 and 2.26), given boundary equations 2.27, 2.28, 2.29 and 2.30.

Coupling between the two interfaces was established with the *reacting flow* interface. This way, the velocity of the gas phase is able to change due to changes in the composition of the gas phase. This takes the convective flux and the Stefan velocity into account with Equations 2.8 and 2.9. Without this interface, the mass balances in the gas phase did not solve correctly.

The model results were checked by formulating mass balances for all species in the gas phase according to Equation 3.5. All gas species entering the lumen should leave the gas compartment either via the gas outlet or via the membrane. When the model is solved correctly, $\frac{dN_{g,i}}{dt}$ approximates 0.

$$J_{i,gm}^{\text{int}} = -D_{m,i}\frac{\mathrm{d}c_{m,i}^{\text{mb,int}}}{\mathrm{d}r} = -D_{i,m}\frac{c_{m,i}^{\text{mb,int}} - c_{m,i}^{\text{gm,int}}}{r_{mb}^{\text{int}} - r_{gm}^{\text{int}}} = -D_{i,m}\frac{0\,\text{mol}\,\text{m}^{-3} - K_i^{mg} c_{g,i}^{\text{gm,int}}}{d_m} \tag{3.4}$$

$$\frac{\mathrm{d}N_{g,i}}{\mathrm{d}t} = \int_0^{A_{c,g}} \boldsymbol{u_g} c_{g,i}\,\mathrm{d}A_{c,g}\bigg|_{z=0} - \int_0^{A_{c,g}} \boldsymbol{u_g} c_{g,i}\,\mathrm{d}A_{c,g}\bigg|_{z=L_f} - \int_0^{A_{s,gm}^{\text{int}}} J_{i,gm}^{\text{int}}\,\mathrm{d}A_{s,gm}^{\text{int}}\bigg|_{r=r_{gm}^{\text{int}}} = 0 \tag{3.5}$$

3.3. Results and discussion

The compound-specific mass balances (Equation 3.5) were solved correctly, according to the results of the model (Table A.2). The gas-membrane flux was plotted for all compounds along the gas-membrane interface in the axial direction (Figure 3.1a). From this, it was observed that the flux of CO_2 is the highest of all fluxes, and decreases with almost 50% along the axial direction. The N_2 flux increased while the CO and H_2 fluxes did not change substantially along the fibre length.

The mass transfer rate and yield (Equations 3.6 and 3.7) of all compounds were calculated and plotted against their permeability (Figure 3.1b). From this was found that 65% of the CO_2 entering the lumen was transferred into the membrane, while the transfer yield of the other compounds is much lower (13, 23 and 11% for CO, H_2 and N_2, respectively). These differences in transfer yield were explained by the differences in permeability of these compounds in the membrane. The compounds with the highest permeability in the membrane (CO_2 and H_2) also have the largest transfer yield. For the mass transfer rate and fluxes this pattern did not hold, since these are partially dependent on the concentrations in the gas phase. As N_2 has a high mole fraction in the gas inlet, the concentration along the axial direction is higher than that of the others, causing a higher mass transfer rate.

$$T_i^{\text{gm,int}} = \int_0^{A_{s,gm}^{\text{int}}} J_{i,gm}^{\text{int}}\,\mathrm{d}A_{s,gm}^{\text{int}}\,\frac{N_f}{V_{\text{shell}}} \tag{3.6}$$

$$Y_{g,i}^{MT} = 1 - \frac{\int_0^{A_{c,g}} \boldsymbol{u_g} c_{g,i}\,\mathrm{d}A_{c,g}\Big|_{z=L_f}}{\int_0^{A_{c,g}} \boldsymbol{u_g} c_{g,i}\,\mathrm{d}A_{c,g}\Big|_{z=0}} = \frac{\int_0^{A_{s,gm}^{\text{int}}} J_{i,gm}^{\text{int}}\,\mathrm{d}A_{s,gm}^{\text{int}}\Big|_{r=r_{gm}^{\text{int}}}}{\int_0^{A_{c,g}} \boldsymbol{u_g} c_{g,i}\,\mathrm{d}A_{c,g}\Big|_{z=0}} \tag{3.7}$$

$$\tilde{c}_{g,i} = \frac{c_{g,i}}{\max\left(c_{g,i}\right)} \tag{3.8}$$

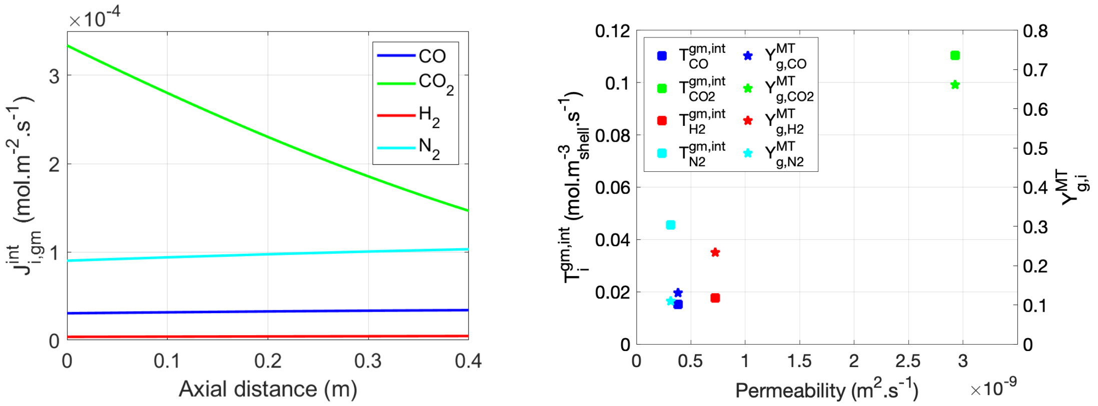

(a) (b)

Figure 3.1: (a) Fluxes of the gas species at the gas-membrane interface (in $\mathrm{mol\,m^{-2}\,s^{-1}}$) along the axial direction. (b) The gas phase mass transfer rate (left axis, squares) and yield (right axis, pentagons) of the gaseous species, were plotted against their permeability

The concentrations of the gas species were plotted along the radial and axial direction of the lumen (Figure 3.2). The concentrations were normalized according to Equation 3.8. It was observed that only the concentration of CO_2 decreases, by around 55%. As substitutes, the concentrations of H_2, N_2 and CO increase by around 1, 15 and 10%, respectively. As the flux through the membrane depends on the concentration in the gas phase, the CO_2 flux decreased due to its decreasing concentration, while the flux of N_2 increased due to its increasing concentration. The increasing concentrations along the axial direction can be explained by the fact the sum of the mole fractions of all gaseous compounds must remain unity (see Figure 3.3a). Due to the fixed pressure at the outlet (Figure 3.3b), the concentrations of some compounds have to increase to maintain that pressure, despite the transfer of the other compounds. This causes substantial changes in the mole composition and density of the syngas along the axial direction (Figure 3.3a and c). The pressure drop in the fibre corresponded to the pressure drop as calculated by the Darcy-Weisbach pressure drop equation (Appendix D.1).

Next to this, the velocity profile of the lumen gas flow was plotted (Figure 3.4a). The velocity distribution does not follow the typical laminar pattern: At the outlet the average velocity became lower than the average inlet velocity (0.10 and 0.13 $\mathrm{m\,s^{-1}}$, respectively) and there is a velocity component towards the radial direction. Due to mass transfer, the density of the gas phase has decreased, which leads in turn to lower velocities. This was expected as mass transfer was coupled to the fluid velocity.

No gradient in the radial concentrations of the gasses was observed (Figure 3.2). This could be expected as gas phase diffusion is very fast compared to diffusion in other media. However, this does not mean that there are no concentration differences in the radial direction. Following Maxwell-Stefan diffusion, it could be expected that there are some compounds diffusing with their gradient and diffusing against their gradient. In order to examine this, the diffusive and convective mass transfer rates were examined by normalizing the total mass transfer rate (Equation 3.9, Figure 3.4b).

From this was derived that only for CO_2 the diffusive flux is positive, meaning that this compound diffuses according to its gradient. The diffusive fluxes of the other compounds are negative, so that they diffuse against their gradient towards the membrane. Then, for mass transfer towards the membrane, the convective flux (driven by the Stefan velocity) must be larger than the diffusive flux, so that the net flux is positive, which was the case for all compounds. This means that CO_2 drags the other compounds against their concentration gradient towards the membrane. It was also observed that the average Maxwell-Stefan diffusion coefficient of CO_2 was lower than the coefficient of the other species (Table D.2). This diffusion coefficient is inversely

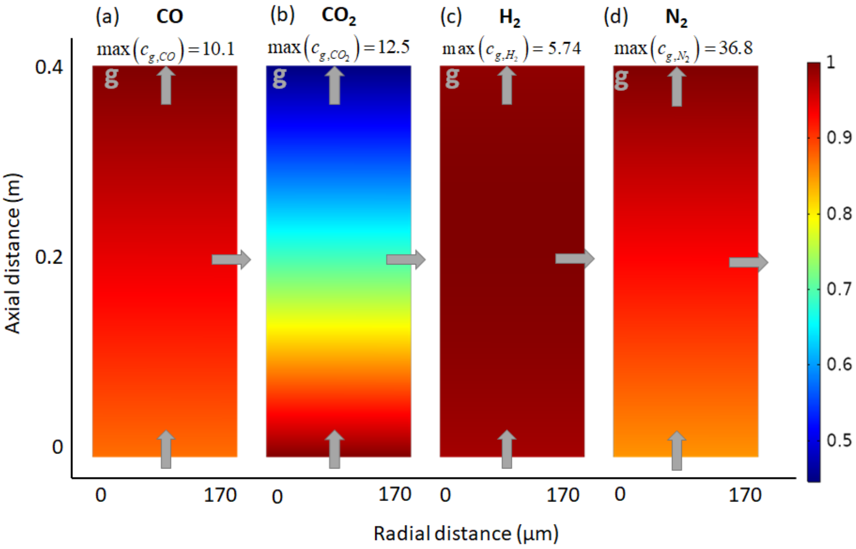

Figure 3.2: The normalized concentration gradients of (a) CO, (b) CO_2, (c) H_2 and (d) N_2 are plotted along the radial and axial direction of the gas compartment. The concentrations have been normalized according to Equation 3.8. The maximum concentration of each compound in the gas phase in mol m^{-3} is provided in the figure. The gas domain is depicted with *g*. The gas inlet, outlet and the direction of transport to the membrane are depicted with the corresponding arrows.

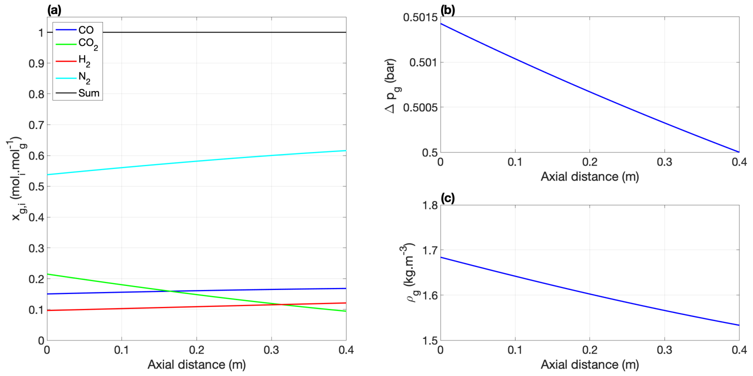

Figure 3.3: Along the axial direction, (a) the mole fractions of all gasses and their sum are plotted, as well as (b) the gas phase overpressure and (c) density.

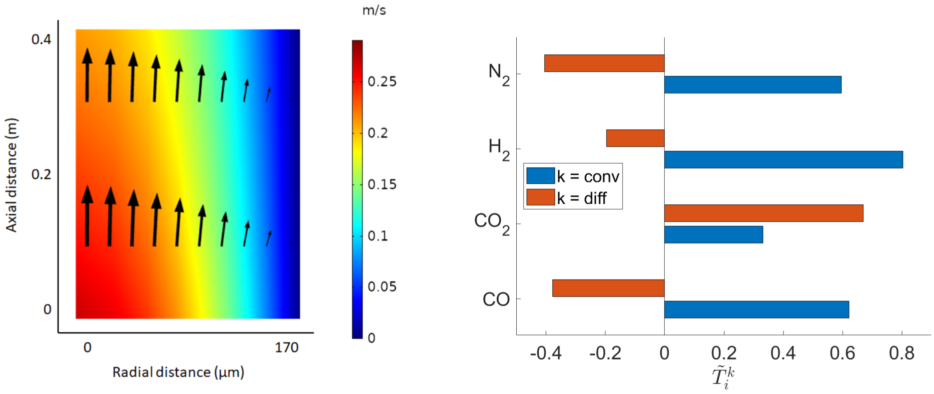

(a)

(b)

Figure 3.4: (a) The velocity profile of the gas flow in the lumen. The arrow size is proportional to the total velocity magnitude in the axial and radial direction $\boldsymbol{u_g}$. The average velocity at the used gas flow rate $F_{g,in}$ of 400 mL min^{-1} equals 0.13 m s^{-1}. (b) For all gas species, their diffusive and convective mass transfer rates were determined as percentage of the total mass transfer rates.

proportional to the friction coefficient, indicating CO_2 has a higher friction coefficient. This higher friction coefficient in turn increases the driving force for mass transfer and therefore the diffusive flux (Krishna and Wesselingh, 1997).

$$\tilde{T}_i^{\mathrm{k}} = \frac{\int_0^{A_{s,gm}^{\mathrm{int}}} J_{i,gm}^{\mathrm{conv}} \,\mathrm{d}A_{s,gm}^{\mathrm{int}}}{\int_0^{A_{s,gm}^{\mathrm{int}}} J_{i,gm}^{\mathrm{conv}} \,\mathrm{d}A_{s,gm}^{\mathrm{int}} + \left| \int_0^{A_{s,gm}^{\mathrm{int}}} J_{i,gm}^{\mathrm{diff}} \,\mathrm{d}A_{s,gm}^{\mathrm{int}} \right|} \qquad \text{with } k = [\mathrm{conv}, \mathrm{diff}] \tag{3.9}$$

Lastly, the mass transfer coefficient in the gas phase for CO $k_{g,CO}$ was calculated using Equation 3.3 (with $Sh = 3.67$) to be $0.13\,\mathrm{m\,s^{-1}}$. This high value of $k_{g,CO}$, indicates that in the performed simulations the inner gas mass transfer resistance is very low and can therefore be neglected for mass transfer to and from other phases.

3.4. Conclusion

From the gas phase model can be concluded that along the radial direction there are no large changes in concentrations of the gaseous compounds, implying that radial gas diffusion is always larger than membrane diffusion. However, from modelling Maxwell-Stefan diffusion, was observed that only CO_2 diffuses according to its gradient and it drags the other compounds against their gradient towards the membrane.

Furthermore, it was found that for all compounds, the fluxes, concentrations and mole fractions change along the axial direction. Next to this, the gas phase velocity did not follow a typical laminar pattern. This indicates that a multi-component gas phase in HFM modules cannot be described with simplified assumptions of constant concentration or gas velocities, as was done in literature before.

Last but not least, the location dependency of the compound fluxes and the different mass transfer yields are important to take into account in HFM reactors. Due to flexibility of the metabolism of *Clostridium* spp., different metabolic routes and rates can be obtained along the fibre length. Possible differences in growth rates along the axial direction could lead to operational problems like clogging or increased pressure drops. Therefore, when simplifications are done for the gas phase, it could happen that the performance of the reactor system is not the same as was expected on forehand. These results should be taken into account when designing HFM modules for industrial scale applications.

4

Membrane phase

As next step, the gas model was extended with the membrane compartment. The membrane compartment has been modelled as separate step. A dense, hydrophobic PDMS membrane will be modelled and solved in a stationary study. This model (M_membrane) enables determining the impact of the membrane on mass transfer from the gas phase to the biofilm and liquid phases. With this model, the impact of the membrane on the total flux and the concentration gradient inside the membrane can be investigated.

When this model has been developed, design choices can be made for optimizing the HFM module: The influence of the gas flow rate on the mass transfer yield and rate was determined (M_memb_Fgin), as well as the usefulness of working with a closed gas phase configuration (M_closed).

4.1. Theory

In Chapter 1.4, the different types of membranes that could be used in HFM modules were shortly discussed. It was chosen to work with a dense hydrophobic membrane due to their resistance to higher pressures, ability to prevent wetting and biofouling, and commercial availability (Kumar et al., 2008; Orgill et al., 2013; Yasin et al., 2015).

For modelling mass transfer across the membrane, Thomas Graham's solution-diffusion model could be assumed (Graham, 1863; Shao et al., 2009). This model interprets membrane diffusion according to three consecutive steps. The first step comprises sorption of the gasses in the feed-side of the membrane. After sorption, the gasses diffuse through the membrane towards the permeate side. At the permeate side, they are desorbed. The driving force for mass transfer is the difference in chemical potential between the feed and permeate sides. By assuming ideality at both sides, the driving force can be related to partial pressures or concentrations (Shao et al., 2009; Haddadi et al., 2018).

The permeability can be described by the diffusivity and the solubility coefficient. As the driving force for mass transfer is the concentration difference across the membrane, the mass flux is analogous to Fick's law (Equation 4.1) (Kumar et al., 2008; Shao et al., 2009; Haddadi et al., 2018). The adimensional solubility coefficient is defined as the ratio of concentrations between the membrane and the gas phase and thus equals the adimensional gas-membrane partition coefficient K_i^{mg} (Kumar et al., 2008; Shao et al., 2009). This enables rewriting Equation 4.1 with membrane-based concentrations (Equation 4.2). Lastly, the mass transfer coefficient in dense membranes can be expressed in terms of the permeability (Equation 4.3) (Reij et al., 1998; Kumar et al., 2008).

$$J_{m,i} = -P_i \frac{c_{b,i}^{\text{mb,int}} - c_{g,i}^{\text{gm,int}}}{r_{mb}^{\text{int}} - r_{gm}^{\text{int}}} \propto -D_{m,i} \times \frac{\mathrm{d}c}{\mathrm{d}r} \tag{4.1}$$

$$J_{m,i} = -P_i \frac{c_{b,i}^{\text{mb,int}} - c_{g,i}^{\text{gm,int}}}{r_{mb}^{\text{int}} - r_{gm}^{\text{int}}} = -D_{m,i} \times K_i^{mg} \frac{\frac{c_{b,i}^{\text{mb,int}}}{K_i^{lg}} - c_{g,i}^{\text{gm,int}}}{d_m} = -D_{m,i} \frac{c_{m,i}^{\text{mb,int}} - c_{m,i}^{\text{gm,int}}}{d_m} \tag{4.2}$$

$$k_{m,i}^{\text{dense}} = \frac{P_i}{d_m} = \frac{D_{m,i} \times K_i^{mg}}{d_m} \tag{4.3}$$

Next to this, the cylindrical geometry of the hollow fibre membrane needs to be taken into account. The surface area of the membrane at the shell side is larger than the one at the lumen side, leading to differences in flux in the radial direction. In a steady-state situation, the total mass transfer rate remains the same (Equation 4.4). This means that the flux at the membrane-biofilm interface can be expected to be a function of the flux at the gas-membrane interface (Equation 4.5).

$$T_i^{\text{gm,int}} = T_i^{\text{mb,int}} = A_{s,gm}^{\text{int}} J_{i,gm}^{\text{int}} = A_{s,mb}^{\text{int}} J_{i,mb}^{\text{int}} \tag{4.4}$$

$$J_{i,mb}^{\text{int}} = \frac{A_{s,gm}^{\text{int}}}{A_{s,mb}^{\text{int}}} J_{i,gm}^{\text{int}} = \frac{\pi L_f N_f (d_i)}{\pi L_f N_f (d_i + 2d_m)} J_{i,gm}^{\text{int}} = \frac{d_i}{d_i + 2d_m} J_{i,gm}^{\text{int}} = 0.607 J_{i,gm}^{\text{int}} \tag{4.5}$$

From this can be expected that there will be large differences in flux for all compounds, as the flux is compound-specific. These large differences in flux will also lead to large differences in concentrations of each compound at the two sides of the membrane.

In a closed-end gas phase configuration, the lumen is sealed off at the end. This causes that all gasses entering the lumen must transfer to the membrane, when a steady-state is reached. This way, Perez-Calleja et al. (2017) was able to achieve 100% mass transfer yields.Munasinghe and Khanal (2012) used closed-end operation for CO transfer. Using closed-end configurations, it can be expected that there will be less convection than diffusion, which could negatively impact the flux and the overall mass transfer rate.

4.2. Model development

For extending the gas model with the membrane in COMSOL Multiphysics, the following additional characteristics are used, compared to the model described in Chapter 2.

- The syngas flow rate $F_{g,in}$ was set to be 400 mL min^{-1}.
- The syngas mixture was used while modelling the gas flow.
- Concentrations 200 µm away from the membrane are 0 mol m^{-3}.

Using the *transport of diluted species* interface in COMSOL, the membrane phase can be modelled. This interface solves Equation 2.10. Flux continuity was imposed in the gas domain, at the gas-membrane interface using Equation 2.8. Boundary condition 2.11 was used to impose partition at the gas-membrane interface. As constraint, it was set that this boundary condition applies to *individual dependent variables.* Otherwise the total mass balance was coupled with the gas phase, while with this constraint the component-specific mass balances were coupled. No flux was imposed at $z = 0$ and $z = L_f$. Flux to the biofilm was imposed using Equation 4.6. This type of flux imposes complete consumption of CO, CO_2 and H_2 in the biofilm. For comparison purposes, the same flux was modelled for N_2, although N_2 is inert. The mass balances were checked in the gas and membrane compartments, using Equations 3.5 and 4.7.

$$J^{\text{int}}_{i,mb} = -D_{b,i}\frac{\Delta c_{b,i}}{\Delta r} = -D_{b,i}\frac{c_{b,i} - K_i^{mb} \,/\, c^{\text{mb,int}}_{m,i}}{\Delta r} = -D_{b,i}\frac{0\,\text{mol}\,\text{m}^{-3} - K_i^{mb} \,/\, c^{\text{mb,int}}_{m,i}}{200\,\mu\text{m}} \tag{4.6}$$

$$\frac{\mathrm{d}N_{m,i}}{\mathrm{d}t} = \int_0^{A^{\text{int}}_{s,gm}} J^{\text{int}}_{i,gm}\,\mathrm{d}A^{\text{int}}_{s,gm}\Bigg|_{r=r^{\text{int}}_{gm}} - \int_0^{A^{\text{int}}_{s,mb}} J^{\text{int}}_{i,mb}\,\mathrm{d}A^{\text{int}}_{s,mb}\Bigg|_{r=r^{\text{int}}_{mb}} = 0 \tag{4.7}$$

For modelling a closed-end fibre, some boundary conditions needed to be changed in the gas phase. At the inlet, the flow cannot be regulated using a mass flow controller (Equation 2.30), but instead with a pressure controller, to keep the pressure at the inlet constant (Equation 4.8). At the end of the fibre, the flow cannot leave anymore, causing that both the gas flow velocity and the species flux are zero (Equation 4.9). All other equations, boundary conditions and parameters are the same as in the model described above.

$$p_g(z=0) = \Delta p_g + p_{ref} \tag{4.8}$$

$$u_{g,z}(z=L_f) = 0\,\text{m}\,\text{s}^{-1} \quad \text{and} \quad J^{\text{diff}}_{g,i}(z=L_f) = 0\,\text{mol}\,\text{m}^{-2}\,\text{s}^{-1} \tag{4.9}$$

4.3. Results and discussion

After solving the model described above, mass balances were checked and approximated zero (Table A.5). The concentrations in the membrane and gas phase were plotted as concentration profile (Figure 4.1), relative to the maximum amount of each compound in the gas phase (Equation 4.10). It was observed that the maximum concentrations in the gas phase were lower than the maximum concentrations obtained in the gas phase model (see Figure 3.2). These lower concentrations are expected to be due to less transfer of CO_2. This causes that there is a smaller increase in the mole fractions of the other compounds, leading to lower maximum concentrations. This lower mass transfer rate also causes that the concentration differences between the gas inlet and outlet are lower: For CO_2 this difference decreased from 55% to 21%.

From Figure 4.1 can also be observed that the concentrations decrease along the radial direction of the membrane for all compounds. However, the pattern of this decrease heavily depends on the concentrations in the gas phase. For example, the pattern of CO_2 is completely different than the pattern of CO. The CO_2 concentration decreases with 21% in the axial direction of the gas phase, while the concentration of CO increases with around 5%. This indicates that, as was expected in the previous Chapter 3, the concentrations at the membrane-biofilm interface will depended on the concentration profile in the gas phase and are not the same along the axial direction.

$$\tilde{c}_{g,i} = \frac{c_{g,i}}{\max\left(c_{g,i}\right)} \quad \text{and} \quad \tilde{c}_{m,i} = \frac{c_{m,i}}{K_i^{mg}\max\left(c_{g,i}\right)} \tag{4.10}$$

$$\Delta c_{m,i} = c^{\text{gm,int}}_{m,i,av} - c^{\text{mb,int}}_{m,i,av} \quad \text{with} \quad c^{\text{k,int}}_{m,i,av} = \frac{\int_0^{A^{\text{int}}_{s,k}} J^{\text{int}}_{i,k}\,\mathrm{d}A^{\text{int}}_{s,k}}{\int_0^{A^{\text{int}}_{s,k}} \mathrm{d}A^{\text{int}}_{s,k}} \quad \text{with k = [gm,mb]} \tag{4.11}$$

$$\Delta\tilde{c}_{m,i} = \frac{c^{\text{gm,int}}_{m,i,av} - c^{\text{mb,int}}_{m,i,av}}{c^{\text{gm,int}}_{m,i,av}} \tag{4.12}$$

The radial concentration difference differs per compound, therefore the absolute and relative average concentration difference across the membrane were calculated, the latter is normalized to the concentration at the gas-membrane interface (Equations 4.11 and 4.12). For CO_2, the concentration loss is significant:

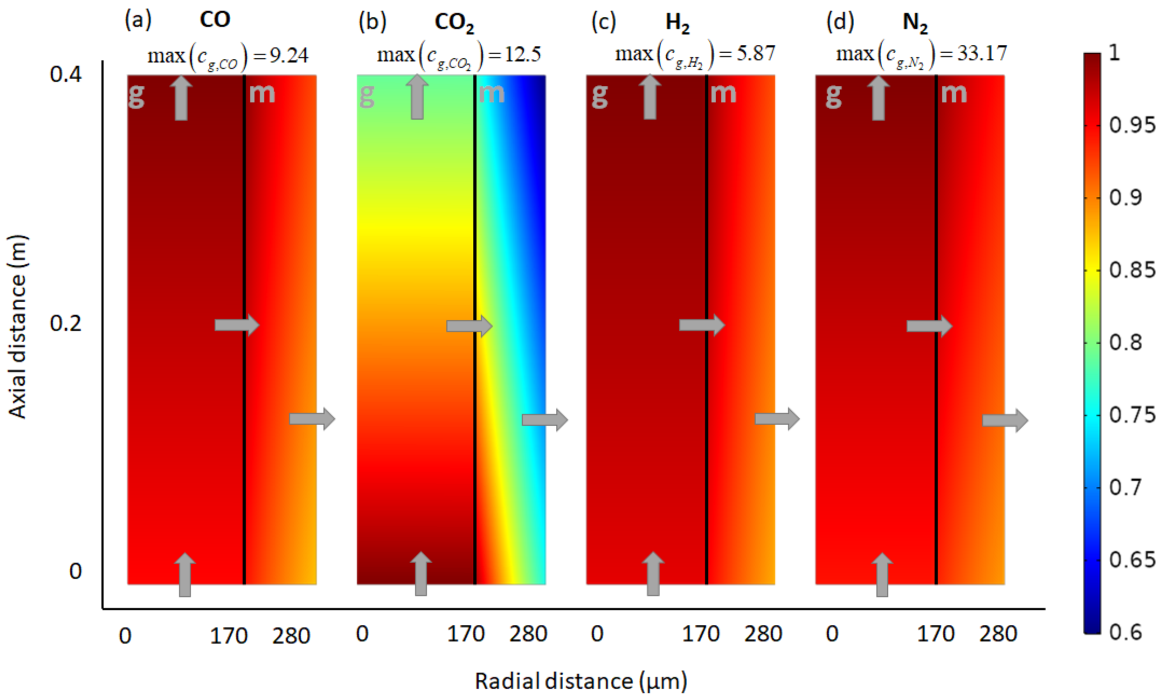

Figure 4.1: Normalized concentration profiles of (a) CO, (b) CO_2, (c) H_2 and (d) N_2 are plotted along the radial and axial direction in the gas and membrane phases. Concentrations have been normalized using Equation 4.10. The black lines depict the gas-membrane interface. The maximum concentrations of all compounds are provided in $\mathrm{mol\,m^{-3}}$. The gas and membrane domains are depicted with *g* and *m*. The gas inlet, outlet and the direction of transport across the membrane are depicted with the corresponding arrows.

around 25% and corresponds to around $3.5\,\mathrm{mol\,m^{-3}}$. For H_2 the absolute decrease is less significant as the concentrations are low, but there is still a decrease of 8%. The absolute decrease follows the same pattern as the fluxes (Figure 4.2): The species with a higher flux also have an increased absolute concentration difference across the membrane.

It is interesting to note that despite its higher permeability through the membrane the concentration loss of CO_2 is high. The compounds with a lower permeability (H_2, CO and N_2) show a lower radial concentration decrease. This implies that there could be a trade-off between high flux through the membrane and the concentration decrease. In the case the aim is to obtain high concentrations at the membrane-biofilm interface, one could choose for a membrane which is thinner or one with a lower permeability.

Next to this, the species fluxes have been plotted at the gas-membrane and at the membrane-biofilm interface along the axial direction of the fibre (Figure 4.2). The fluxes follow the same pattern as was observed in Figure 3.1a: The CO_2 flux decreases along the fibre length due to its decreasing concentration. The values of the fluxes of the other compounds are lower, but increase along the fibre length due to their increasing concentration. In all cases, the flux at the outer side of the membrane is observed to be lower than the flux at the gas-membrane interface, which is due to the cylindrical nature of the hollow fibre membrane.

Following Equation 4.5, the flux at the membrane-biofilm interface should equal $0.607 J_{i,gm}^{\mathrm{int}}$. This seems to be the case by comparing the fluxes at both interfaces. This indicates that the flux decreases with around 40% due to cylindrical nature of the system. The same amount of mass transferred needs to be distributed along a greater surface area. This decreases the flux and thus the potential highest concentration at the outer membrane interface. In the case the membrane would be flat, the flux would not have been decreased as the surface areas are equal at both interfaces.

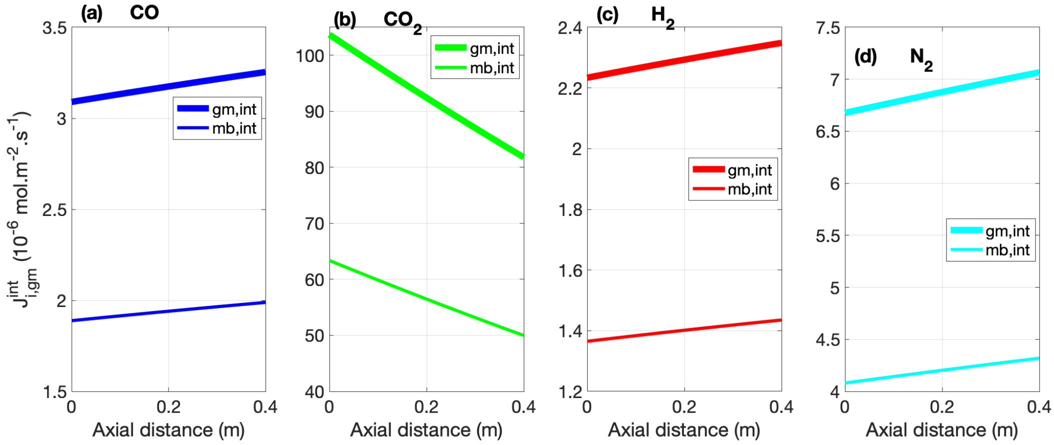

Figure 4.2: Mass fluxes of (a) CO, (b) CO_2, (c) H_2 and (d) N_2 are plotted along the axial direction of the fibre at the gas-membrane and membrane-biofilm interfaces. The flux at the gas-membrane interface has been depicted with thicker lines than the flux at the membrane-biofilm interface. The fluxes are plotted in $10^{-6}\,\mathrm{mol\,m^{-2}\,s^{-1}}$.

This illustrates that the thickness of the membrane directly influences the flux across the membrane. A thinner membrane would lead to smaller differences in fluxes, and thereby cause higher concentrations at the outer side, compared to a thicker membrane. However, it needs to be taken into account that there could be a possible trade-off between membrane thickness and reaction rate. A thicker membrane causes a higher surface area, and thus enables more biofilm to grow on the same membrane. This would lead to higher volumes of biomass around the membrane and could potentially increase the reaction rate.

Important to note is that the flux to the biofilm was calculated in an arbitrary way: the thickness of the biofilm, the biofilm diffusivity factor and the bulk concentration ($0\,\mathrm{mol\,m^{-3}}$) were all assumed. Although this is unrealistic, this was still necessary for developing the model and for comparing the species fluxes and concentration profiles.

Influence of gas flow rate

First, the closed-end fibre model was solved and results in terms of mass transfer rate (Equation 3.6) and yield (Equation 3.7) were calculated (Figure 4.3a). The mass transfer yield of all species was observed to be 100%: All gas entering the lumen is indeed transferred through the membrane.

At 10 cm from the inlet, all CO_2 was already transferred to the membrane, (Figure 4.3b). This leads to increased concentrations of the other compounds in the fibre. Therefore, this closed-end configuration causes that the compounds with a low membrane permeability accumulate in the lumen.

The gas phase velocity (Figure 4.3c) decreases to zero. It is clear that gas is transported to the fibre and that most of the mass transfer takes place at the beginning of the fibre. The gas velocity and flow rate are very low in the whole module (near the entrance around $1.5\,\mathrm{mm\,s^{-1}}$ or $4.62\,\mathrm{mL\,min^{-1}}$). This low flow rate causes that less gas enters the lumen compared to open-end configurations with higher flow rates, inducing a lower mass transfer rate. Next to this, the influence of the volumetric gas flow rate $F_{g,in}$ on the mass transfer rate and yield was examined. The gas flow rate was varied between 4.62 and $400\,\mathrm{mL\,min^{-1}}$ (Figure 4.4a and b). The model did not converge for flow rates lower than $4.62\,\mathrm{mL\,min^{-1}}$. This implies that the lowest possible operational flow rate equals the flow rate of the closed-end reactor model. Figure 4.4b suggests the same: the yield equals around 100%, similar to the closed-end fibre.

From these results, it was observed that there is a trade-off between mass transfer rate and mass transfer yield. At low flow rates, the mass transfer yields reach 100%, while the mass transfer rates are below their maximum. For CO and H_2, the maximum rates could be higher at moderate gas flow rates: around 20% (at

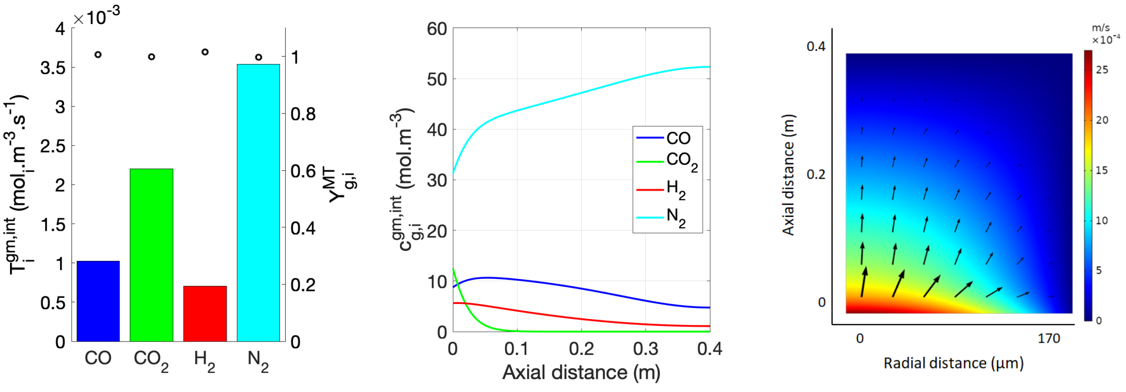

(a) (b) (c)

Figure 4.3: For the closed-end fibre, (a) the mass transfer rates and yields are depicted. The rates are displayed in the bars and the yields with the circles. (b) The gas concentrations at the gas-membrane interface $c^{\text{gm,int}}_{g,i}$ in the axial direction (in mmol m^{-3}) (c) and the gas velocity in the lumen are depicted (in m s^{-1}). The arrows in (c) indicate the gradient of the gas phase velocity.

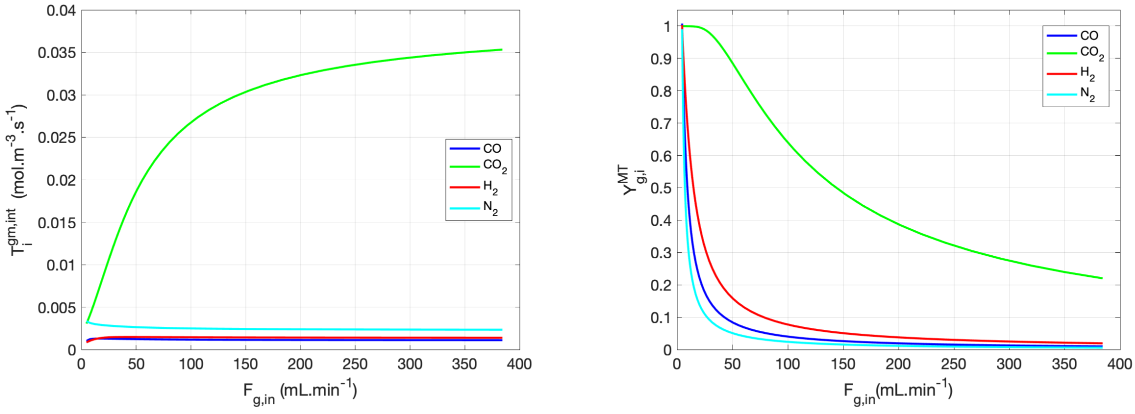

(a) (b)

Figure 4.4: For different inlet flow rates the (a) mass transfer rate from the gas phase to the membrane (in mmol m^{-3} s^{-1}) (b) and the mass transfer efficiencies (in %) are given.

17 mL min^{-1}) and 40% higher (at 42 mL min^{-1}), respectively. However, this is at the expense of the the mass transfer yield, which are higher at gas lower flow rates From these results was concluded that a lower gas flow rate (20 mL min^{-1}) should be used in upcoming models.

Last but not least, if one aims to permeate the electron-rich compounds (CO and H_2), one should investigate which membranes have high permeability for those instead of CO_2. PDMS offers high mass transfer rates and yields for CO_2, but lower rates and yields for the other compounds. Next to this, as the fluxes are partially a function of the composition in the gas phase, the mass transfer rate and yield also highly depend on the used syngas composition.

4.4. Conclusion

The gas phase model was successfully extended with the membrane compartment. It was found that there could be a high concentration loss (up to 20%) in the radial direction between the gas-membrane and the membrane-biofilm interface. Next to this, large differences at the membrane-biofilm interface were observed in the axial direction for CO_2: Its concentration near the fibre inlet was around 20% higher than at the outlet. This indicates that uniform membrane concentrations in both the radial and axial direction could not be assumed while modelling dense HFM modules, such as the one investigated module.

It was observed that the membrane parameters as diffusivity and the partition coefficient influences the decrease in concentrations across the membrane. A high permeability was related to higher flux and to higher concentration losses. This means that the choice of the membrane should be based on the compound that needs to be transferred, and whether high flux or high concentrations are aimed for. Modelling the membrane provided thereby insights in how the membrane properties influence the flux and concentrations of the species in the gas and membrane compartments.

Next to this, it was observed that the thickness of the membrane has a direct influence on the mass flux. Thicker hollow fibre membranes lead to lower fluxes and lower concentrations at the membrane-biofilm interface, compared to thinner membranes. Thereby a possible trade-off was discussed between surface area for biofilm growth and reaction rate and the necessary concentrations at that surface.

Lastly, it was found that closed-end fibres could be beneficial when high syngas transfer yields are required. However, this high yield is at the expense of the mass transfer rate, which significantly decreased compared to open-end fibres (up to 20% for CO and 40% for H_2). By varying the gas flow rate in the lumen, it was derived that high gas flow rates lead to lower mass transfer yields while it could increase the mass transfer rate. It was found that the transfer potential of CO_2 is much higher than the one of the desired compounds CO and H_2, implying that other membrane materials than PDMS could enhance the transfer of these compounds.

5

Liquid and biofilm phases

In this chapter, the membrane model (M_membrane) is extended with biofilm and the liquid compartments. Several different models are developed in order to describe the different phenomena in each phase and to predict the influence of varying parameters. First, a model without biomass and without biofilm is developed in order to describe mass transfer from the gas phase to the liquid phase. Thereupon, the overall volumetric mass transfer coefficient $k_{L,CO}^{ov}a$ can be calculated and compared with abiotic experiments performed in HFM reactors (from literature). Secondly, this abiotic model is extended with suspended biomass to estimate the productivity of ethanol fermentation in a HFM module without biofilm at varying biomass concentrations. The third model contains a biofilm and makes it possible to compare reactor configurations with suspended biomass and biofilm. This comparison will be made in order to describe whether biofilm formation is preferred over suspended biomass.

Biofilm growth and detachment has been investigated and modelled. Due to the lack of information on the biofilm, it is not detailed described here and not taken into account in the model with biofilm. More information on the theories behind biofilm growth and detachment can be found in Appendix G.

5.1. Theory

Mass transfer

Mass transfer from gas to liquid in membrane contractors is extensively studied before. The general approach to describe the overall mass transfer coefficient $k_{L,i}^{ov}$ is based on the resistance-in-series model. The overall mass transfer resistance is thus the sum of all mass transfer resistances (Equation 5.1). The overall mass transfer coefficient can be calculated using Equation 5.2 for a flat membrane and Equation 5.3 for a HFM, for which a correction for the cylindrical nature is applied (Drioli et al., 2006; Atchariyawut et al., 2008).

$$R_{OV,i}^{MT} = R_{g,i}^{MT} + R_{m,i}^{MT} + R_{l,i}^{MT} \tag{5.1}$$

$$\frac{1}{k_{L,i}^{ov}} = \frac{K_i^{lg}}{k_{g,i}} + \frac{K_i^{lg}}{k_{m,i}} + \frac{1}{k_{l,i}} \tag{5.2}$$

$$\frac{1}{k_{L,i}^{ov}(d_i + 2d_m)} = \frac{K_i^{lg}}{k_{g,i}d_i} + \frac{K_i^{lg}}{k_{m,i}d_{ln}} + \frac{1}{k_{l,i}(d_i + 2d_m)} \quad \text{with} \quad d_{ln} = \frac{(d_i + 2d_m) - d_i}{\ln \frac{(d_i+2d_m)}{d_i}} \tag{5.3}$$

It can be expected that the liquid and membrane mass transfer coefficients are the limiting factors for mass transfer in HFM contactors (Drioli et al., 2006). Orgill et al. (2013) argue that at low liquid velocities the liquid phase resistance dominates mass transfer, while at higher velocities the membrane is limiting (for O_2 transfer through PDMS membranes). The liquid phase is expected to be laminar (Appendix D.3) and radial diffusion is expected to dominate axial convection (Appendix B and D.3). This could lead to a thick hydrodynamic boundary layer, causing that radial diffusion in the liquid could become the limiting factor at low liquid flow velocities, decreasing the overall mass transfer rate.

In case a biofilm is present, an additional term needs to be added for the resistance in the biofilm $R_{b,i}^{MT}$. Diffusion coefficients of gas species in the biofilm are proportional to these in water. Matson and Characklis (1976) found that oxygen in microbial aggregates diffuses 20% to 100% slower in water. The diffusivity factor of solutes through *Clostridium* biofilms are unknown thus far. A correction factor f_B is 0.8 has been assumed, so that biofilm diffusivity is 20% lower than water diffusivity. The diffusion coefficients in the biofilm and in water are calculated in Appendix D.3.

CO-conversion

Prior to developing these models, the stoichiometry and kinetics of the organism were calculated. The stoichiometry was calculated based on the generalized thermodynamic approach (Kleerebezem and Van Loosdrecht, 2010) (Appendix F). Kinetics were based upon the kinetic model for *Clostridium ljungdahlii* developed by Mohammadi et al. (2014). The method they used to derive the kinetics could be questionable, as the authors only measured gas phase concentrations and assumed that they were representative. However, it is the only useful available kinetic model for *Clostridium* spp. The other models found in literature were dimensionless (Chen et al., 2018), growth-based, neglecting maintenance at low CO concentrations (Younesi et al., 2005) or were only valid for chain-elongation based on H_2 uptake in co-cultures (Chen and Ni, 2016).

The parameters found by Younesi et al. (2005) and Li and Henson (2019) showed a small inhibitory effect of CO ($K_{I,CO}$ were 2 and $5\,\mathrm{mol\,m^{-3}}$, respectively), compared to the inhibition found by Mohammadi et al. (2014) ($K_{I,CO} = 0.5\,\mathrm{mol\,m^{-3}}$). The latter is the more realistic value as the former values correspond to high CO-pressures (larger than 2 atm) and it is known that CO inhibits growth of *Clostridium* spp. at lower concentrations (Kim et al., 1984; Meyer et al., 1985). Medeiros et al. (2019) tried to derive kinetic parameters from experimental studies. After comparing all kinetic parameters, can be derived that that the kinetic model for CO uptake derived by Mohammadi et al. (2014) is the most acceptable (see Table F.1).

The kinetic model derived by Mohammadi et al. (2014) was assumed to be valid for ethanol-producing *C. autoethanogenum*, both for suspended biomass and in biofilms. The CO-uptake rate is maximum at a dissolved CO concentration of $0.09\,\mathrm{mol\,m^{-3}}$ with a rate of $0.025\,\mathrm{mol_{CO}\,g_x^{-1}\,h^{-1}}$, and gets inhibited at higher CO concentrations: At the CO solubility ($0.85\,\mathrm{mol\,m^{-3}}$), the uptake rate decreases to $0.015\,\mathrm{mol_{CO}\,g_x^{-1}\,h^{-1}}$ (Figure F.2b). In literature, it has been found that, next to ethanol, this organism also produces acetate and 2,3-butanediol (Valgepea et al., 2018). In the developed (stoichiometric) models, only ethanol formation was taken into account from pure CO gas streams. This is done as it is known that one could produce mainly ethanol from *C. autoethanogenum* (e.g. LanzaTech, after strain engineering) (Abubackar et al., 2011) and as Phillips et al. (1993) was also able to produce ethanol with high selectivity (21 mol ethanol per mol acetate) from *C. ljungdahlii.* The derivations of the overall stoichiometry and the kinetic models are discussed in Appendix F.

After calculating the characteristic times in the biofilm, it was expected that reaction and biofilm diffusion would be in the same order of magnitude (Appendix B). This means that factors as the CO concentration in the biofilm, the biofilm biomass concentration and thickness, could have a large impact on the overall performance of the HFM reactor.

A biofilm could decrease the CO diffusion distance and increase the biomass concentration in the module, compared to systems with suspended biomass configurations. Hence, biofilm formation could lead to higher volumetric productivities. However, when biomass is suspended, there is more volume for the biomass available, and diffusion in the liquid phase is faster than in a biofilm, implying that in some cases, suspended biomass could be more productive than biomass in a biofilm. Values commonly reported in literature for the biomass concentration in biofilms grown in HFM reactors range between $15\,\mathrm{kg\,m^{-3}}$ (Pavasant et al., 1996), $30\,\mathrm{kg\,m^{-3}}$ (Picioreanu et al., 2001; Martin et al., 2013) and $50\,\mathrm{kg\,m^{-3}}$ (Matsumoto et al., 2007). The highest value reported for the suspended biomass concentrations in a CSTR with HFM cell retention system for *C. ljungdahlii* was $10\,\mathrm{kg\,m^{-3}}$ (Richter et al., 2013). However, it needs to be taken into account that high suspended biomass concentrations substantially increase the viscosity of the broth. Blunt et al. (2019) found that concentrations up to $25\,\mathrm{g_x\,L^{-1}}$ of polyhydroxyalkanoate producing *Psuedomonas putida* increased the broth viscosity up to a nine-fold. Therefore, the suspended biomass concentration was varied up to $10\,\mathrm{g_x\,L^{-1}}$ (for which a 2.5 time viscosity-increase can be expected).

5.2. Model development

All the described models in this chapter were developed by extending the membrane model (M_memb). Next to this, some characteristics were kept constant, unless otherwise mentioned:

- The gas flow rate $F_{g,in}$ through the lumen is $20\,\mathrm{mL\,min^{-1}}$.
- Pure CO is fed from the gas phase.
- The shell liquid $F_{l,mod,in}$ is $200\,\mathrm{mL\,min^{-1}}$.
- Solute concentrations in the liquid inlet are $0\,\mathrm{mol\,m^{-3}}$.
- Effects of suspended biomass on the liquid viscosity were not taken into account.
- Ethanol inhibition was not taken into account.
- Water and ethanol evaporation were neglected.

In all cases, the liquid flow was modelled by assuming laminar flow of water ($Re \approx 11$, Appendix D.3). The *laminar flow* interface was used for solving liquid momentum and mass continuity (Equations 2.32 and 2.31). Used boundary conditions were given by Equations 2.33, 2.34, 2.35 and 2.36.

Solutes transport in the liquid was modelled using the *transport of diluted species* interface, which solves Equation 2.17. A Danckwerts boundary condition was used (Equation 2.18). Other boundary conditions in the liquid phase were Equations 2.19 and 2.21. When no biofilm was present, the flux and concentrations at the membrane-liquid interface were described according to Equations 2.12 and 2.16, while changing the biofilm-based parameters to liquid-based parameters (i.e. $D_{l,i}$ instead of $D_{b,i}$).

When present, solutes transport in the biofilm was modelled with the *transport of diluted species* interface (Equation 2.13), with boundary conditions being Equations 2.12, 2.14 and 2.16, and no flux at $z = 0$ and $z = L_f$.

In the models developed in this chapter, ethanol inhibition was not taken into account. Although it is known that ethanol is inhibitory to *Clostridium*, no liquid recirculation was incorporated in this model, preventing higher ethanol concentrations. Next to this, the biofilm thickness ($100\,\mu\mathrm{m}$), biomass concentration ($15\,\mathrm{kg\,m^{-3}}$), its biomass distribution (equally distributed), and shape (flat) are unknown and assumed.

Mass balances in these models were analysed similar to the mass balances in the gas and membrane models (Equations 3.5 and 4.7). The mass balances in the biofilm and liquid phases were analysed using Equations 5.4 and 5.5, with the reaction term in brackets as this was only valid in cases with suspended biomass. The models and the parameters which were varied in these models as well as the values of these parameters used

Table 5.1: For the developed models, it is tabulated whether biomass is present and which parameters were varied. The base value of a certain parameter is the value of that parameter as used in the other models. The module liquid flow rate $F_{l,mod,in}$ was changed based on the liquid Reynolds number. The base value for this flow rate was 200 mL min^{-1}, which corresponds with to $Re_l = 4.34$.

Model	Biomass	Variable	Base value	Lower value	Upper value	Unit
M_liq_kla_xCO	No biomass	$x_{CO,in}$	1	10^{-8}	1	$\mathrm{mol_{CO}\,mol_g^{-1}}$
M_liq_kla_Re	No biomass	Re_l	4.34	0.1	10	$\mathrm{mL\,min^{-1}}$
M_liq_susp	Suspended	$c_{l,x}$	0	0.1	10	$\mathrm{kg\,m^{-3}}$
M_biof_cx	Biofilm	$c_{b,x}$	15	1	60	$\mathrm{kg\,m^{-3}}$

in the other models are described in Table 5.1. Next to this, the width of the liquid compartment changes as function of the biofilm thickness (Equation 5.6).

$$\frac{\mathrm{d}N_{b,i}}{\mathrm{d}t} = \int_0^{A_{s,mb}^{\mathrm{int}}} J_{i,mb}^{\mathrm{int}}\,\mathrm{d}A_{s,mb}^{\mathrm{int}}\bigg|_{r=r_{mb}^{\mathrm{int}}} - \int_0^{A_{s,bl}^{\mathrm{int}}} J_{i,bl}^{\mathrm{int}}\,\mathrm{d}A_{s,bl}^{\mathrm{int}}\bigg|_{r=r_{bl}^{\mathrm{int}}} + \int_0^{V_b} q_i c_{b,x}\,\mathrm{d}V_b = 0 \tag{5.4}$$

$$\frac{\mathrm{d}N_{l,i}}{\mathrm{d}t} = \int_0^{A_{c,l}} \boldsymbol{u_l} c_{l,i}\,\mathrm{d}A_{c,l}\bigg|_{z=0} + \int_0^{A_{s,bl}^{\mathrm{int}}} J_{i,bl}^{\mathrm{int}}\,\mathrm{d}A_{s,bl}^{\mathrm{int}}\bigg|_{r=r_{bl}^{\mathrm{int}}} - \int_0^{A_{c,l}} \boldsymbol{u_l} c_{l,i}\,\mathrm{d}A_{c,l}\bigg|_{z=L_f} + \left(\int_0^{V_l} q_i c_{l,x}\,\mathrm{d}V_l\right) = 0 \tag{5.5}$$

$$d_l = \frac{1}{2} d_{\mathrm{spacing}} - d_b \tag{5.6}$$

In the models without biomass, the $k_{L,i}^{ov}a$ was calculated according to Equation 5.7, which is based on the definition that the total mass transfer rate is a function of the volumetric mass transfer coefficient and the concentration gradient. In the models with biomass, the shell volume-specific productivity of the system was calculated (Equation 5.8) as well as the average biomass-specific productivity (Equation 5.9).

$$k_{L,i}^{ov}a = \frac{T_i^{ml,int}}{\Delta c_i} = \frac{\displaystyle\int_0^{A_{s,ml}^{\mathrm{int}}} J_i^{\mathrm{ml,int}}\,\mathrm{d}A_{s,ml}^{\mathrm{int}}\,\frac{N_f}{V_{\mathrm{shell}}}}{c_{g,i}^{\mathrm{gm,int}} \times K_i^{lg} - c_{l,i}^{\mathrm{ml,int}}} \tag{5.7}$$

$$P_{V,i} = \int_0^{V_k} q_i c_{k,x}\,\mathrm{d}V_k\, M_i \frac{N_f}{V_{\mathrm{shell}}} \quad \text{with} \quad k = [b, l] \tag{5.8}$$

$$P_{x,i} = \frac{\displaystyle\int_0^{V_k} q_i c_{k,x}\,\mathrm{d}V_k\, M_i}{\displaystyle\int_0^{V_k} c_{k,x}\,\mathrm{d}V_k} \quad \text{with} \quad k = [b, l] \tag{5.9}$$

5.3. Results and discussion

$k_{L,CO}^{ov}a$ determination

In the models without biomass, the $k_{L,CO}^{ov}a$ was calculated according to Equation 5.7, which is based on the definition that the total mass transfer rate is a function of the volumetric mass transfer coefficient and the concentration gradient. The total mass transfer rate was calculated as the amount transferred from the membrane to the shell, in the whole HFM module. By changing the liquid flow rate, based on its Reynolds number, the results can be compared with experiments performed with other membrane modules. When gas was undiluted (100% CO), the obtained volumetric mass transfer coefficient was very low $k_{L,CO}^{ov}a = 40\,\mathrm{h^{-1}}$ (Figure 5.1a). This is due to the low mass transfer rate, as the maximum solubility in the water was reached. In these cases, the driving force for mass transfer was low, decreasing the need for large mass transfer rates to dissolve all CO in the water. By decreasing the amount of CO in the gas phase, the maximum solubility will not be reached, increasing the mass transfer rate. When the CO fraction in the gas phase gets lower than 70%, there is a constant mass transfer rate as all CO can dissolve in the water in these cases (Figure 5.1a). In these cases,

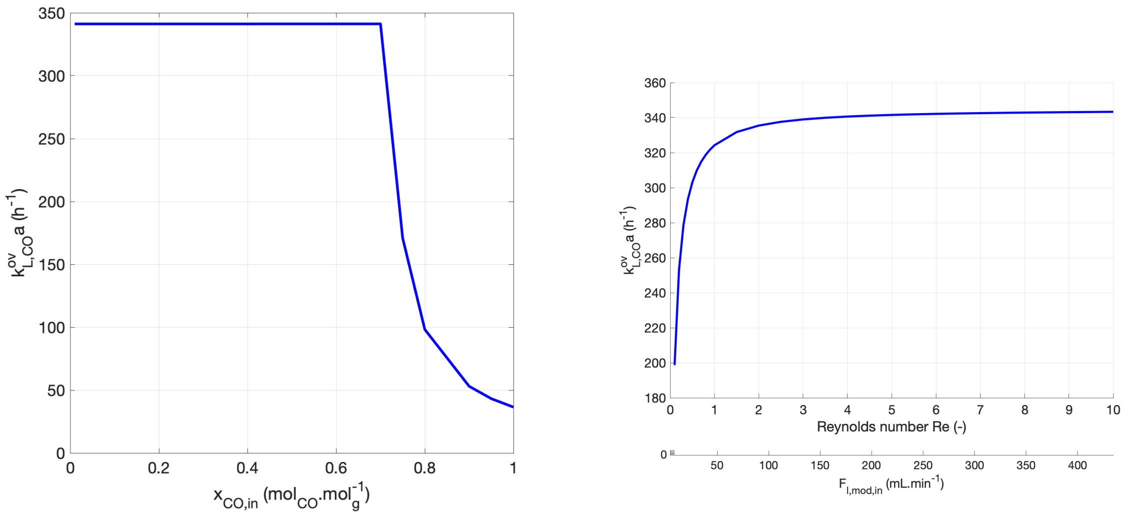

(a) (b)

Figure 5.1: (a) The $k^{ov}_{L,CO}a$ was calculated for varying inlet CO fractions, with a constant Reynolds number of 4.6 (M_liq_kla_xCO) ($F_{l,mod,in}$ = 200 mL min^{-1}). (b) The $k^{ov}_{L,CO}a$ is calculated for different liquid flow rates, represented by the Reynolds number and the liquid flow rate into the module, with a constant CO inlet molar fraction of 0.5 (M_liq_kla_Re). No biofilm or suspended biomass was taken into account in this model.

the $k^{ov}_{L,CO}a$ does not increase by decreasing the inlet CO fraction, which could indicate that the maximum mass transfer rate is reached and the mass transfer is limited by the constant resistance in the membrane.

When the Reynolds number was increased, the mass transfer coefficient increased as well (Figure 5.1b). This increase is due to larger convection rates as this causes a smaller boundary layer near the membrane side. A smaller liquid boundary layer leads to less diffusion in the liquid phase and thus increases the mass transfer rate and its coefficient. When Re approached 3, the slope of the mass transfer coefficient increase diminished: a maximum $k^{ov}_{L,CO}a$ of 343 h^{-1} was obtained. In these cases, the change of the thickness of the liquid boundary layer becomes lower at increased flow velocities, indicating that the liquid resistance decreases and that the membrane is the main resistance for mass transfer. Orgill et al. (2019) obtained the $k^{ov}_{L,CO}a$ of their PDMS HFM module, by modelling and performing experiments. The results they obtained for different Reynolds numbers are analogous to the results which were obtained in Figure 5.1b.

With the same procedure, the $k^{ov}_{L,\mathrm{N_2}}$ was calculated as well. From these values for both CO and N_2, the mass transfer coefficient in the liquid phase $k_{l,i}$ was back-calculated using Equation 5.3, for different values of Re. $k_{g,i}$ and $k_{m,i}$ were calculated using Equations 3.1 (with $Sh = 3.67$) and 4.3. The gas mass transfer resistance for both compounds was found to be negligible (around 10^2 s m^{-2}). The different values obtained for the mass transfer resistances (in the membrane and the liquid) as well as the overall mass transfer resistance are depicted in Figure 5.2a and b. From this was observed that for both compounds, the mass transfer resistances in the liquid and the membrane are in the same order of magnitude. When Re is very low, the mass transfer in the liquid phase is limiting for N_2, but not for CO, as CO has a slightly higher liquid diffusivity. As N_2 has a lower K^{mg} and K^{lg} than CO, its membrane resistance is lower, so that its overall mass transfer resistance could become slightly lower than the one of CO.

From this was observed that at low Re (when $Re < 3$ or $F_{l,mod,in} < 150$ mL min^{-1}) mass transfer in the liquid phase decreases the overall mass transfer rate, while at high Re the membrane becomes the limiting factor. This is important to take into account while working with suspended biomass. At high shell liquid flow

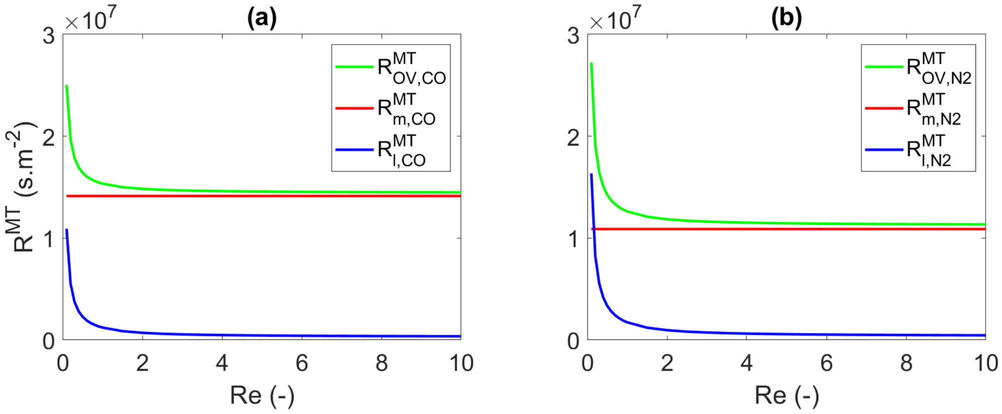

Figure 5.2: For both (a) CO and (b) N_2 transfer from gas to liquid, the mass transfer resistances were calculated in the HFM module. The overall, membrane and liquid resistances were plotted for different values of the Reynolds number. The gas phase mass transfer resistance was found to be negligible. Results were derived from model M_liq_kla_Re ($x_{CO,in} = 0.5$).

Table 5.2: Comparison of mass transfer coefficients in different HFM configurations.

Study[a]	Membrane type[b]	Operating conditions	a (m^{-1})	$k^{ov}_{L,CO}a$ (h^{-1})	$k^{ov}_{L,CO}$ ($cm\,h^{-1}$)
[1]	Dead-end composite, PU (40 µm)	$\Delta p = 2.04$ atm Re = 25	2645	946.6	35.8
[2]	Open end microporous, PP (40 µm)	$\Delta p = 1.02$ atm Re = 27	100	1096.2	627
[3]	Submerged microporous, PVDF (500 µm)	$\Delta p = 0.37$ atm Re = N/A	62.5	155	248.3
[4]	Dense PDMS (100 µm)	Δp = N/A Re = 3.5	10000	420	4.20
This study (100% CO)	Dense PDMS (110 µm)	Δp= 0.5 atm Re = 2.3	774	40	5.16
This study (50% CO)	Dense PDMS (110 µm)	$\Delta p = 0.5$ atm Re = 2.3	774	343	44.3

a) [1]: Munasinghe and Khanal (2012), [2]: Shen et al. (2014b), [3]: Yasin et al. (2014), [4]: Orgill et al. (2019). All used 100% CO in the gas inlet.
b) PU: polyurethane, PP: polypropylene, PDMS: polydimethylsiloxane, PVDF: Polyvinylidene fluoride

rates radial diffusion could become a problem, causing that not all biomass in the shell receives CO. While at lower flow rates, the mass transfer rate will be lower, causing lower amounts of dissolved CO. Next to this, it is also important to note that in some cases, working with dense HFM modules for gas-liquid contacting could decrease the overall mass transfer rate as the membrane resistance could dominate. As the residence time of suspended biomass is a function of the liquid flow velocity, there is a narrow range of shell liquid velocity for optimum mass transfer and conversion.

The obtained results at CO inlet fractions of 0.5 and 1 were compared with literature data (Table 5.2). From this data, it became clear that not only the $k^{ov}_{L,CO}a$ should be compared, but also the $k^{ov}_{L,CO}$ as some scholars used HFM configurations with very large surface areas which could be impossible to maintain during biotic conditions. Although these large surface areas lead to high $k^{ov}_{L,CO}a$ values, the required small fibre spacing, could increase clogging in the liquid and the pressure drop, and therefore diminish the reactor performance.

Comparing the results of this HFM module with other studies, it seems that the obtained $k^{ov}_{L,CO}$ values (5.16 and 44.3 $cm\,h^{-1}$, at 100% and 50% CO in the inlet, respectively), are similar to the values found by Munasinghe and Khanal (2012) and Orgill et al. (2019). It is hard to compare the results of this system with the systems of Shen et al. (2014b) and Yasin et al. (2014). The former based the surface area they provided on the total reactor volume and not on the total membrane surface area, as they pressurized the liquid reservoir

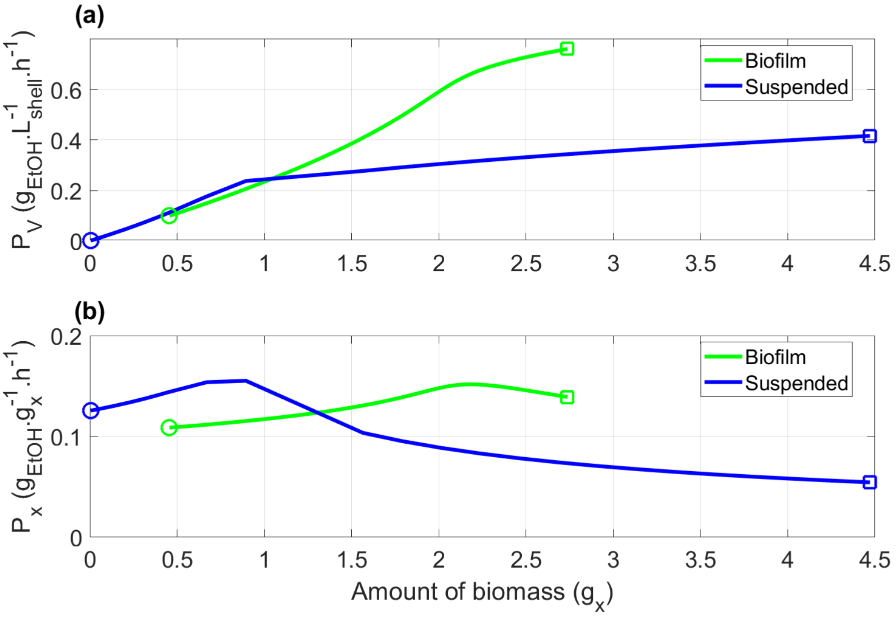

Figure 5.3: (a) The shell volume-specific productivity was calculated and (b) the biomass-specific productivity for different amount of suspended and biofilm biomass in the HFM module. Results were derived from models M_liq_susp and M_biof_cx. The circles depict the lowest and the squares the highest possible value used for the concentrations of biomass in the suspended and biofilm configurations (see Table 5.1). The biofilm thickness was fixed at 100 μm, pure CO was added in the gas phase and the module liquid flow rate $F_{l,mod,in}$ was fixed at 200 mL min^{-1} in all cases.

with the membrane off-gas. The latter used their microporous membrane to induce bubble formation and did not take the surface area of the bubbles into account by calculating their $k_{L,CO}^{ov}a$.

Biomass models

For the suspended biomass model and the biofilm model, the volume-specific and biomass-specific productivities were calculated and plotted against the amount of biomass in the module (Figure 5.3a and b). The amount of biomass in the module was chosen to correct for volume differences in the biofilm and liquid phases. From these results, it can be observed that the biomass-specific productivity reaches the same maximum values, but both at different amounts of biomass. Suspended biomass is the most productive at 1 g_x ($c_{l,x}$ = 2 g_x L^{-1}), whilst the biofilm is the most productive at 2.2 g_x ($c_{b,x}$ = 48 g_x L^{-1}). However, while operating at the maximum biomass productivity, the volume-specific ethanol productivity is sub-optimal, as can be found in Figure 5.3a.

From these figures becomes clear that a 100 μm biofilm could be beneficial for ethanol production, when it could retain more than 1.05 g_x in the module (or has a concentration of at least 23 g_x L^{-1}). If that biomass concentration could not be reached in the biofilm, then these results suggest that suspended biomass in a HFM module would cause the highest productivities.

The optimum in the biomass-specific productivity and the decline of the slope of the volume-specific productivity in both cases can be explained by investigating the characteristic times of reaction and radial diffusion (Figure 5.4). In the suspended biomass case, the time of reaction matches the time of radial diffusion in the liquid, when there is around 1 g_x in the module. With this biomass concentration, CO is able to diffuse through the whole liquid phase, so that all biomass can be used for reaction. At larger concentrations the biomass in the middle of the channel won't be exposed to CO as it has already been consumed by the biomass closer to the membrane. By increasing the biomass concentration, the mass transfer rate to the liquid phase can be increased, as the membrane is not limiting mass transfer.

In the biofilm case, the characteristic time of reaction equals the time of diffusion in the biofilm when the amount of biomass in the module has reached 2.2 g_x. At lower biomass concentrations, the system is limited by the kinetics of the organism (the reaction is too slow). By increasing the amount of biomass, the conversion capacity increases and only at higher amounts (more than 2.6 g_x ($c_{b,x} = 57\, g_x\, L^{-1}$)), the system becomes mass transfer-limited by the membrane. This means that between 2.2 and 2.6 g_x, not all CO reaches the biofilm-liquid boundary, so that there is less reaction per amount of biomass (i.e. lower P_x). However, in this case, the maximum capacity of the membrane has not been reached. This implies that the mass transfer rate of CO through the membrane can be increased by increasing the driving force. If there would be more biomass, the driving force would be increased, and thus the volumetric productivity.

It needs to be taken into account that for deriving these results, several uncertain assumptions were made (amongst others the microbe kinetics, diffusion in biofilm, and the biofilm thickness). Furthermore, practicalities as retention of suspended biomass, its influence on the liquid viscosity and possible channeling or fouling in the membrane module were not taken into account, but these could become serious issues when operating at high biomass concentrations. Therefore, one should not take these mentioned numbers as absolute, but the trends are expected to be the same: Higher amounts of biomass in biofilm lead to higher volumetric productivities than could be achieved with suspended biomass flowing through a HFM module.

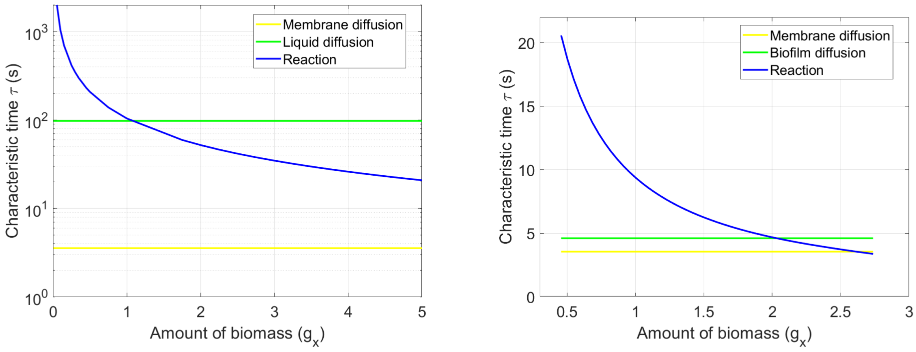

(a) (b)

Figure 5.4: For (a) the suspended biomass (M_liq_susp) and (b) the biofilm model (M_biof_cx), characteristic times were calculated for different amounts of biomass in the module. The characteristic times were calculated according to their equations in Appendix B. The biofilm thickness was fixed at 100 µm, pure CO was added in the gas phase and the module liquid flow rate $F_{l,mod,in}$ was fixed at 200 mL min^{-1} in both cases.

5.4. Conclusion

In this chapter, the maximum overall volumetric CO mass transfer coefficient $k_{L,CO}^{ov}a$ was calculated to be 343 h^{-1}, which was comparable with $k_{L,CO}^{ov}a$ values obtained for HFM modules in literature. Moreover, it was found that at low liquid flow rates, both the membrane and the liquid mass transfer resistances became limiting for mass transfer. At flow rates higher than 150 mL min^{-1}, the membrane became the dominating resistance for mass transfer.

From the performed analyses can be concluded that biofilms have the potential to reach higher volumetric productivities than suspended biomass, when their biomass concentration is higher than 23 $g_x L^{-1}$. This can be explained by the increased reaction rate due to the characteristic of biofilms to retain high biomass concentrations. In the operating window for suspended biomass (up to 10 $g_x L^{-1}$) was found that the mass transfer potential of the HFM module was not completely utilized, while biofilms with high biomass concentrations could enable the utilization of the complete mass transfer potential of the HFM module.

6

Reservoir

An external reservoir can be used in order to increase the product concentration, to enhance sampling and to limit the wash-out of fresh medium. Modelling the reservoir could give predictions in which circumstances this might be true. It would also provide insights in the effects of recirculation on the module performance.

6.1. Theory

In such a reservoir (see Figure 2.2), a fresh liquid inflow stream $F_{l,res,in}$ is added to refresh the reservoir and an outflow stream to simulate continuous behaviour. The reservoir is linked to the membrane module with two streams ($F_{l,mod,in}$ and $F_{l,mod,out}$). In order to release the dissolved gasses, a gas flow is added ($F_{g,res,in}$). A pressure release valve would also be sufficient, but then the gas flow cannot be used for measurements in the reservoir. A condenser is operated at 4 °C in order to condense evaporated water and ethanol prior to returning these into the reservoir.

An important parameter of the reservoir is the hydraulic retention time (HRT), which is defined according to Equation 6.1. The total liquid volume in the whole system is defined as the volume of the reservoir, the liquid in the membrane module and the connecting pipes. The volume of the pipes was neglected, while the volume of the biofilm was subtracted from the shell volume.

$$HRT = \frac{V_{l,\mathrm{tot}}}{F_{l,res,out}} = \frac{V_{res} + V_{mod} + V_{\mathrm{pipes}}}{F_{l,res,out}} = \frac{V_{res} + V_{shell} - V_{biof} + V_{\mathrm{pipes}}}{F_{l,res,out}} \tag{6.1}$$

Shen et al. (2014b) performed experiments with syngas fermentation in a HFM reactor with liquid recirculation in a reservoir. They used the lumen off-gas to pressurize the reservoir, which increased their $K_{L,CO}a$. They found that low reservoir dilution rates ($F_{l,res,out}/V_{res}$), increase the concentration of ethanol and acetate. Next to this, they found by varying the liquid recirculation flow rate ($F_{l,mod,in}$) that concentrations of ethanol decrease at relatively high module inflow rates, which they explained by additional biofilm detachment due to shear stress.

Results that are important to derive are the effects of these parameters on the shell volume-specific biofilm productivity of the system. This way it can be determined whether operation with reservoir could lead to differences in productivity and what the operating window is that results in the highest productivity. Next to that, operation with a reservoir can enable higher ethanol concentrations as ethanol is expected to accumulate in the system when the HRT is high. Therefore, the influence of the HRT on the ethanol concentration will be determined. High concentrations would lead to better downstream processing options so that the process efficiency can be increased. Furthermore, the concentration difference between the module outflow and the module inflow could be an interesting result as this could make it possible to perform calculations for validation of the model. For this, the flow rate through the module will be predicted as that could lead to considerable concentration differences between the in- and outflow.

6.2. Model development

The reservoir was incorporated in COMSOL by extending the biofilm models (M_biof_cx) with the equations that describe the reservoir (2.37-2.41). This way, the complete model described in Chapter 2 is obtained. Ethanol inhibition following the linear inhibition model (Appendix F) and evaporation of water to the lumen (see Appendix E) were taken into account. While developing this model, the following assumptions were made, which are discussed in Appendix H:

- The stirred reservoir is ideally mixed and in a steady-state.
- Reaction in the reservoir is considered to be negligible.
- Pressure and temperature in the reservoir remain constant.
- The density of the liquid phase always equals the density of water.
- The volume of the connecting pipes can be neglected.
- The reservoir inlet gas flow rate equals its outlet gas flow rate.
- Non-ideal behaviour in the reservoir can be neglected.
- Water evaporation in the reservoir is neglected.
- The volumetric mass transfer coefficient of the reservoir is $30\,\mathrm{h}^{-1}$.
- There is no nutrient limitation and pH can be controlled.

As there are several additional process variables that can be controlled in this configuration ($F_{g,res,in}$, $F_{l,res,in}$, $F_{l,mod,in}$ and V_{res}). Several analyses were performed in order to investigate the effect of changes in these process variables on the shell volume-specific biofilm productivity (Equation 6.2), ethanol titer ($c_{l,\mathrm{EtOH},res}$) and the concentration difference between the module in and outlet (Equation 6.3).

$$P_{V,i} = \int_0^{V_b} q_i c_{b,x} \,\mathrm{d}V_b \, M_i \frac{N_f}{V_{\mathrm{shell}}} \tag{6.2}$$

$$\Delta c_{i,mod} = c_{l,\mathrm{EtOH},mod,out} - c_{l,\mathrm{EtOH},mod,in} = \left. \frac{\int_0^{A_{c,l}} \boldsymbol{u_l} c_{l,EtOH} \,\mathrm{d}A_{c,l}}{\int_0^{A_{c,l}} \boldsymbol{u_l} \,\mathrm{d}A_{c,l}} \right|_{z=L_f} - c_{l,\mathrm{EtOH},res} \tag{6.3}$$

In Table 6.1 the window of operation used for all these parameters is tabulated. Parametric analyses within these windows were performed. By constraining the $F_{l,res,in}$ at $2\,\mathrm{mL\,min}^{-1}$, it was prevented that there is too much fresh water entering the system, which limits the usefulness of the reservoir system. For the biofilm, a thickness of 190 µm and biomass concentration of $15\,\mathrm{g\,L}^{-1}$ were used.

The initial goal was to perform simulations according to the Monte Carlo method in the COMSOL optimization toolbox. This analysis randomly varies the value of each variable for each simulation based on the provided window of operation (Table 6.1), so that between 100 and 1000 model simulations could be solved. As all these process variables are expected to have certain effects that influence each other, fixing the other variables in order to estimate the effect of one variable was considered less useful than randomly varying all variables and discovering trends. However, due to the additional relation for ethanol inhibition the system became highly non-linear, preventing the model to solve at high ethanol concentrations. This made it impossible to execute Monte-Carlo simulations to determine the influence of the additional reservoir parameters.

Table 6.1: The different models, associated with the different process parameters and their operating window and values are tabulated. The base value of each parameter was kept constant during variations of other parameters.

Model	Parameter	Symbol	Unit	Base value	Lower	Upper value
M_res_Fgresin	Reservoir gas flow rate	$F_{g,res,in}$	$\mathrm{mL\,min^{-1}}$	1	0.1	100
M_res_Flresin	Reservoir liquid flow rate	$F_{l,res,in}$	$\mathrm{mL\,min^{-1}}$	0.2	0.025	2
M_res_Flmodin	Module liquid flow rate	$F_{l,mod,in}$	$\mathrm{mL\,min^{-1}}$	150	0.4	500
M_res_Vres	Reservoir volume	V_{res}	L	0.5	0.25	1.5

In order to derive the influence of the additional parameters on the performance of the HFM reactor, they were varied according to the ranges described in Table 6.1. One parameter was changed, while keeping the other parameters at their base value. The advantage of this way of solving is that less computational effort is needed than for Monte Carlo simulations. However, the joint influence of parametric values cannot be identified this way. The results of these parametric studies were plotted as function of the normalized parameter value. The normalized parameter value was determined by dividing the value of each parameter by their upper value (e.g. Equation 6.4) for the gas flow rate).

$$\tilde{F}_{g,res,in} = \frac{F_{g,res,in}}{\max\left(F_{g,res,in}\right)} \tag{6.4}$$

6.3. Results and discussion

Ethanol concentration

The ethanol concentrations in the reservoir have been examined for the different reservoir process variables (Figure 6.1). It was expected that the ethanol concentration in the system is regulated by the hydraulic retention time. At high HRT, the produced ethanol accumulates in the system causing higher concentrations. As the HRT is regulated by the reservoir inflow rate and the reservoir volume, it is expected that these parameters have an effect while the effect of the other parameters is lower.

From this data, it was found that low reservoir inflow rates lead to higher ethanol concentrations (Figure 6.1a). In all these cases, the maximum ethanol concentration of $45\,\mathrm{g\,L^{-1}}$ was not reached. The ethanol concentration decreases with increasing reservoir flow rates. When this increases, the HRT decreases which leads to less ethanol recirculation in this system. The lower amount of recirculation does also increase its productivity as there is less inhibition in these cases. Therefore, by increasing the reservoir inflow rate, the ethanol concentration decreases in a hyperbolic way. The increased inhibitory effects decreases the slope at lower reservoir inflow rates.

It was expected that the volume of the reservoir would also have a large impact on the concentration of ethanol, but no pattern can be distinguished between the reservoir volume and the resulting ethanol concentration. This could be due to the smaller operating window compared to the possible window for the reservoir inflow rate. The gas flow rate and the module inflow rate did not seem to influence the ethanol concentration. Therefore, from this analysis can be said that the reservoir inflow rate is the most important process variable that controls the ethanol concentration.

Effect on concentration difference

The liquid flow through the module is expected to lead to certain concentration differences of the solutes between the shell inlet and outlet. As ethanol is produced in the module, the ethanol concentration is expected to be higher at the module outlet. By measuring this concentration difference in the lab, one can estimate

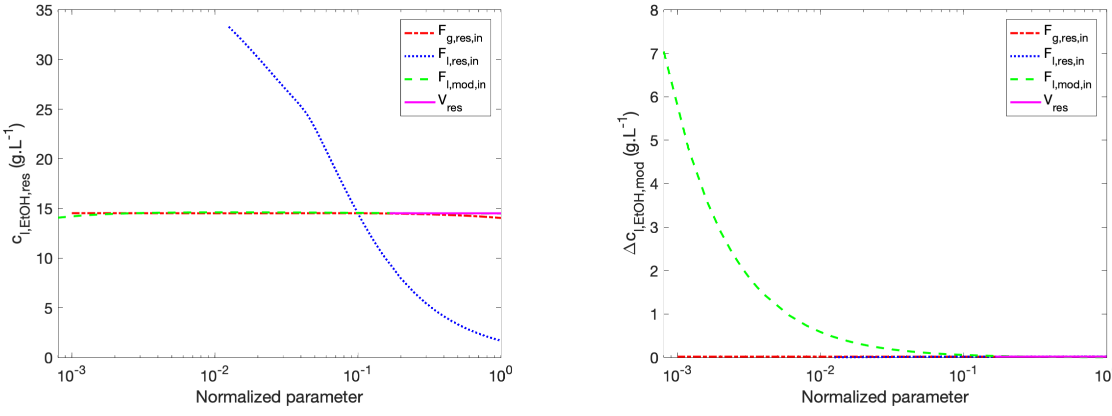

(a) (b)

Figure 6.1: (a) The concentration of liquid ethanol in the reservoir $c_{l,\mathrm{EtOH},res}$ and (b) the ethanol concentration difference over the module $\Delta c_{i,mod}$, are plotted for different values of the reservoir process parameters. The maximum and minimum values between which they were varied are given in Table 6.1. During the simulation of one range of parameters, the other reservoir parameters were kept constant according to their base values in Table 6.1.

the performance of the reactor and one is able to make mass balance calculations based on this difference. At high module flow rates it is expected that the concentration difference is very low and therefore difficult to measure. One could argue that at lower module inflow rates plug-flow behaviour is established along the axial direction in the module as along the module fibre length concentration differences can be expected. At larger inflow rates this behaviour the concentration differences are expected to become smaller, causing more STR-like behaviour.

For all reservoir parameters, the ethanol concentration difference between the module outlet and inlet was calculated (Figure 6.1b). It can be observed that the concentration difference is not influenced by the gas flow rate, the reservoir volume and reservoir inflow rate. The module inflow rate has a large influence on the concentration difference. At lower module inflow rates, the liquid residence time in the module increases. This causes that ethanol accumulates in the liquid, leading to higher concentration differences over the module.

By varying the shell liquid velocity, it could be established whether there was plug-flow or more STR-like behaviour in the shell. In Figure 6.2a, can be observed that at low module liquid flow rates, the concentrations increase (up to 50%) relative to the concentration entering the shell. This increase is due to the low flow velocity and therefore leads to a higher shell residence time, so that more ethanol can be absorbed in the liquid flow. When the module liquid flow rate reaches 20 mL min^{-1}, the concentration increase falls below 1%. This means that at flow rates lower than around 20 mL min^{-1} plug-flow behaviour can be obtained.

From these results can be determined that during operation at module inflow rates between 0.4 and 2 mL min^{-1}, the concentration difference is expected to be between 7.0 and 1.5 g L^{-1}, respectively. This concentration difference can be measured in the lab. Therefore, the reservoir could enable mass balance calculations over the module.

Effect on productivity

The module volume specific ethanol productivity of the biofilm was plotted against the normalized parameters (Figure 6.2b). From this, it was observed that the reservoir inflow rate has a high impact on the ethanol productivity in the module. As obtained before, the reservoir flow rate correlates with the hydraulic retention time, which both have a high impact on the ethanol concentration. This has a large influence on the ethanol

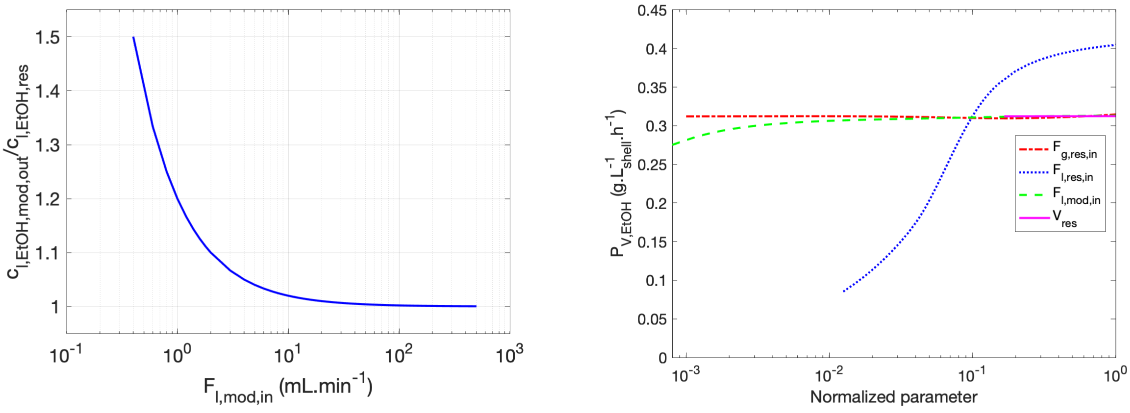

(a) (b)

Figure 6.2: (a) For different values for the module liquid flow rate, the concentration difference between the module outlet and inlet is calculated. (b) The shell volume-specific biofilm productivity of ethanol was calculated for different values of the reservoir process parameters. The maximum and minimum values between which they were varied are given in Table 6.1. During the simulation of one

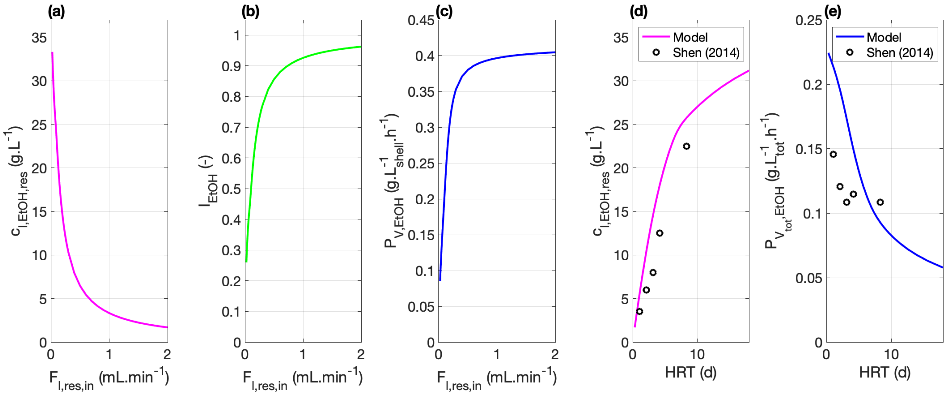

Figure 6.3: For different values of the reservoir inlet flow rates, (a) the ethanol concentration in the reservoir, (b) the ethanol inhibition constant, and (c) the shell volume specific ethanol productivity of ethanol are plotted. Next to these, the influence of the hydraulic retention time on (d) the ethanol concentration in the reservoir and (e) the total volume-specific ethanol productivity (calculated as $P_V \frac{V_{\text{shell}}}{V_{l,tot}}$) are given for the simulations and the data derived by Shen et al. (2014b) (black dots). The maximum and minimum values between which they were varied are given in Table 6.1. During the simulation of one range of parameters, the other reservoir parameters were kept constant according to their base values in Table 6.1.

productivity due to inhibitory effects. This inhibition leads then to a lower productivity (Figure 6.3a-d).

It was observed that the module inflow rate has an additional effect on the productivity. At lower inflow rates, the productivity decreased (up to around 10%). This lower module inflow rate causes an increased residence time of ethanol in the module (due to the plug flow behaviour). This is likely to cause larger concentration differences inside the module. This could lead to increased ethanol inhibition as the ethanol concentration will be higher near the end of the shell. This increased inhibition would lead to lower productivity in the biofilm. It seemed that, in the modelled HFM reactor, the volumetric ethanol productivity was not influenced by the reservoir volume (due to its small operating window) and the reservoir gas flow rate.

The influence of the dilution rate on the ethanol concentration and the productivity was derived experimentally by Shen et al. (2014b) and was compared with the simulations performed (Figures 6.2). By comparing the experimental data with the data from the model becomes clear the values obtained from the simulations are in the same order of magnitude and follow the same trends as the values of Shen et al. (2014b). This means that, despite all the assumptions made while modelling reaction, the results are in the same range as experimental data. The authors used *Clostridium carboxidivoran* P7, 300 mL min^{-1} syngas with 25% CO, a

21 cm long, microporoous membrane with 7400 fibres and returned the module syngas outflow to the reservoir. In this study, the reservoir volume (8L) was only provided, but not volume of the HFM module. All these differences cause that the productivities and the concentrations cannot fairly be compared.

It should be noted that the ethanol inhibition function is a very important assumption for determining these patterns. In Appendix F.2 is discussed that there is uncertainty on the precise mechanism of ethanol inhibition. For three different inhibition models, the reservoir inlet flow rate was varied (in the same way as in this chapter). From that analysis was found that the linear inhibition model leads to lower shell volume-specific productivities than the other models: for an inflow rate of around $0.15\,\mathrm{mL\,min^{-1}}$, this difference was significant (50% lower productivity). In order to derive model results that can be experimentally reproduced, it is highly pertinent to know which inhibition kinetics apply to the studied organism and the operational conditions.

From the analyses in Appendix F.2 was shown that the assumption that the gas outlet equals the gas inlet did not hold in cases with low gas flow rates. Reaction was also neglected in the reservoir, but this was proved to be an invalid assumption in cases with low reservoir liquid inflow rates due to accumulation of dissolved CO.

6.4. Conclusion

From incorporating the liquid recirculation reservoir was derived which parameters influence the HFM reactor. It was found that, in their possible operational windows that can be used for this HFM reactor, the reservoir gas flow rate and volume did not significantly impact the ethanol concentration, its concentration difference over the module and the ethanol productivity. In contrast, it was found that various module liquid inflow rates could lead to plug-flow behaviour in the shell liquid phase and was therefore able to influence the ethanol concentration difference between the module in- and outlets. This concentration differences also caused a small decline (around 10%) in ethanol productivity.

The reservoir inlet flow rate seemed to be a very influential parameter. This flow rate is directly coupled to the hydraulic retention time and the ethanol concentration in the module. Low flow rates increase the ethanol concentration in the HFM reactor (up to $34\,\mathrm{g\,L^{-1}}$), which causes a decrease in ethanol productivity due to inhibitory effects (up to 75%).

From this analysis can be derived that the reservoir leads to increased operational opportunities as it enabled steering the ethanol concentration and thereby the productivity in the system. Next to that, it is possible to work with low reservoir inlet flow rates and high module flow rates, without spending high amounts of fermentation medium, as the liquid phase is being recycled.

Lastly, by comparing the data with the data obtained by Shen et al. (2014b), it can be said that the calculated values of the ethanol concentration in the reservoir match with the data derived by them. The calculated productivities do not match, which is expected to be due to the use of different operational conditions.

7

Parametric analyses

After developing the reservoir model in the previous chapter, it could be determined what the influence of process parameters is on the HFM reactor. The analysed process parameters were the gas phase velocity, the gas phase pressure, the liquid pressure and the reservoir inflow rate. Although the reservoir gas inflow rate, the reservoir volume and the shell liquid flow rate are given as process parameters (in Table 2.1) they were not investigated in this chapter as since it was concluded that they had marginal influences on both the ethanol concentration and the volume-specific productivity in the studied HFM reactor (see Chapter 6). This analysis will provide insights in how these process parameters influence the syngas fermentation process in the HFM reactor. This could be used to determine an operational window to improve the reactor performance.

Next to the influence of these parameters, also a sensitivity analysis will be discussed in this chapter. A sensitivity analysis was performed for the two most important assumptions made in this model: the biofilm thickness and the biomass concentration in the biofilm. With this analysis can be derived what the impact is of the assumed parameters on the results.

7.1. Methodology

As stated in Chapter 1, the performance of the syngas fermentation process was determined to be a function of the ethanol yield, the volumetric productivity (Equation 6.2), the substrate utilization efficiency and the product concentration ($c_{l,EtOH,res}$). As the ethanol yield is a function of the metabolism, which was assumed to be constant (only CO consumption and ethanol formation according to the derived stoichiometry in Appendix F), this indicator was not taken into account in the further studies. The substrate utilization efficiency could be calculated in multiple ways. The first way is the amount of CO that is transferred from the gas into the membrane, which is defined as the gas phase mass transfer yield (Equation 7.1). It could also be defined as the amount of CO that is consumed relative to the amount that is transferred to the micro-organism (Equation 7.2). Lastly, the overall CO yield was derived as function of the amount of CO that is consumed by the micro-organism relative to the amount that enters the lumen (Equation 7.3).

$$Y^{MT}_{g,CO} = 1 - \frac{N_{g,CO,out}}{N_{g,CO,in}} = 1 - \frac{\left.\int_0^{A_{c,g}} \boldsymbol{u_g} c_{g,CO} \mathrm{d}A_{c,g}\right|_{z=L_f}}{\left.\int_0^{A_{c,g}} \boldsymbol{u_g} c_{g,CO} \mathrm{d}A_{c,g}\right|_{z=0}} \tag{7.1}$$

Table 7.1: The operating window and values of the different process parameters which values were varied. The base value of each parameter was kept constant during variations of other parameters.

Model	Parameter	Symbol	Unit	Base value	Lower value	Upper value
M_param_Fgin	Lumen gas flow rate	$F_{g,in}$	$\mathrm{mL\,min^{-1}}$	20	4	200
M_param_Pgas	Lumen gas overpressure	Δp_g	atm	1.5	1	1.5
M_param_Pliq	Liquid overpressure	Δp_l	atm	1	1	2
M_res_Flresin[a]	Reservoir liquid inflow rate	$F_{l,res,in}$	$\mathrm{mL\,min^{-1}}$	0.11[b]	0.025	2

a) For $F_{l,res,in}$ the same model was used as in Chapter 6. There, $F_{l,mod,in}$ and $F_{g,res,in}$ were set to be 150 and 1 $\mathrm{mL\,min^{-1}}$, respectively.
b) When varying Δp_l, $F_{l,res,in}$ was set to be 0.12 $\mathrm{mL\,min^{-1}}$.

$$Y_x = \frac{\int_0^{V_b} q_{CO} c_{b,x} \mathrm{d}V_b}{\left. \int_0^{A_{s,gm}^{\mathrm{int}}} J_{CO,gm}^{\mathrm{int}} \mathrm{d}A_{s,gm}^{\mathrm{int}} \right|_{r=r_{gm}^{\mathrm{int}}}} \tag{7.2}$$

$$Y_{CO}^{ov} = \frac{\int_0^{V_b} q_{CO} c_{b,x} \mathrm{d}V_b}{\left. \int_0^{A_{c,g}} \boldsymbol{u_g} c_{g,CO} \mathrm{d}A_{c,g} \right|_{z=0}} \tag{7.3}$$

Initially, it was aimed to derive optimum values for the performance indicators by varying the process parameters according in their windows using Monte-Carlo simulations (the same approach as in Chapter 6). From these simulations, several patterns between the process parameters and the process performance indicators could be derived. However, this optimization method did not work for several random combinations of parameters, which is expected to be due to the non-linearity in the model.

Instead, the parameters were individually varied in the window of operation as provided in Table 7.1. The reservoir parameters were kept constant: $F_{g,res,in} = 60\,\mathrm{mL\,min^{-1}}$, $F_{l,mod,in} = 100\,\mathrm{mL\,min^{-1}}$, $V_{res} = 0.5\,\mathrm{L}$ and $F_{l,res,in} = 0.11\,\mathrm{mL\,min^{-1}}$, so that the hydraulic retention time in the HFM reactor equals 5.7 day. The biofilm thickness d_b was assumed to be 190 µm. The same model was used as in Chapter 6, which was described in detail in Chapter 2.

A sensitivity analysis performed for the assumed biofilm thickness and biomass concentration (M_sens). The influence of these parameters on the ethanol concentration, shell volume-specific productivity and the overall CO yield was calculated. The biofilm thickness d_b was varied between 20 and 250 µm, during these simulations the biomass concentration in the biofilm $c_{b,x}$ was varied between 10 and 60 $\mathrm{kg\,m^{-3}}$. This way the cumulative effects of both assumptions could be determined, as a 2D plot can be derived from simulating these values. The process parameters were kept constant at their base value (Table 7.1).

7.2. Trade-off analysis

For all analysed process parameters, their effects on the performance indicators (the ethanol concentration, the overall CO yield and the volumetric ethanol productivity) are depicted in Figure 7.1. In this figure, the influence of these parameters on the trade-offs shown can be analysed. From these results can be stated that the reservoir inflow rate and the lumen gas flow rate are the most important parameters governing the trade-offs in the modelled HFM reactor. In the operating window used, the liquid pressure and the CO pressure in the gas phase have only a small influence on performance indicators. Their influence is smaller as the ranges wherein the performance indicators vary are much smaller than the ranges obtained by varying the gas flow rate and the reservoir liquid inflow rate.

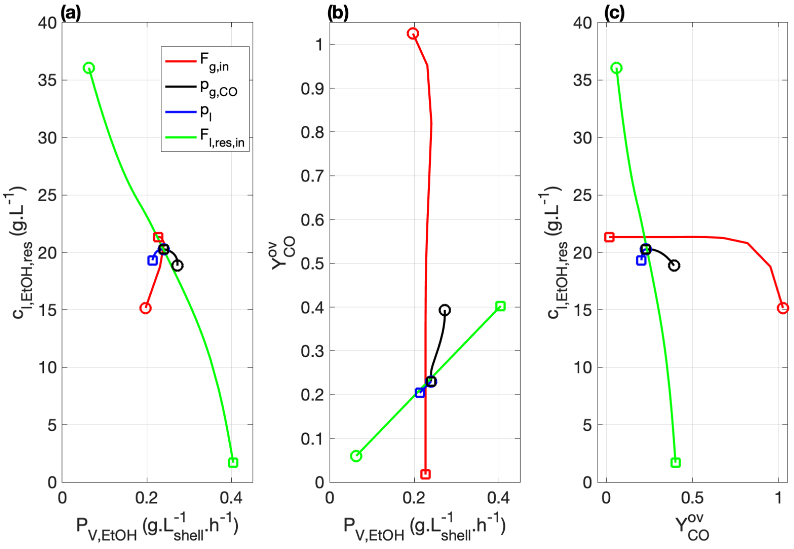

Figure 7.1: Trade-offs are depicted that can be achieved within the operating ranges of the different process parameters. The trade-off between (a) the volumetric ethanol productivity and the ethanol concentration, (b) productivity and the overall CO yield, and in (c) the overall CO yield and the ethanol concentration. During these simulations the process parameters were individually varied in their operating ranges. The circle depict the lower boundary, while the squares depict the upper boundary. During the simulation of one parameter the other process parameters were kept constant according to their base values in Table 7.1.

For the reservoir liquid inflow rate, there is a clear trade-off between the concentration of ethanol and the productivity. Higher productivities lead to lower concentrations, while higher concentrations cause lower productivity. Also, the reservoir inflow rate leads to changes of the productivity and the concentration in a very wide range, compared to the other parameters. Varying the lumen gas flow rate could create a change in concentration of around 5 $\mathrm{g\,L^{-1}}$, while the influence of the gas pressure and the liquid pressure is negligible in these cases.

Furthermore, the influence of the gas flow rate on the volumetric productivity is marginal compared to the influence of the reservoir liquid inflow rate on the volumetric productivity. However, the gas flow rate can be used to manipulate the overall CO conversion yield in the HFM reactor. By varying the lumen gas flow rate, one can steer the overall yield from 100% to almost 0%. Besides, there is a certain optimum in productivity for the gas flow rate (as will be demonstrated in Figure 7.2a). From Figure 7.1b can be observed that for this gas flow there is an optimum value between productivity and yield: An overall yield of 90% can be achieved, without significantly harming the productivity.

7.3. Process parameter analysis

As the reservoir inflow rate and the lumen gas flow rate are the process parameters that influence the performance of the HFM module the most (Figure 7.1), they will be discussed in this section. The influence of the CO partial pressure and the liquid pressure is discussed in Appendix I.

Lumen gas flow rate

At low gas flow rates, the lumen gas phase is expected to behave like a closed-end system (Chapter 4) due to the limiting amount of CO that can be transferred towards the membrane. At higher gas flow rates, the CO amount is expected not to be limiting anymore and will therefore not increase the mass transfer rate. As was also observed in Figure 4.4, high flow rates could lead to an increased mass transfer rate at the expense of the mass transfer yield. However, that analysis was performed with a syngas mixture and without biofilm, so that it does not represent the effect that would be in cases with more CO.

In Figure 7.2a, it can be observed that the volumetric productivity only changes by flow rates up to 12.5 mL min^{-1}. Gas flow rates between 4 and 6 mL min^{-1} cause substrate limitation in the biofilm, while higher mass transfer rates can be achieved at increasing gas flow rates. However, an optimum productivity is reached at 6 mL min^{-1}. This increase in productivity also causes an increase in ethanol concentrations (Figure 7.2b). Due to the liquid recirculation, a small increase in the productivity (0.2 to 0.24 g L^{-1} h^{-1}) leads to a high increase in ethanol concentration (from 15 to 21.3 g L^{-1}). However, between 6 and 12.5 mL min^{-1} the productivity decreases slightly, until a constant value is reached. This is expected to be due to CO and ethanol inhibition. The increased ethanol concentration will lead to inhibition and therefore prevents the productivity of the micro-organism to increase. Due to the increased mass transfer rate, and the inhibitory effects of both compounds, less CO can be consumed by the organism, decreasing the productivity even more. At flow rates higher than 12.5 mL min^{-1}, the productivity remains constant. This implies that the increase in gas flow rate (or gas supply) does not lead to more mass transfer as the reaction becomes the limiting factor for mass transfer.

At very low gas flow rates, the yields are high and even reach 100% (Figure 7.2c). As the gas mass transfer yield reaches 100%, closed-end behaviour is reached. However in these cases, the productivity is lower. By increasing the gas flow rate, the mass transfer yield decreases, but the productivity increases slightly. At the optimum productivity (6 mL min^{-1}), the overall yield has decreased to 80%. The consumption yield is a function of the biomass productivity and therefore also decreases at flow rates where the ethanol concentration becomes inhibitory. The overall yield was always lower than the gas phase mass transfer yield, but when the consumption yield decreases, the overall yield decreases even more.

A possible problem derived from this are the trade-offs between the volumetric ethanol productivity, ethanol concentration and overall yield. In the range where its concentration is high (at increased gas flow rates (> 8 mL min^{-1}), the overall yield is decreased by 30%. In order not to waste too much syngas, the gas flow rate should be adjusted very carefully in this narrow operational range. Another problem with this system is ethanol inhibition: Already at very low gas flow rates, the ethanol becomes inhibitory and causes a decline in productivity. In order to increase the productivity, the ethanol concentration should become lower, which could be done by for example *in situ* product removal technologies.

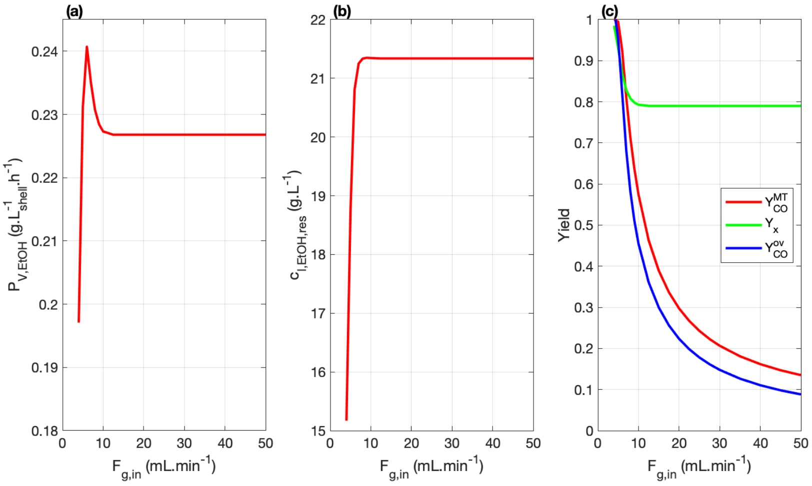

Figure 7.2: For different values of the lumen gas flow rate $F_{g,in}$ inlet flow rates, (a) the shell volume-specific ethanol productivity, (b) the ethanol concentration in the reservoir and (c) the different yields are calculated (M_param_Fgin). The lumen gas flow rate was varied between 4 and 200 mL min^{-1}, but the results above 50 mL min^{-1} are not shown as the same trends continue. During these simulations other process parameters were kept constant according to their base values in Table 7.1.

Reservoir inflow rate

Also for the reservoir liquid inflow rate between 0.025 and 2 mL min^{-1}, the process indicators were calculated (Figure 7.3). This inflow rate has an inverse proportional correlation to the HRT, which influences accumulation of solutes (see Chapter 6). From the analysis can be observed that low inflow rates cause low productivities, but high ethanol titers. At high reservoir flow rates, the concentration of ethanol approaches zero, while at lower flow rates, the concentrations increase to around 35 g L^{-1}. This large change in the achievable ethanol concentration range also implies that this parameter can be used to steer the effect of the ethanol inhibition on the volume-specific ethanol productivity. Experimentally, one could easily change the reservoir inflow rate and thereby adjust the amount of ethanol in the system and change the biomass productivity (if steady-states can be reached quickly).

In terms of yield, the effect of the reservoir liquid inflow rate is similar. Higher inflow rates generate higher overall, consumption and mass transfer yields. The diminishing amount of ethanol inhibition at high flow rates cause that more CO can be consumed. This in turn leads to increasing overall and consumption yields. The mass transfer yield is increased as well, as the higher reaction rate leads to a higher driving force of CO across the membrane and thereby increases the CO transfer rate relative to the amount of CO entering the lumen.

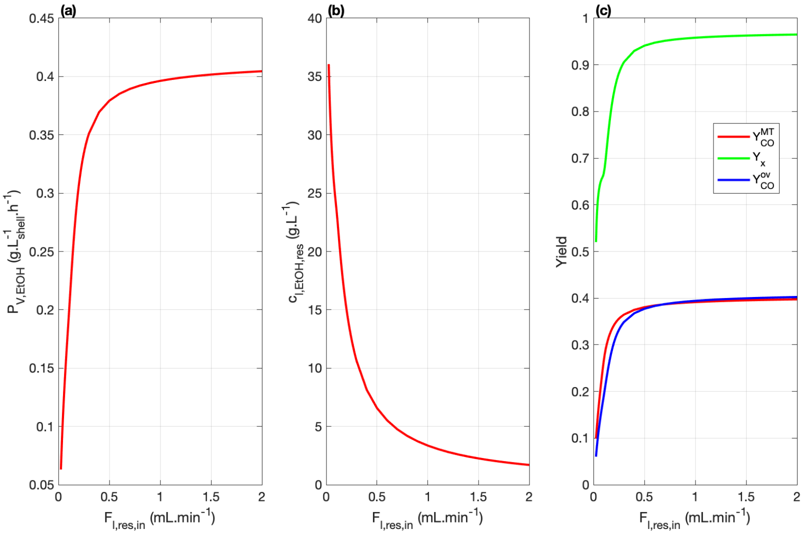

Figure 7.3: For different values of the reservoir liquid inflow rate, (a) the shell volume-specific ethanol productivity, (b) the ethanol concentration in the reservoir and (c) the different yields are calculated (M_param_Flresin) . The liquid inflow rate was varied between 0.025 and 2 mL min^{-1}. During these simulations other process parameters were kept constant according to their base values in Table 7.1.

7.4. Sensitivity analysis

During modelling the biomass concentration in the biofilm and the biofilm thickness were assumed. As there have not been any measurements for those parameters for syngas fermentation by *Clostridium* spp. in HFM reactors, values for these parameters have been assumed in the developed models. The influence of these parameters was determined with a sensitivity analysis. Both the biofilm thickness and the biomass concentration were varied between a certain range which was thought to be possible in practice. The biomass concentration was varied between 10 and 60 g L^{-1}, while the biofilm thickness was changed between 20 and 240 μm. As these two parameters have a conjoint effect on the system (both cause an increase of total biomass), a 2D

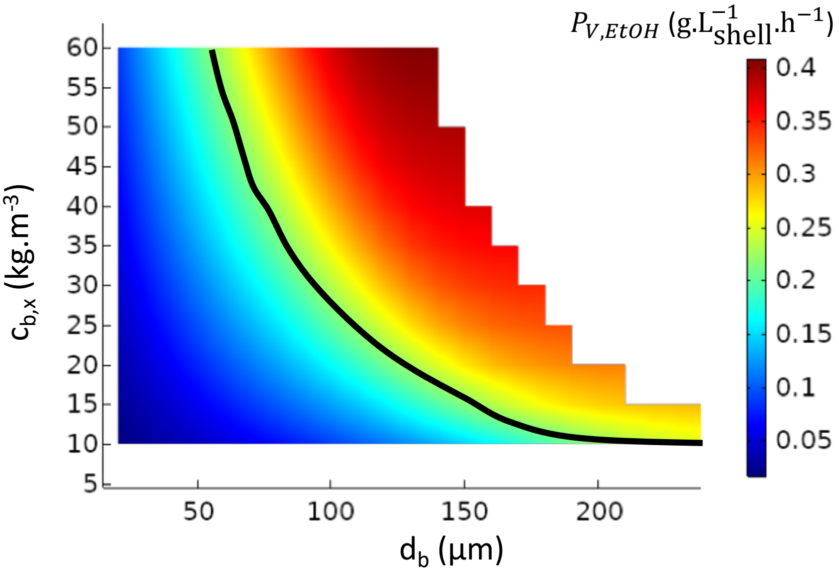

Figure 7.4: Sensitivity analysis for the biofilm thickness d_b and its biomass concentration $c_{b,x}$. These parameters were varied between 20 and 240 µm, and 10 and 60 $\mathrm{g\,L^{-1}}$, respectively (M_sens). The shell volume specific ethanol productivity of the biofilm was calculated for each simulation. The black line depict the range of biomass concentrations and biofilm thicknesses at which biofilm formation leads to higher volumetric productivity than suspended biomass, which is the case for values above the line. During this simulations, the process parameters were kept constant at their base value (Table 7.1).

analysis was performed: for all varying values of the biofilm thickness, the biomass concentration was varied as well.

The influence of the biofilm thickness and its biomass concentration on the shell volume-specific ethanol productivity (Figure 7.4), the overall CO yield (Figure I.6) and the ethanol titer (Figure I.7) were calculated. As the results of the concentration and yield followed the same patterns as the productivity, they are depicted in Appendix I. From this sensitivity analysis became clear that in cases with large amounts of biomass in the module (thick biofilms with high concentrations), the system did not solve correctly. This is expected to be due to the low CO concentrations which can be achieved near the biofilm-liquid boundary, which causes that there cannot be reaction at these points. This was also observed in the detachment models (Appendix G) , where at thick biofilms (with constant $c_{b,x} = 15\,\mathrm{g\,L^{-1}}$) the reaction became limiting.

From the results obtained it can be seen that increasing both the biofilm thickness and the biomass concentration leads to increased productivities, yields and ethanol titers. The influence of these parameters can be significant when the amount of biomass in the system is low: doubling the biomass concentration can lead to an almost twice as large ethanol productivity, overall CO yield and ethanol titer, as expected. This can be explained by the reaction rate, as this increases proportional with the biomass concentration. When there is more biomass, a doubling of biomass concentration causes a lower increase due to increased ethanol inhibition.

The influence of the biofilm thickness is even more significant: doubling the biofilm thickness (at low biomass concentrations and therefore low ethanol concentrations) causes a more than twice fold increase in productivity, yield and titer. This is due to cylindrical nature of the biofilm, doubling the biofilm thickness causes a more than proportional increase in biofilm volume and therefore in the amount of biomass present.

From this analysis, it can be said that it is important to derive some estimates for the biofilm thickness and its concentration. As in Figure 5.3 was shown, in some cases it is, beneficial not to have biofilms, in terms of volumetric productivity. The black line in Figure 7.4 compares the amount of biomass that would lead to higher productivities in biofilms than in suspended cases. This line indicates that at moderate values of both parameters biofilm formation is beneficial for the volumetric productivity.

There are no clear values obtained in literature for *Clostridium* biofilms. Wang et al. (2017b) performed syngas fermentation with microporous HFM with a mixed culture (66% *Thermoanaerobacterium*) and obtained a biofilm thickness of around 100 μm. For aerobic waste water treatment using membrane aerated biofilm reactors (with higher possible growth rates), biofilm thicknesses between 50 and 200 μm were observed (Casey et al., 1999).

7.5. Conclusion

From the analyses performed in this chapter was derived that the reservoir liquid inflow rate and the lumen gas flow rate are the most influential parameters governing the performance of the HFM reactor. The lumen gas flow rate could be used to increase the overall yield: At very low gas flow rates, overall CO yields of around 90% were observed without significantly hampering the ethanol productivity. The reservoir inflow rate determines the concentration of ethanol in the HFM reactor. Higher inflow rates lead to lower concentrations and increase the ethanol productivity. For designing this process, a trade-off needs to be made between desired productivity and ethanol concentration.

Changing the liquid pressure does not lead to large differences in the HFM module. For the gas pressure, a counter-intuitive result was obtained: higher pressures induce lower productivities, which was explained to be due to a combined effect of both ethanol and CO inhibition.

Lastly, a sensitivity analysis was performed for the biofilm thickness and its biomass concentration. Doubling one of the values of these parameters could promote a twofold increase in productivity, concentrations and overall CO yield. These parameters are therefore important to derive to make sure that the model can make adequate predictions.

8

Model validation

As models could only provide an approximation of reality, it is important to verify whether the model predicts the reality accurately. Therefore, the results from the model should correspond to experimentally obtained data in the lab. For some model parameters, the values have been assumed. Once these values are experimentally obtained, the model could be amended.

In this chapter, experiments are proposed for validation of the model. Three classes of experiments are discussed: First, a set of experiments should be performed to verify whether the assumptions behind the model could be made. Subsequently, a set of experiments is discussed for determining whether the results derived from the model correspond to experimental data. Lastly, experiments are proposed to determine the values of some unknown parameters. In Table 8.1 an overview of the proposed experiments is provided.

Table 8.1: Experiments proposed for validation of the developed model. The proposed experiments are more extensively described in the section depicted in the table.

Determinant	**Experimental procedure**	**Analysis**
Model assumptions		
Liquid and gas flow distribution	Inject gas and liquid flows with an inert tracer pulse	Investigate the residence time distribution profile of tracer
Bubble formation in shell	Operate with lumen gas overpressure	Observe bubble formation in liquid phase
Reservoir outflow rate	Perform experiments with different reservoir inflow rates	Investigate the difference between in- and outflow rates
Reservoir volumetric mass transfer coefficient	Purge with O_2 and measure c_{l,O_2} with DO probe	Determine the O_2 uptake over time
Model results		
Axial concentration profiles in gas phase	Rapid sampling after syngas injection and with counter-current flow	Determine time of outflow for each compound
Decreased lumen gas flow velocity	Measure gas flow rate at outlet	Compare with inlet
Trade-off between mass transfer rate and yield	Measure mass transfer rates for different gas flow rates	Compare with gas concentrations in the lumen in- and outflow
Determine volumetric mass transfer coefficient of module	Measure mass transfer rates for different *Re*	Equation 8.3

Determine main resistance	Determine constants in Equation 8.4	Calculate $k_{l,i}$ and compare with $k_{m,i}$
Inhibition model (qualitative)	Varying lumen gas pressure	Compare observed trends with different inhibition models
Verify influence of $F_{l,res,in}$	Vary liquid flow rate and measure ethanol concentration and productivity	Equation 8.5
Determine influence of evaporation	Measure water and ethanol concentrations in lumen off-gas	Verify whether evaporation can be neglected
Model variables		
Stoichiometry	Measure production and consumption of the different compounds	Calculate the stoichiometric coefficients
CO uptake kinetics	Vary CO partial pressure	Measure CO uptake rate and fit with kinetic equation
Ethanol inhibition kinetics	Vary ethanol concentration	Measure CO uptake rate and fit with kinetic equation
Biofilm thickness	1) Measure Δp_l with and without biofilm	Calculate the hydraulic diameter with Darcy-Weisbach equation
	2) Single fibre study and scanning electron microscopy	Measure biofilm thickness
	3) Optical coherence tomography in module	Measure biofilm thickness
Biomass concentration	1) Sonification to suspend the biomass from the membrane	Measure total organic carbon
	2) Calculate from dilution rate the biomass amount in the module	Equation 8.7
Biofilm diffusivity factor	Single fibre study with micro-sensor and N_2 permeation	Measure N_2 concentration profile and mass transfer rate

Model assumptions

The most important characteristic behind the model is the model geometry: In order to describe the HFM reactor, only one fibre was modelled (Chapter 2). This geometry assumed that there is no flow maldistribution in the system (i.e. the liquid flow velocity is equal near all fibres) and that the gas flow is proportionally distributed (i.e. the same amount of gas flows through all fibres). These assumptions can be verified using studies with inert tracer compounds.

With a short insertion pulse of a tracer compound in the inlets and measuring the tracer at the outlet, one can determine the residence time distribution of the tracer in both the gas and liquids phase. The shape of the distribution curve provides thereby information on the flow pattern. In case the flow is uniform among all fibres (plug-flow), the distribution will have a narrow peak, while in cases with flow non-uniformity, the peak is expected to be wider. These experiments are similar to the ones Kavousi et al. (2016) performed for different values of the fibre spacing.

For the shell side, these experiments can be performed with and without biofilm. From this can be determined whether the biofilm influences the flow pattern. This can provide insights whether clogging and preferred flow could occur.

Another important assumption made while modelling is based on Equation 2.11. This boundary condition implies that there is no bubble formation in the HFM module in cases where the dissolved gas concentration reaches supersaturation. This assumption could be justified by permeating with pure CO (or other poorly soluble compounds), with an overpressure in the gas phase. This should be done in biotic and abiotic modules. In the cases bubbles are formed in the module, this assumption does not hold. Bubble formation is expected to increase the volumetric mass transfer coefficient due to the increased amount of surface area for mass transfer, to decrease the overall CO yield due to possible release in the reservoir off-gas, and it could also lead to abrasion of the biofilm.

Next to this, the reservoir has been modelled by assuming that the gas outflow rate equals the gas inflow rate ($F_{g,res,out} = F_{g,res,in}$). This assumption need to be justified as it could lead to erroneous prediction of the reservoir off-gas composition. This analysis can be performed by measuring both the in and outflow rates and comparing them with each other (as in Figure H.2a). Lastly, the volumetric mass transfer coefficient of the reservoir was assumed to be $30\,\mathrm{h}^{-1}$. This value can be obtained by aerating the reactor with oxygen and measure the oxygen uptake over time with a DO probe.

Model results

From the models developed in Chapters 3 and 4 was derived that the mass transfer rate highly depends on the permeability of the different compounds. This also causes that the flux is location-specific, which resulted in large concentration differences for CO_2 along the axial direction. Assuming that it is impossible to measure axial and radial gradients directly in the HFM module, different strategies need to be determined to validate these effects.

First, the mass transfer rate can be calculated, by measuring the concentration differences inside the liquid phase. By using a low, known, liquid flow rate ($F_{l,mod,in}$), a concentration difference along the module length is expected to be present (as was demonstrated in Figure **??**). By measuring the concentrations of dissolved gasses in the reservoir and at the module outlet, the mass transfer rate can be determined (Equation 8.1). By measuring concentrations with a DO probe, Orgill et al. (2019) determined the O_2 gas to liquid mass transfer rate in a dense PDMS HFM module. Orgill et al. (2019) also used gas chromatography to determine the mass transfer rate from the gas to the liquid (using Equation 8.2). Other ways to measure the values of the dissolved gasses are using vacuum separation and GC/MS (Abrahamsom, 2019). Based on these two equations, the known gas inlet pressure and assuming the concentration of gasses in the liquid inlet to be 0, the module outlet concentration was calculated.

$$T_i^{MT} = F_{l,mod,in} \times \left(c_{l,i,mod,out} - c_{l,i,res}\right) \tag{8.1}$$

$$T_i^{MT} = F_{g,in} \frac{K_i^{lg} p_{g,i,in}}{RT} - F_{g,out} \frac{K_i^{lg} p_{g,i,out}}{RT} \tag{8.2}$$

Using these methods, it could be determined whether there will be concentration gradients along the axial direction. By using rapid sampling, low gas and liquid flow rates, a known syngas mixture pulse injection, and counter-current flow. This method is based on the fact that most of the CO_2 is expected to permeate near the lumen inlet, while the other compounds permeate near the end of the lumen as the fluxes of these compounds will be higher near the end. Due to the counter-current flows, most of the permeated CO_2 is expected to leave the module earlier than the other compounds. By measuring the liquid concentrations over time at the outlet of an abiotic module, one could make distribution plots from which could be clear which compounds appeared over time. This is then expected to be correlated to the axial concentration profiles.

For these measurements, also the gas velocity needs to be measured at the outlet (inlet is supposed to be known). With this measurement, one could determine that the gas flow velocity decreases, which was one of the main results of the gas phase model. This way, it could experimentally be stated that one should not assume constant axial gas velocities and concentrations while modelling HFM modules.

Next to this, it could be interesting to experimentally determine the trade-offs between mass transfer rate and the mass transfer yield, for different values of the lumen gas flow rate (as in Figure 4.4). This way, one could determine whether there obtained data match experimentally and decide which gas flow rate to use for experiments.

Using the calculated mas transfer rates, one could calculate the overall volumetric mass transfer coefficient of the HFM module with Equation 8.3 (Orgill et al., 2019). The data obtained by modelling (Figure 5.1) could be checked with experimental data. The most interesting analysis would be varying $F_{l,mod,in}$ (or Re_l). A higher value would lead to a lower liquid mass transfer resistance and thus a higher $k_{L,i}^{ov}a$. This way it could be checked whether the predicted results from the model correspond to experimental data. Next to that, one could determine the $k_{l,i}$ by fitting the γ and δ coefficients in the correlation for the Sherwood number with the experimentally determined $k_{L,i}^{ov}a$ values for different Reynolds numbers (Kavousi et al., 2016; Orgill et al., 2019), and Equation 5.3. With this data, it could be determined for which Re_l the membrane becomes the dominating factor for mass transfer, as was simulated in Figure 5.2.

$$k_{L,i}^{ov}a = \frac{T_i^{MT}}{\Delta c_{i,ln} V_{\text{shell}}} \quad \text{with} \quad \Delta c_{i,ln} = \frac{\left(\frac{K_i^{lg} p_{g,i,in}}{RT} - c_{l,i,mod,out}\right) - \left(\frac{K_i^{lg} p_{g,i,out}}{RT} - c_{l,i,mod,in}\right)}{\ln\left(\frac{\left(\frac{K_i^{lg} p_{g,i,in}}{RT} - c_{l,i,mod,out}\right)}{\frac{K_i^{lg} p_{g,i,out}}{RT} - c_{l,i,mod,in}}\right)} \tag{8.3}$$

$$Sh_l = \frac{k_{l,i} d_{\text{spacing}}}{D_{l,i}} = \gamma Re^{\delta} Sc^{1/3} \tag{8.4}$$

However, it is expected that during operation in HFM modules, no radial gradients can be measured. This makes it impossible to determine the concentration gradients in the biofilm. Next to that, due to the uncertainty in the biofilm thickness, the biomass concentration and the metabolism of *Clostridium*, it is expected to be impossible to validate any of the conversion related results quantitatively, until more information on these parameters is retrieved and the model is run based on these new values.

However, it would still be possible to justify the predicted effects from the model by observing trends due to changes in process parameters. First of all, it could be determined whether the linear ethanol inhibition model is possible here. Figure I.1 demonstrated that increased pressures would cause lower productivities due to increased inhibition of ethanol and CO, while it was also demonstrated that another ethanol inhibition model would increase the ethanol productivity at higher pressures (Figure I.3). By varying the gas pressure and measuring the ethanol productivity for the different gas pressures in the module, one could determine qualitatively which of these inhibition models have a better fit with the experimentally obtained data.

$$P_{V,EtOH} = \frac{F_{l,mod,in}}{V_{\text{shell}}} \times \left(c_{l,EtOH,mod,out} - c_{l,EtOH,res}\right) \tag{8.5}$$

The productivity in the module can be determined by measuring the concentrations in the module inflow and outflow (Equation 8.5) at steady-state. This way, the influence of the reservoir inflow rate could be verified. However, as high HRT are necessary to obtain high ethanol concentrations (Figure 6.3), these experiments could be very long-lasting experiments, as new steady-states need to be obtained.

Lastly, evaporation from the shell to the lumen was taken into account for water as it was expected that this was not significant for ethanol (Appendix E). One should determine by measuring the lumen gas outlet whether these assumptions are correct and whether ethanol evaporation could be an issue at high concentrations of ethanol in the reservoir.

Model variables

Different parameters need to be retrieved with regard to the micro-organism and the biofilm as much information is not known. Therefore in this section, it will be discussed how several of these parameters could be derived: the stoichiometry of the micro-organism, the kinetics, the biofilm thickness, the biomass concentration in the biofilm and the biofilm diffusivity factor.

The stoichiometry of the micro-organism can be derived by measuring the production and consumption rates of the different compounds. This way, the amount consumed and produced can be derived, which should relate in a stoichiometry of the metabolism (e.g. Equation 8.6 for biomass and CO). However, it must be assumed that the stoichiometry is independent of the substrate or product composition, which could be an unrealistic assumption in biofilms as it is known that extracellular acetate and hydrogen concentrations induce metabolism shifts (Jack et al., 2019; Xu et al., 2020).

The correctness of the CO-uptake kinetics as derived by Mohammadi et al. (2014) was questioned before (Chapter 5). In cases a steady-state is reached, one could vary the CO partial pressure (either by decreasing the gas overpressure or by diluting with N_2) and determine that effect on the consumption rate of CO. As the proposed kinetic function for CO uptake depends on an inhibition and saturation constant, one could determine these constants by fitting the kinetic function with the CO consumption rates. For this one needs to assume that the CO concentration is constant everywhere in the biofilm. This will lead to a lumped term for the maximum uptake rate and the biomass concentration ($q_{CO}^{max} c_{b,x}$) as both are unknown. In these cases, the ethanol concentration needs to remain constant so that inhibition does not influence the results.

The ethanol inhibition kinetics could be measured by running the HFM reactor with different concentrations of ethanol and determining the CO consumption rate. The amount of CO provided to the organism needs to remain constant in these cases.

$$Y_{x/CO} = \frac{R_x}{R_{CO}} = \frac{F_{l,mod,in} \times \left(c_{l,x,mod,out} - c_{l,x,res}\right)}{F_{g,in} \frac{p_{g,CO,in}}{RT} - F_{g,out} \frac{p_{g,CO,out}}{RT} + F_{l,mod,in} \times \left(c_{l,CO,mod,out} - c_{l,CO,res}\right)} \tag{8.6}$$

$$R_x = \mu c_{b,x} V_b = \frac{1}{HRT} c_{b,x} V_b = R_{CO} Y_{x/CO} \tag{8.7}$$

Using the Darcy-Weisbach pressure drop equation (Brown, 2002), one could possibly determine the biofilm thickness. As the pressure drop is inversely proportional to the fibre spacing, a smaller fibre spacing (due to biofilm) will increase the pressure drop. In these cases, it needs to be assumed that the friction factor does not significantly change due to increased roughness of the biofilm. This assumption can be made when the flow is laminar (Janssen and Warmoeskerken, 2006).

One could also determine the biofilm thickness using scanning electron microscopy, as was done by Zhang et al. (2013) and Wang et al. (2017b). In this case, the biofilm first needs to be extracted out of the module. Experiments could also be performed with only one fibre outside the module, and to use the biofilm grown on that fibre for characterization studies. Another technique is optical coherence tomography which can be performed to derive *is-situ* information on the biofilm (Dreszer et al., 2014), eliminating the need for single fibre studies.

Next to this, the biomass concentration in the biofilm needs to be derived. This could possibly be done using the procedure derived by Tijhuis et al. (1994). They used sonification to suspend the biomass from the particles and used total organic carbon analyses to determine the amount of biomass.

While operating a reservoir and when a steady-state is reached, the growth rate should equal the dilution rate of the reservoir. With the mass transfer rates the stoichiometry could be derived (as explained above). As the reaction rates are a function of the biomass concentration, one could calculate the biomass concentration in the biofilm, when the biofilm thickness is known (Equation 8.7). In cases without known biofilm thickness, only a lumped parameter ($c_{b,x} V_b$) can be retrieved, which should represent the amount of biomass in the HFM module (similar to Figure 5.3).

The biofilm diffusivity factor could be measured in the single fibre experiment, outside the module. Using micro-sensors, one can measure the concentration profiles inside the biofilm. For inert compounds, like N_2, this concentration profile depends on the biofilm diffusion coefficient. As this is proportional to its liquid counterpart, the diffusivity factor can be determined.

As a general note, scientific philosopher Popper (1963) proposed that science could only be falsified: One can only derive that a theory, model or statement, is not true, since one is never sure that there is a case in which the derived theory, model or statement does not hold. In line with this, one can never be sure that the model is correct.

Next to this, Box (1976) proposed the famous statement "all models are wrong". This indicates that one should not take the results derived by the model for granted. However, the results derived by the model could still be useful predictors for reality. Therefore, one should ask whether the model is useful, instead of whether the model is correct.

9

Future perspectives

By modelling the HFM reactor, new insights were gained on the performance of this system and in the parameters that influence the HFM reactor the most. Development of this model was not straightforward. The *reacting flow* interface in COMSOL was not known before, as well as the necessary coupling between the membrane and gas phase. Scrutinizing the models with mass balances was necessary to ensure internal correctness. Now these methods are known, gas phase models can be developed more accurately.

Although results derived from modelling should not be taken for granted, the model provided insights and trends which were not known before. Such an understanding is valuable as it could guide design of more efficient HFM reactor modules. With this information, an operational window was derived that could be used for design of experiments. Besides, with the model, one could determine the theoretical influence of several parameters in a faster and more resource-efficient way than by performing experiments.

However, there are some limitations behind the developed model. First of all, it is a complex model due to the amount of phases, components and balances modelled. This complexity was necessary to ensure that all phases were modelled in the most accurate way, as it was shown that several simplifying assumptions did not hold. Next to this, the liquid recirculation reservoir highly increased the non-linearity in the system, making it difficult to solve without providing initial values. Furthermore, in cases where mass transfer was limiting CO conversion in the biofilm (at high biomass concentrations), the model did not converge. After incorporating the reservoir, time-dependent studies could not be performed, hampering the applicability to study the behaviour of the HFM reactor over time. Next to this, the assumptions for the reservoir gas outlet and neglecting conversion in the reservoir did not hold in case with low reservoir gas and liquid inflow rates, respectively.

From the obtained results cannot be said whether the HFM reactor is a suitable configuration for industrial scale syngas fermentation. Industrially achievable productivities are more than one order of magnitude higher (up to $10\,\mathrm{g\,L^{-1}\,h^{-1}}$ (Molitor et al., 2016)) than the ones obtained during modelling (around $0.4\,\mathrm{g\,L^{-1}\,h^{-1}}$). These difference are expected to be due to optimized reactor configurations and strain engineering. As kinetics of industrial used strains are not known, no conclusions can be drawn with regard to the industrial performance of this HFM reactor. Besides, no other reactors configurations have been modelled for syngas fermentation with the same kinetic and inhibition model, so that comparison with other reactor configurations models (like bubble columns) is not straightforward.

The next step for advancing this line of research is derivation and validation of the stoichiometry CO consumption and ethanol formation, as well as determining the kinetics of CO uptake and ethanol inhibition of *Clostridium* spp. New insights in the metabolism could lead to enhanced predictions of ethanol concentrations, ethanol productivity and CO conversion yields. When more information of biofilm characteristics (thickness, biomass concentration and diffusion factor) is known, this model could experimentally be tested in the lab. With the current knowledge, only the abiotic models can be validated in the lab.

Experimental research should also focus on development of strains that do not experience inhibition by ethanol. Using evolutionary engineering techniques, the micro-organism could be adjusted to higher ethanol concentrations. Further options for future studies are implementation of *in-situ* product removal technologies. Among those, one could think about ethanol extraction using an organic phase in the reservoir. The reservoir also enables the possibility to implement separation technology in the liquid flow circuit. One could couple the HFM module with a distillation column or another membrane module for ethanol pervaporation to remove the ethanol out of the liquid stream.

Next to this, the product spectrum of syngas fermentation has been broadened by the deployment of strains and co-cultures for production of higher-value products as butyrate and caproate. The productivities of these strains still need to be enhanced, but could be promising for future studies. The biofilm formation in HFM reactors is especially interesting for these co-cultures, due to the higher biomass concentrations and the increased possibilities for inter-species mass transfer.

Next modelling steps that could be done are parametric studies among the HFM module characteristics. With such studies one could determine how indirectly influenceable parameters as the membrane thickness, the fibre spacing, the fibre length, the inner fibre diameter and different types of membranes (microporous, dense and composite) would influence the process performance.

Next to this, one could try to simplify the model. Such a simplified version of the model could be helpful for process design. Such a model could be developed by treating the HFM reactor as a black-box wherein the input parameters (e.g. syngas composition and flow rate, conversion and productivity) directly influence the output parameters. and As industrial membrane modules are quite small compared to other reactor equipment, strategies need to be derived to operate the plant the most efficiently. For example, membrane modules can be placed in cascade systems, with some modules in series and others in parallel-configurations. A simplified model of a HFM module could be used to model these systems. Next to that, a simplified model makes it possible to add other unit operations to the HFM module, so that the economical potential of syngas fermentation in HFM reactors could be determined.

Lastly, the results derived by experiments and modelling should be compared with other reactor configurations that could be used for syngas fermentation. This way, techno-economic comparison with other reactor types such as bubble column reactors could be made to determine the best configuration for synthesis gas fermentation.

10

Conclusions

By modelling syngas fermentation in the HFM reactor, the following conclusions were derived:

- In the lumen there are axial differences in gas concentration and velocity.
- There could be a high concentration loss in the membrane.
- The lumen gas flow rate governs a trade-off between mass transfer rate and yield.
- The main mass transfer resistances are both the membrane and liquid resistance.
- The $k_{L,CO}^{ov}a$ of the module ($343\,\mathrm{h}^{-1}$) is promising and corresponds to literature data.
- Compared with suspended biomass, a biofilm could lead to increased productivities.
- Microbial conversion is the limiting step for syngas fermentation in the modelled HFM reactor.
- Modelled trends in concentration and productivity match with experimental data.
- Of all process parameters, the reservoir inflow rate and lumen gas flow rate influence the performance of the modelled HFM reactor the most.
- The reservoir inflow rate governs a trade-off between ethanol concentration and productivity.
- The biofilm thickness and biomass concentration must be assumed while being highly sensitive.

In this thesis, the following research questions were derived in Chapter 1:

What is the impact of different input process parameters of a hollow fibre membrane biofilm reactor on the performance of the syngas fermentation process and how can they be used to improve the reactor performance? How can these effects be experimentally validated?

These research questions were answered by developing a computational model of a HFM reactor. It was derived that the reservoir liquid inflow rate and the lumen gas flow rate are the two process parameters that influence the performance of the HFM reactor the most. The lumen gas flow rate governs a trade-off between mass transfer rate and yield, while the reservoir inflow rate governs a trade-off between ethanol concentration and the volumetric ethanol productivity. Due to these detected trade-offs, it cannot directly be said how to improve the performance of the reactor as (techno-economic) decisions need to be made between the volumetric ethanol productivity, the desired ethanol concentration and the overall CO yield.

Next to this, several experiments have been proposed in Chapter 8. These experiments should determine whether the predicted values and trends correspond to data that can experimentally be retrieved.

Acknowledgements

First and foremost, I would like to thank Marina for welcoming me into her project. Her passion and affection for syngas fermentation is highly encouraging and inspiring. Prior to this project, I would have never thought that I could feel so much affection for a topic like this. This affection would have never been originated without all the conversations and discussions we have had. During the project Marina continuously helped me pushing the boundaries, raising the bar, to get the best out of me. I could imagine that this was not an easy job for her, as I am not easily satisfied and convinced. But, Marina managed to get beyond that, for which I am really grateful.

Furthermore, I would like to thank Adrie Straathof, Cristian Picioreanu and Ludovic Jourdin for participating in the thesis committee. I would like to thank Adrie for taking his time working on this project, mainly during our biweekly progress meetings, and for welcoming me into the BPE research group. I would like to thank Cristian for his assistance, sometimes spending hours solving complex problems, or troubleshooting in our favorite simulation software.

I would like to thank my office mates, Lisa, Javier, Koen and Renzo, and the rest of the BPE research group, for enabling me to share moments of hope and hopelessness, even with a non-alcoholic "beer". Thanks to Marijn and Britt taking the time for discussions mass transfer, syngas, metabolism and general modelling problems. I owe a beer to everybody who read parts of the thesis: my friends Marijn, Renzo, Koen and Alessandro, and my brother Jort.

I feel sorry for everybody to whom I complained about modelling problems and for this years NMMST students for helping Cristian in developing a very complex modelling assignment.

Last but not least, I would like to thank my parents and family for continuously supporting me during my studies. Although they could not really know in detail what the topic was about, they were still interested and concerned whether I had a good time and enjoyed working on the thesis.

Bibliography

Abrahamsom, J. B. (2019). *Conceptual Design and Evaluation of a Commercial Syngas Fermentation Process.* PhD thesis, Delft University of Technology.

Abrini, J., Naveau, H., and Nyns, E. J. (1994). Clostridium autoethanogenum, sp. nov., an anaerobic bacterium that produces ethanol from carbon monoxide. *Archives of Microbiology*, 161(4):345–351.

Abubackar, H. N., Veiga, M. C., and Kennes, C. (2011). Biological conversion of carbon monoxide: Rich syngas or waste gases to bioethanol. *Biofuels, Bioproducts and Biorefining*, 5(1):93–114.

Ahmadi Motlagh, A. R., Voller, V. R., and Semmens, M. J. (2006). Advective flow through membrane-aerated biofilms: Modeling results. *Journal of Membrane Science*, 273(1-2):143–151.

Ail, S. S. and Dasappa, S. (2016). Biomass to liquid transportation fuel via Fischer Tropsch synthesis - Technology review and current scenario. *Renewable and Sustainable Energy Reviews*, 58:267–286.

Anggraini, I. D., Keryanti, K., Kresnowati, M. T. A. P., Purwadi, R., Noda, R., Watanabe, T., and Setiadi, T. (2019). Bioethanol Production via Syngas Fermentation of Clostridium Ljungdahlii in a Hollow Fiber Membrane Supported Bioreactor. *International Journal of Technology*, 10(3):481.

Asimakopoulos, K., Gavala, H. N., and Skiadas, I. V. (2018). Reactor systems for syngas fermentation processes: A review. *Chemical Engineering Journal*, 348:732–744.

Atchariyawut, S., Jiraratananon, R., and Wang, R. (2008). Mass transfer study and modeling of gas-liquid membrane contacting process by multistage cascade model for CO2 absorption. *Separation and Purification Technology*, 63(1):15–22.

Benalcázar, E. A., Deynoot, B. G., Noorman, H., Osseweijer, P., and Posada, J. A. (2017). Production of bulk chemicals from lignocellulosic biomass via thermochemical conversion and syngas fermentation: a comparative technoeconomic and environmental assessment of different sitespecific supply chain configurations. *Biofuels, Bioproducts and Biorefining*, 11(5):861–886.

Blume, I., Schwering, P. J., Mulder, M. H., and Smolders, C. A. (1991). Vapour sorption and permeation properties of poly (dimethylsiloxane) films. *Journal of Membrane Science*, 61(C):85–97.

Blunt, W., Gaugler, M., Collet, C., Sparling, R., Gapes, D. J., Levin, D. B., and Cicek, N. (2019). Rheological Behavior of High Cell Density Pseudomonas putida LS46 Cultures during Production of Medium Chain Length Polyhydroxyalkanoate (PHA) Polymers. *Bioengineering*, 6(4):93.

Bothe, D. (2011). On the Maxwell-Stefan approach to multicomponent diffusion. In *Progress in Nonlinear Differential Equations and Their Application*, volume 80, pages 81–93. Springer US.

Box, G. E. P. (1976). Science and Statistics. Technical Report 356.

Bredwell, M., Srivastava, P., and Worden, R. (1999). Reactor Design Issues for Synthesis-Gas Fermentations. *Biotechnology Progress*, 15(5):834–844.

Brown, G. O. (2002). The history of the Darcy-Weisbach equation for pipe flow resistance. In *Proceedings of the Environmental and Water Resources History*, pages 34–43.

Brown, T. R. (2015). A techno-economic review of thermochemical cellulosic biofuel pathways. *Bioresource Technology*, 191:88–96.

Bryers, J. D. (1987). Biologically Active Surfaces: Processes Governing the Formation and Persistence of Biofilms. *Biotechnology Progress*, 3(2):57–68.

Casey, E., Glennon, B., and Hamer, G. (1999). Review of membrane aerated biofilm reactors. In *Resources, Conservation and Recycling*.

Chen, J., Daniell, J., Grin, D., Li, X., and Henson, M. A. (2018). Experimental testing of a spatiotemporal metabolic model for carbon monoxide fermentation with Clostridium autoethanogenum. *Biochemical Engineering Journal*, 129:64–73.

Chen, X. and Ni, B. J. (2016). Anaerobic conversion of hydrogen and carbon dioxide to fatty acids production in a membrane biofilm reactor: A modeling approach. *Chemical Engineering Journal*, 306:1092–1098.

Crane (1999). *Flow of Fluids Through Valves, Fittings and Pipe*. Crane Co., Chicago.

Cussler, E. L. (2011). *Diffusion: mass transfer in fluid systems*. Cambridge University Press, Cambridge; New York, 3 edition.

Dagley, S. and Hinshelwood, C. N. (1938). 365. Physicochemical aspects of bacterial growth. Part III. Influence of alcohols on the growth of Bact. lactis aerogenes. *Journal of the Chemical Society (Resumed)*, pages 1942–1948.

Danckwerts, P. V. (1953). Continuous flow systems. Distribution of residence times. *Chemical Engineering Science*, 2(1):1–13.

de Medeiros, E. M., Posada, J. A., Noorman, H., and Filhob, R. M. (2019). Modeling and Multi-Objective Optimization of Syngas Fermentation in a Bubble Column Reactor. In *Computer Aided Chemical Engineering*, volume 46, pages 1531–1536. Elsevier B.V.

Devarapalli, M., Lewis, R., and Atiyeh, H. (2017). Continuous Ethanol Production from Synthesis Gas by Clostridium ragsdalei in a Trickle-Bed Reactor. *Fermentation*, 3(2):23.

Diender, M., Stams, A. J., and Sousa, D. Z. (2016). Production of medium-chain fatty acids and higher alcohols by a synthetic co-culture grown on carbon monoxide or syngas. *Biotechnology for Biofuels*, 9(1).

Dreszer, C., Wexler, A. D., Drusová, S., Overdijk, T., Zwijnenburg, A., Flemming, H. C., Kruithof, J. C., and Vrouwenvelder, J. S. (2014). In-situ biofilm characterization in membrane systems using Optical Coherence Tomography: Formation, structure, detachment and impact of flux change. *Water Research*.

Drioli, E., Criscuoli, A., and Curcio, E. (2006). *Membrane contactors : fundamentals, applications and potentialities*. Elsevier.

Drzyzga, O., Revelles, O., Durante-Rodríguez, G., Díaz, E., García, J. L., and Prieto, A. (2015). New challenges for syngas fermentation: towards production of biopolymers. *Journal of Chemical Technology & Biotechnology*, 90(10):1735–1751.

Edel, M., Horn, H., and Gescher, J. (2019). Biofilm systems as tools in biotechnological production. *Applied Microbiology and Biotechnology*, 103(13):5095–5103.

Erickson, B., Nelson, and Winters, P. (2012). Perspective on opportunities in industrial biotechnology in renewable chemicals. *Biotechnology Journal*, 7(2):176–185.

Fast, A. G. and Papoutsakis, E. T. (2012). Stoichiometric and energetic analyses of non-photosynthetic CO2-fixation pathways to support synthetic biology strategies for production of fuels and chemicals. *Current Opinion in Chemical Engineering*, 1(4):380–395.

Fernández-Naveira, ., Abubackar, H. N., Veiga, M. C., and Kennes, C. (2016). Carbon monoxide bioconversion to butanol-ethanol by Clostridium carboxidivorans: kinetics and toxicity of alcohols. *Applied Microbiology and Biotechnology*, 100(9):4231–4240.

Freitas Dos Santos, L. M., Pavasant, P., Strachan, L. F., Pistikopoulos, E. N., and Livingston, A. G. (1997). Membrane attached biofilms for waste treatment - Fundamentals and applications. *Pure and Applied Chemistry*, 69(11):2459–2469.

Fuller, E. N., Schettler, P. D., and Giddings, J. C. (1966). A new method for prediction of binary gas-phase diffusion coefficients. *Industrial and Engineering Chemistry*, 58(5):18–27.

Galadima, A. and Muraza, O. (2015). From synthesis gas production to methanol synthesis and potential upgrade to gasoline range hydrocarbons: A review. *Journal of Natural Gas Science and Engineering*, 25:303–316.

Ghidossi, R., Veyret, D., and Moulin, P. (2006). Computational fluid dynamics applied to membranes: State of the art and opportunities. *Chemical Engineering and Processing: Process Intensification*, 45(6):437–454.

Graham, T. (1863). On the Molecular Mobility of Gases. *Philosophical Transactions of the Royal Society of London*, 153:385–405.

Haddadi, B., Jordan, C., Miltner, M., and Harasek, M. (2018). Membrane modeling using CFD: Combined evaluation of mass transfer and geometrical influences in 1D and 3D. *Journal of Membrane Science*, 563:199–209.

Hashemifard, S. A., Ismail, A. F., Matsuura, T., and Dashtarzhandi, M. R. (2015). Performance of silicon rubber coated polyetherimide hollow fibers for CO2 removal via a membrane contactor. *RSC Advances*, 5(60):48442–48455.

Heijnen, J. J. and Van Dijken, J. P. (1992). In search of a thermodynamic description of biomass yields for the chemotrophic growth of microorganisms. *Biotechnology and Bioengineering*, 39(8):833–858.

Hermann, B. G., Blok, K., and Patel, M. K. (2007). Producing bio-based bulk chemicals using industrial biotechnology saves energy and combats climate change. *Environmental Science and Technology*, 41(22):7915–7921.

Horn, H. and Lackner, S. (2014). Modeling of Biofilm Systems: A Review. In Muffler, K. and Ulber, R., editors, *Productive Biofilms*, pages 53–76. Springer International Publishing, Cham.

Huffer, S., Clark, M. E., Ning, J. C., Blanch, H. W., and Clark, D. S. (2011). Role of alcohols in growth, lipid composition, and membrane fluidity of yeasts, bacteria, and archaea. *Applied and Environmental Microbiology*, 77(18):6400–6408.

Jack, J., Lo, J., Maness, P. C., and Ren, Z. J. (2019). Directing Clostridium ljungdahlii fermentation products via hydrogen to carbon monoxide ratio in syngas. *Biomass and Bioenergy*, 124:95–101.

Janssen, L. and Warmoeskerken, M. (2006). *Transport phenomena data companion.* VSSD, Delft.

Kavousi, F., Syron, E., Semmens, M., and Casey, E. (2016). Hydrodynamics and gas transfer performance of confined hollow fibre membrane modules with the aid of computational fluid dynamics. *Journal of Membrane Science*, 513(1):117–128.

Kim, B., Bellows, P., Datta, R., and Zeikus, J. (1984). Control of Carbon and Electron Flow in Clostridium acetobutylicum Fermentations: Utilization of. *Applied and Environmental Microbiology*, 48(4):764–770.

Klasson, K. T., Ackerson, M. D., Clausen, E. C., and Gaddy, J. L. (1991). Bioreactor design for synthesis gas fermentations. *Fuel*, 70(5):605–614.

Klasson, K. T., Ackerson, M. D., Clausen, E. C., and Gaddy, J. L. (1992). Bioconversion of synthesis gas into liquid or gaseous fuels. *Enzyme and Microbial Technology*, 14(8):602–608.

Kleerebezem, R. and Van Loosdrecht, M. C. M. (2010). A generalized method for thermodynamic state analysis of environmental systems. *Critical Reviews in Environmental Science and Technology*, 40(1):1–54.

Krishna, R. and Wesselingh, J. A. (1997). The Maxwell-Stefan approach to mass transfer. *Chemical Engineering Science*, 52(6):861–911.

Kumar, A., Dewulf, J., and Van Langenhove, H. (2008). Membrane-based biological waste gas treatment. *Chemical Engineering Journal*, 136(2-3):82–91.

Kumar, P. S., Hogendoorn, J. A., Feron, P. H., and Versteeg, G. F. (2003). Approximate solution to predict the enhancement factor for the reactive absorption of a gas in a liquid flowing through a microporous membrane hollow fiber. *Journal of Membrane Science*, 213(1-2):231–245.

Kwok, W. K., Picioreanu, C., Ong, S. L., van Loosdrecht, M. C. M., Ng, W. J., and Heijnen, J. J. (1998). Influence of biomass production and detachment forces on biofilm structures in a biofilm airlift suspension reactor. *Biotechnology and Bioengineering*, 58(4):400–407.

Lewis, W. K. and Whitman, W. G. (1924). Principles of Gas Absorption. *Industrial and Engineering Chemistry*, 16(12):1215–1220.

Li, X. and Henson, M. A. (2019). Metabolic modeling of bacterial co-culture systems predicts enhanced carbon monoxide-to-butyrate conversion compared to monoculture systems. *Biochemical Engineering Journal*, 151:107338.

Liew, F. M., Martin, M. E., Tappel, R. C., Heijstra, B. D., Mihalcea, C., and Köpke, M. (2016). Gas Fermentation-A flexible platform for commercial scale production of low-carbon-fuels and chemicals from waste and renewable feedstocks. *Frontiers in Microbiology*, 7:1–28.

Lin, Y. and Tanaka, S. (2006). Ethanol fermentation from biomass resources: current state and prospects. *Applied Microbiology and Biotechnology*, 69(6):627–642.

Lopez, L., Velasco, J., Montes, V., Marinas, A., Cabrera, S., Boutonnet, M., and Järås, S. (2015). Synthesis of Ethanol from Syngas over Rh/MCM-41 Catalyst: Effect of Water on Product Selectivity. *Catalysts*, 5(4):1737–1755.

Martin, K. J., Picioreanu, C., and Nerenberg, R. (2013). Multidimensional modeling of biofilm development and fluid dynamics in a hydrogen-based, membrane biofilm reactor (MBfR). *Water Research*, 47(13):4739–4751.

Martin, K. J., Picioreanu, C., and Nerenberg, R. (2015). Assessing microbial competition in a hydrogen-based membrane biofilm reactor (MBfR) using multidimensional modeling. *Biotechnology and Bioengineering*, 112(9):1843–1853.

Matson, J. V. and Characklis, W. G. (1976). Diffusion into microbial aggregates. *Water Research*, 10(10):877–885.

Matsumoto, S., Terada, A., and Tsuneda, S. (2007). Modeling of membrane-aerated biofilm: Effects of C/N ratio, biofilm thickness and surface loading of oxygen on feasibility of simultaneous nitrification and denitrification. *Biochemical Engineering Journal*, 37(1):98–107.

McKendry, P. (2002). Energy production from biomass (part 3): Gasification technologies. *Bioresource Technology*, 83(1):55–63.

Medeiros, E. M., Posada, J. A., Noorman, H., and Filho, R. M. (2019). Dynamic modeling of syngas fermentation in a continuous stirredtank reactor: Multiresponse parameter estimation and process optimization. *Biotechnology and Bioengineering*, 116(10):2473–2487.

Merkel, T. C., Bondar, V. I., Nagai, K., Freeman, B. D., and Pinnau, I. (2000). Gas sorption, diffusion, and permeation in poly(dimethylsiloxane). *Journal of Polymer Science, Part B: Polymer Physics*, 38(3):415–434.

Meyer, C. L., McLaughlin, J. K., and Papoutsakis, E. T. (1985). The effect of CO on growth and product formation in batch cultures of Clostridium acetobutylicum. *Biotechnology Letters*, 7(1):37–42.

Mohammadi, M., Mohamed, A. R., Najafpour, G. D., Younesi, H., and Uzir, M. H. (2014). Kinetic studies on fermentative production of biofuel from synthesis gas using clostridium ljungdahlii. *The Scientific World Journal*, 2014:1–8.

Mohammadi, M., Younesi, H., Najafpour, G., and Mohamed, A. R. (2012). Sustainable ethanol fermentation from synthesis gas by Clostridium ljungdahlii in a continuous stirred tank bioreactor. *Journal of Chemical Technology & Biotechnology*, 87(6):837–843.

Molitor, B., Richter, H., Martin, M. E., Jensen, R. O., Juminaga, A., Mihalcea, C., and Angenent, L. T. (2016). Carbon recovery by fermentation of CO-rich off gases Turning steel mills into biorefineries. *Bioresource Technology*, 215:386–396.

Montoya, J. P. (2010). Membrane Gas Exchange Using Hollow Fiber Membranes to Separate Gases from Liquid and Gaseous Streams. Technical report, MedArray, Inc.

Munasinghe, P. C. and Khanal, S. K. (2010). Biomass-derived syngas fermentation into biofuels: Opportunities and challenges. *Bioresource Technology*, 101:5013–5022.

Munasinghe, P. C. and Khanal, S. K. (2012). Syngas fermentation to biofuel: Evaluation of carbon monoxide mass transfer and analytical modeling using a composite hollow fiber (CHF) membrane bioreactor. *Bioresource Technology*, 122:130–136.

Orgill, J. J., Abboud, M. C., Atiyeh, H. K., Devarapalli, M., Sun, X., and Lewis, R. S. (2019). Measurement and prediction of mass transfer coefficients for syngas constituents in a hollow fiber reactor. *Bioresource Technology*, 276:1–7.

Orgill, J. J., Atiyeh, H. K., Devarapalli, M., Phillips, J. R., Lewis, R. S., and Huhnke, R. L. (2013). A comparison of mass transfer coefficients between trickle-bed, Hollow fiber membrane and stirred tank reactors. *Bioresource Technology*, 133:340–346.

Pavasant, P., dos Santos, L. M. F., Pistikopoulos, E. N., and Livingston, A. G. (1996). Prediction of optimal biofilm thickness for membrane-attached biofilms growing in an extractive membrane bioreactor. *Biotechnology and Bioengineering*, 52(3):373–386.

Pereira, J. P., Verheijen, P. J., and Straathof, A. J. (2016). Growth inhibition of S. cerevisiae, B. subtilis, and E. coli by lignocellulosic and fermentation products. *Applied Microbiology and Biotechnology*, 100(21):9069–9080.

Perez-Calleja, P., Aybar, M., Picioreanu, C., Esteban-Garcia, A., Martin, K., and Nerenberg, R. (2017). Periodic venting of MABR lumen allows high removal rates and high gas-transfer efficiencies. *Water Research*, 121:349–360.

Perry, R. H., Green, D. W., and Maloney, J. O. (1997). *Perry's chemical engineers' handbook*. McGraw-Hill, New York, 7 edition.

Peyton, B. M. and Characklis, W. G. (1993). A statistical analysis of the effect of substrate utilization and shear stress on the kinetics of biofilm detachment. *Biotechnology and Bioengineering*, 41(7):728–735.

Phillips, J. R., Klasson, K. T., Clausen, E. C., and Gaddy, J. L. (1993). Biological production of ethanol from coal synthesis gas - Medium development studies. *Applied Biochemistry and Biotechnology*, 39-40(1):559–571.

Piccolo, C. and Bezzo, F. (2009). A techno-economic comparison between two technologies for bioethanol production from lignocellulose. *Biomass and Bioenergy*, 33:478–491.

Picioreanu, C., van Loosdrecht, M. C. M., and Heijnen, J. J. (2001). Two-dimensional model of biofilm detachment caused by internal stress from liquid flow. *Biotechnology & Bioengineering*, 72(2):205–218.

Popper, K. R. (1963). Science as Falsification. *Conjectures and Refutations*, pages 33–39.

Raja, L. L., Kee, R. J., Deutschmann, O., Warnatz, J., and Schmidt, L. D. (2000). A critical evaluation of Navier-Stokes, boundary-layer, and plug-flow models of the flow and chemistry in a catalytic-combustion monolith. *Catalysis Today*, 59(1-2):47–60.

Ramió-Pujol, S., Ganigué, R., Bañeras, L., and Colprim, J. (2018). Effect of ethanol and butanol on autotrophic growth of model homoacetogens. *FEMS Microbiology Letters*, 365(10).

Reid, R. C., Prausnitz, J. M., and Poling, B. E. (1987). *The properties of gases and liquids*. McGraw-Hill, New York, 4th edition.

Reij, M. W., Keurentjes, J. T., and Hartmans, S. (1998). Membrane bioreactors for waste gas treatment. *Journal of Biotechnology*, 59(3):155–167.

Richter, H., Martin, M. E., and Angenent, L. T. (2013). A two-stage continuous fermentation system for conversion of syngas into ethanol. *Energies*, 6(8):3987–4000.

Richter, H., Molitor, B., Wei, H., Chen, W., Aristilde, L., and Angenent, L. T. (2016). Ethanol production in syngas-fermenting Clostridium ljungdahlii is controlled by thermodynamics rather than by enzyme expression. *Energy & Environmental Science*, 9(7):2392–2399.

Rittman, B. E. (1982). The effect of shear stress on biofilm loss rate. *Biotechnology and Bioengineering*, 24(2):501–506.

Robb, W. L. (1968). THIN SILICONE MEMBRANES-THEIR PERMEATION PROPERTIES AND SOME APPLICATIONS. *Annals of the New York Academy of Sciences*, 146(1 Materials in):119–137.

Robert, H., Rathin, D., Shih-perng, T., and Rahul, B. (2014). *U.S. Patent No. 20140377822A1*. U.S. Patent and Trademark Office, Washington, DC.

Rodgers, R. C. and Hill, G. E. (1978). Equations for vapour pressure versus temperature: Derivation and use of the antoine equation on a hand-held programmable calculator. *British Journal of Anaesthesia*, 50(5):415–424.

Sander, R. (2015). Compilation of Henry's law constants (version 4.0) for water as solvent. *Atmos. Chem. Phys*, 15:4399–4981.

Sathish, A., Sharma, A., Gable, P., Skiadas, I., Brown, R., and Wen, Z. (2019). A novel bulk-gas-to-atomized-liquid reactor for enhanced mass transfer efficiency and its application to syngas fermentation. *Chemical Engineering Journal*, 370:60–70.

Seader, J. D., Henley, E. J., and Roper, D. K. (2011). *Separation process principles : chemical and biochemical operations*. John Wiley Inc.

Shao, L., Low, B. T., Chung, T. S., and Greenberg, A. R. (2009). Polymeric membranes for the hydrogen economy: Contemporary approaches and prospects for the future.

Shen, Y., Brown, R., and Wen, Z. (2014a). Enhancing mass transfer and ethanol production in syngas fermentation of Clostridium carboxidivorans P7 through a monolithic biofilm reactor. *Applied Energy*, 136:68–76.

Shen, Y., Brown, R., and Wen, Z. (2014b). Syngas fermentation of Clostridium carboxidivoran P7 in a hollow fiber membrane biofilm reactor: Evaluating the mass transfer coefficient and ethanol production performance. *Biochemical Engineering Journal*, 85:21–29.

Shen, Y., Brown, R. C., and Wen, Z. (2017). Syngas fermentation by Clostridium carboxidivorans P7 in a horizontal rotating packed bed biofilm reactor with enhanced ethanol production. *Applied Energy*, 187:585–594.

Shirazian, S., Moghadassi, A., and Moradi, S. (2009). Numerical simulation of mass transfer in gas-liquid hollow fiber membrane contactors for laminar flow conditions. *Simulation Modelling Practice and Theory*, 17(4):708–718.

Souza, G. M., Ballester, M. V. R., de Brito Cruz, C. H., Chum, H., Dale, B., Dale, V. H., Fernandes, E. C., Foust, T., Karp, A., Lynd, L., Maciel Filho, R., Milanez, A., Nigro, F., Osseweijer, P., Verdade, L. M., Victoria, R. L., and Van der Wielen, L. (2017). The role of bioenergy in a climate-changing world. *Environmental Development*, 23:57–64.

Stern, S. A. (1968). The barrer permeability unit. *Journal of Polymer Science Part A-2: Polymer Physics*, 6(11):1933–1934.

Sutherland, W. (1893). The viscosity of gases and molecular force. *The London, Edinburgh, and Dublin Philosophical Magazine and Journal of Science*, 36(223):507–531.

Tijhuis, L., Van Loosdrecht, M. C., and Heijnen, J. J. (1993). A thermodynamically based correlation for maintenance gibbs energy requirements in aerobic and anaerobic chemotrophic growth. *Biotechnology and Bioengineering*, 42(4):509–519.

Tijhuis, L., van Loosdrecht, M. C. M., and Heijnen, J. J. (1994). Formation and growth of heterotrophic aerobic biofilms on small suspended particles in airlift reactors. *Biotechnology and Bioengineering*, 44(5):595–608.

Valgepea, K., De Souza Pinto Lemgruber, R., Abdalla, T., Binos, S., Takemori, N., Takemori, A., Tanaka, Y., Tappel, R., Köpke, M., Simpson, S. D., Nielsen, L. K., and Marcellin, E. (2018). H2 drives metabolic rearrangements in gas-fermenting Clostridium autoethanogenum. *Biotechnology for Biofuels*, 11(1):1–15.

Vassilev, S. V., Baxter, D., Andersen, L. K., Vassileva, C. G., and Morgan, T. J. (2012). An overview of the organic and inorganic phase composition of biomass. *Fuel*, 94:1–33.

Wang, C. Y., Mercer, E., Kamranvand, F., Williams, L., Kolios, A., Parker, A., Tyrrel, S., Cartmell, E., and McAdam, E. J. (2017a). Tube-side mass transfer for hollow fibre membrane contactors operated in the low Graetz range. *Journal of Membrane Science*, 523:235–246.

Wang, Y.-Q., Yu, S.-J., Zhang, F., Xia, X.-Y., and Zeng, R. J. (2017b). Enhancement of acetate productivity in a thermophilic (55ă°C) hollow-fiber membrane biofilm reactor with mixed culture syngas (H2/CO2) fermentation. *Applied Microbiology and Biotechnology*, 101(6):2619–2627.

Wilke, C. R. (1950). A viscosity equation for gas mixtures. *The Journal of Chemical Physics*, 18(4):517–519.

Williams, C. L., Westover, T. L., Emerson, R. M., Tumuluru, J. S., and Li, C. (2016). Sources of Biomass Feedstock Variability and the Potential Impact on Biofuels Production. *Bioenergy Research*, 9(1):1–14.

Xu, H., Liang, C., Chen, X., Xu, J., Yu, Q., Zhang, Y., and Yuan, Z. (2020). Impact of exogenous acetate on ethanol formation and gene transcription for key enzymes in Clostridium autoethanogenum grown on CO. *Biochemical Engineering Journal*, 155:107470.

Xu, H., Liang, C., Yuan, Z., Xu, J., Hua, Q., and Guo, Y. (2017). A study of CO/syngas bioconversion by Clostridium autoethanogenum with a flexible gas-cultivation system. *Enzyme and Microbial Technology*, 101:24–29.

Yasin, M., Jang, N., Lee, M., Kang, H., Aslam, M., Bazmi, A. A., and Chang, I. S. (2019). Bioreactors, gas delivery systems and supporting technologies for microbial synthesis gas conversion process. *Bioresource Technology Reports*, 7:100207.

Yasin, M., Jeong, Y., Park, S., Jeong, J., Lee, E. Y., Lovitt, R. W., Kim, B. H., Lee, J., and Chang, I. S. (2015). Microbial synthesis gas utilization and ways to resolve kinetic and mass-transfer limitations. *Bioresource Technology*, 177:361–374.

Yasin, M., Park, S., Jeong, Y., Lee, E. Y., Lee, J., and Chang, I. S. (2014). Effect of internal pressure and gas/liquid interface area on the CO mass transfer coefficient using hollow fibre membranes as a high mass transfer gas diffusing system for microbial syngas fermentation. *Bioresource Technology*, 169:637–643.

Younesi, H., Najafpour, G., and Mohamed, A. R. (2005). Ethanol and acetate production from synthesis gas via fermentation processes using anaerobic bacterium, Clostridium ljungdahlii. *Biochemical Engineering Journal*, 27(2):110–119.

Zhang, F., Ding, J., Zhang, Y., Chen, M., Ding, Z. W., van Loosdrecht, M. C., and Zeng, R. J. (2013). Fatty acids production from hydrogen and carbon dioxide by mixed culture in the membrane biofilm reactor. *Water Research*, 47(16):6122–6129.

A

Models and mass balances

Table A.1: All models described in the report are tabulated in this figure. The green cells depict what was described in this column was taken into account in the model, the orange cells mean that it was incorporated in the model, but was not taken into account in the results of the model and the brown cells mean it was not taken into account in the model.

Model name	Chapter / Appendix	Components						Biomass		Compartments					Variable parameter	Range	Notes
		CO	CO_2	H_2	N_2	H_2O	EtOH	Susp.	Biofilm	Gas	Mem	Biof	Liq	Res			
M_gasphase	3	🟩	🟩	🟩	🟩	🟫	🟫	🟫	🟫	🟩	🟫	🟫	🟫	🟫	-	-	
M_membrane	4	🟩	🟩	🟩	🟩	🟫	🟫	🟫	🟫	🟩	🟩	🟫	🟫	🟫	-	-	
M_memb_Fgin	4	🟩	🟩	🟩	🟩	🟫	🟫	🟫	🟫	🟩	🟩	🟫	🟫	🟫		4 - 400 mL/min	
M_closed	4	🟩	🟩	🟩	🟩	🟫	🟫	🟫	🟫	🟩	🟩	🟫	🟫	🟫	-	-	
M_liq_kla_xCO	5	🟩	🟩	🟧	🟩	🟫	🟫	🟫	🟫	🟩	🟩	🟫	🟩	🟫		1E-8 - 1	
M_liq_kla_Re	5	🟩	🟩	🟧	🟧	🟫	🟫	🟫	🟫	🟩	🟩	🟫	🟩	🟫		0.1 - 7	
M_liq_susp	5	🟩	🟩	🟧	🟧	🟫	🟩	🟩	🟫	🟩	🟩	🟫	🟩	🟫		0.1 - 10 g/L	
M_biof_cx	5	🟩	🟩	🟧	🟧	🟫	🟩	🟫	🟩	🟩	🟩	🟩	🟩	🟫		10 - 60 g/L	
M_res_Fgresin	6/H	🟩	🟩	🟧	🟩	🟩	🟩	🟩	🟩	🟩	🟩	🟩	🟩	🟩		0.1 - 100 mL/min	
M_res_Flresin	6/7/F/H	🟩	🟩	🟧	🟩	🟩	🟩	🟩	🟩	🟩	🟩	🟩	🟩	🟩		0.025 - 2 mL/min	
M_res_Flmodin	6/E	🟩	🟩	🟧	🟩	🟩	🟩	🟩	🟩	🟩	🟩	🟩	🟩	🟩		0.4 - 500 mL/min	
M_res_Vres	6	🟩	🟩	🟧	🟩	🟩	🟩	🟩	🟩	🟩	🟩	🟩	🟩	🟩		0.25 - 1.5 L	
M_param_Fgin	7	🟩	🟩	🟧	🟩	🟩	🟩	🟩	🟩	🟩	🟩	🟩	🟩	🟩		3 - 200 mL/min	
M_param_Pgas	7	🟩	🟩	🟧	🟩	🟩	🟩	🟩	🟩	🟩	🟩	🟩	🟩	🟩		1 - 1.5 atm	
M_param_Pliq	7	🟩	🟩	🟧	🟩	🟩	🟩	🟩	🟩	🟩	🟩	🟩	🟩	🟩		1 - 2 atm	
M_sens	7	🟩	🟩	🟧	🟩	🟩	🟩	🟩	🟩	🟩	🟩	🟩	🟩	🟩		10 - 60 g/L 20 - 240 µm	
M_res_Flres_Inhib	F	🟩	🟩	🟧	🟩	🟩	🟩	🟩	🟩	🟩	🟩	🟩	🟩	🟩		0.025 - 2 mL/min	compares the inhibition models
M_biof_dbiof	G	🟩	🟩	🟧	🟧	🟫	🟩	🟫	🟩	🟩	🟩	🟩	🟩	🟫		10 - 300 µm	
M_param_Pgas_Inhib	I	🟩	🟩	🟧	🟩	🟩	🟩	🟩	🟩	🟩	🟩	🟩	🟩	🟩		1 - 1.5 atm	inhibition model de Medeiros

Mass balances

Table A.2: Mass balance for the gas compartment in the gas phase model (M_gasphase), based on Equation 3.5. The amount of gas entering the gas phase via the inlet and the membrane and leaving via the gas outlet is tabulated for each compound (in $\mathrm{mol\,s^{-1}}$). The mass balance error is provided in $\mathrm{mol\,s^{-1}}$ and as percentage of the amount entering via the inlet.

Compound	Gas inlet	In via membrane	Gas outlet	MB error ($\mathrm{mol\,s^{-1}}$)	MB error (%)
CO	1.06E-07	-1.36E-08	-9.26E-08	-8.15E-11	-0.0768%
CO_2	1.52E-07	-9.98E-08	-5.20E-08	-1.91E-10	-0.1261%
H_2	6.82E-08	-1.71E-09	-6.66E-08	-4.21E-11	-0.0617%
N_2	3.79E-07	-4.02E-08	-3.39E-07	-2.03E-10	-0.0535%

Table A.3: Mass balance for the membrane compartment in the membrane model (M_membrane), based on Equation 4.7. The amount of gas entering the membrane phase from the gas phase and leaving at the membrane-biofilm interface is tabulated for each compound (in $\mathrm{mol\,s^{-1}}$). The mass balance error is provided in $\mathrm{mol\,s^{-1}}$ and as percentage of the amount entering via the inlet.

Compound	Membrane inflow	Membrane outflow	MB error ($\mathrm{mol\,s^{-1}}$)	MB error (%)
CO	1.35677E-09	-1.3657E-09	-8.95827E-12	-0.660%
CO_2	3.95511E-08	-3.9812E-08	-2.61142E-10	-0.660%
H_2	1.68338E-09	-1.6945E-09	-1.11147E-11	-0.660%
N_2	2.93922E-09	-2.9586E-09	-1.94066E-11	-0.660%

Table A.4: Mass balance for the biofilm compartment in the biofilm model (M_biof_cx) ($c_{b,x} = 15\,\mathrm{g_x L^{-1}}$), based on Equation 5.4. The amount of gas entering the biofilm from the membrane from the gas phase and leaving at the biofilm-liquid interface and the amount produced (+) and consumed (-) are tabulated for each compound (in $\mathrm{mol\,s^{-1}}$). The mass balance error is provided in $\mathrm{mol\,s^{-1}}$ and as percentage of the amount entering via the inlet.

Compound	In via membrane	Biofilm outflow	Reaction	MB error ($\mathrm{mol\,s^{-1}}$)	MB error (%)
CO	7.8808E-09	-2.94E-09	-5.23E-09	-2.94E-10	-3.729%
CO_2	-5.6682E-10	-2.82E-09	3.4619E-09	7.95E-11	2.296%
H_2	5.2123E-17	-5.34E-17	-	-1.32E-18	-2.525%
N_2	3.3844E-17	-3.47E-17	-	-8.55E-19	-2.526%
EtOH	-	-8.4063E-10	8.3981E-10	-8.20E-13	-0.098%

Table A.5: Mass balance for the liquid compartment in the biofilm model (M_biof_cx) ($c_{b,x} = 15\,\mathrm{g_x L^{-1}}$), based on Equation 5.5. The amount of solutes leaving the biofilm at the biofilm-liquid interface and the amount that leaves the shell at the outlet are tabulated for each compound (in $\mathrm{mol\,s^{-1}}$). The mass balance error is provided in $\mathrm{mol\,s^{-1}}$ and as percentage of the amount entering via the inlet.

Compound	In via biofilm	Liquid outlet	MB error ($\mathrm{mol\,s^{-1}}$)	MB error (%)
CO	2.94E-09	-2.94E-09	-3.70E-12	-0.126%
CO_2	2.8156E-09	-2.82E-09	-3.20E-12	-0.114%
H_2	5.3439E-17	-5.35E-17	-7.00E-20	-0.131%
N_2	3.4699E-17	-3.47E-17	-4.30E-20	-0.124%
EtOH	8.4063E-10	-8.41E-10	9.79E-15	0.001%

B

Characteristic times

The time necessary for transport phenomena can be estimated by calculating the characteristic times for these phenomena. Although the HFM reactor is modelled in a 2D geometry, the characteristic times are, for simplicity, calculated based on assuming an 1D geometry and for CO transport. In general, the characteristic times for convection, diffusion and reaction can be calculated from the general transport equation (Equation B.1). First the equation is divided by its characteristic concentration to Equation B.2. As transport needs to be performed over a certain distance, for diffusion and convection the nabla operators can be substituted by the characteristic transport distance L_c (Equation B.3). Hereafter, it is possible to substitute the characteristic length for the distance necessary in each transport phenomenon and split the equations to an equation for diffusion (Equation B.4), convection (Equation B.5) and reaction (Equation B.6).

For all transport processes, the characteristic times are derived and tabulated in Table B.1 for a scenario similar to the biofilm model in Chapter 5 (M_biof_cx). The values used for the calculation of these times are provided in Table B.2.

$$\frac{\partial c_{CO}}{\partial t} = -D_{CO}\nabla^2 c_{CO} + v\nabla c_{CO} + \frac{q_{CO,max}c_{CO}}{K_{p,CO} + c_{CO} + \frac{c_{CO}^2}{K_{I,CO}}} c_x \tag{B.1}$$

$$\frac{\partial}{\partial t} = -D_{CO}\nabla^2 + v\nabla + \frac{q_{CO,max}}{K_{p,CO} + c_{CO} + \frac{c_{CO}^2}{K_{I,CO}}} c_x \tag{B.2}$$

$$\frac{\partial}{\partial t} = -D_{CO}\frac{1}{L_c^2} + v\frac{1}{L_c} + \frac{q_{CO,max}}{K_{p,CO} + c_{CO} + \frac{c_{CO}^2}{K_{I,CO}}} c_x \tag{B.3}$$

$$\tau_{\text{diff}} = \frac{L_c^2}{D_{CO}} \tag{B.4}$$

$$\tau_{\text{conv}} = \frac{L_c}{v} \tag{B.5}$$

$$\tau_{\text{reac}} = \frac{K_{p,CO} + c_{CO} + \frac{c_{CO}^2}{K_{I,CO}}}{q_{CO,max}c_x} \tag{B.6}$$

From this analysis can be found that axial diffusion is all compartments can be neglected. In the gas phase, radial diffusion is much faster than axial convection. This indicates that radial concentration gradients are not expected. Axial diffusion in the membrane is not expected to lead to concentration gradients as radial diffusion is significantly faster. Biofilm radial diffusion and reaction are in the same order of magnitude. This means that both phenomena will play an important role in the depletion of CO and need to be examined in detail. Liquid convection and radial diffusion are in the same order of magnitude as well. They have both an important contribution to mixing in the shell liquid phase and are therefore important to take into account as well.

As membrane radial diffusion is expected to be in the same order of magnitude as diffusion in the biofilm and reaction, it is expected that these phenomena govern the overall performance of the reactor system. Gas phase radial diffusion is expected not to affect this performance as its characteristic time is very low compared to the other phenomena.

Table B.1: For all transport processes, the formula for their characteristic time and their value based on the values in Table B.2 are calculated.

Phase	Phenomena	Symbol	Formula	Order of magnitude (s)
Gas	Convection	$\tau_{\text{conv},g}$	$\frac{L_f}{v_g}$	10^1-10^2
	Axial diffusion	$\tau_{\text{diff,ax},g}$	$\frac{L_f^2}{D_{g,CO,av}}$	10^3-10^4
	Radial diffusion	$\tau_{\text{diff,rad},g}$	$\frac{(0.5d_i)^2}{D_{CO,g,av}}$	10^{-3}-10^{-2}
Membrane	Axial diffusion	$\tau_{\text{diff,ax},m}$	$\frac{L_f^2}{D_{m,CO}}$	10^7-10^8
	Radial diffusion	$\tau_{\text{diff,rad},m}$	$\frac{d_m^2}{D_{m,CO}}$	10^0-10^1
Biofilm	Axial diffusion	$\tau_{\text{diff,ax},b}$	$\frac{L_f^2}{D_{b,CO}}$	10^7-10^8
	Radial diffusion	$\tau_{\text{diff,rad},b}$	$\frac{d_b^2}{D_{b,CO}}$	10^0-10^1
	Reaction	τ_{reac}	$\frac{K_{p,CO}+c_{CO}+\frac{c_{CO}^2}{K_{I,CO}}}{q_{CO,max}c_x}$	10^{-1}-10^1
Liquid	Convection	$\tau_{\text{conv},l}$	$\frac{L_f}{v_l}$	10^2-10^3
	Axial diffusion	$\tau_{\text{diff,ax},l}$	$\frac{L_f^2}{D_{l,CO}}$	10^7-10^8
	Radial diffusion	$\tau_{\text{diff,rad},l}$	$\frac{d_l^2}{D_{l,CO}}$	10^1-10^2

Table B.2: Values used for the calculation of the characteristic times provided in Table B.1.

Parameter	Symbol	Value	Unit	Reference
Fibre length	L_f	0.4	m	-
Fibre diameter	d_i	340	μm	-
Membrane thickness	d_m	110	μm	-
Biofilm thickness	d_b	100	μm	-
Liquid phase radius	d_l	515	mm.s^{-1}	-
Gas phase velocity	v_g	6.675	mm.s^{-1}	-
Liquid phase velocity	v_l	2.2667	mm.s^{-1}	-
CO saturation constant	$K_{p,CO}$	0.0178	mol$_{CO}$.m^{-3}	Mohammadi et al. (2014)
CO inhibition constant	$K_{I,CO}$	0.5101	mol$_{CO}$.m^{-3}	Mohammadi et al. (2014)
Maximum uptake rate	$q_{CO,max}$	0.0343	mol$_{CO}$.g$_x^{-1}$.h^{-1}	Mohammadi et al. (2014)
Biomass concentration	c_x	15	g.L^{-1}	-

C

Membrane specifications

The packing density ϕ and fibre spacing of the membrane module were calculated based on Equations C.1 and C.2. With the total module volume, the diameter of the module was calculated according to Equation C.3.

$$\phi = \frac{V_g + V_m}{V_{\text{shell}}} = 9.7\,\% \tag{C.1}$$

$$d_{\text{spacing}} = 2\left(r_l - r_{mb}^{\text{int}}\right) = 0.123\,\text{cm} \quad \text{with } r_l = r_{mb}^{\text{int}}\sqrt{\frac{1}{\phi}} \tag{C.2}$$

$$d_{\text{module}} = \sqrt{\frac{V_{\text{shell}} + V_g + V_m}{\frac{1}{4}\pi L_f}} = 4.2\,\text{cm} \tag{C.3}$$

For all compartments, the width, cross-sectional area and volume are provided in Table C.1. The cross-sectional area is calculated with Equation C.4, while the volumes were calculated with Equations C.5 to C.8. The locations of the interfaces and their surface areas are provided in Table C.2. The surface areas are calculated according to Equation C.9. Figure C.1 schematically displays all locations specified in the equations and tables.

$$A_{c,g} = \tfrac{1}{4}\pi N_f {d_i}^2 \qquad \text{and } A_{c,l} = \frac{V_l}{L_f} \tag{C.4}$$

$$V_g = \tfrac{1}{4}\pi N_f L_f {d_i}^2 \tag{C.5}$$

$$V_m = \tfrac{1}{4}\pi N_f L_f \left((d_i + 2d_m)^2 - {d_i}^2\right) \tag{C.6}$$

$$V_b = \tfrac{1}{4}\pi N_f L_f \left((d_i + 2d_m + 2d_b)^2 - (d_i + 2d_m)^2\right) \tag{C.7}$$

$$V_l = V_{\text{shell}} - V_b \tag{C.8}$$

$$A_{s,k} = \pi L_f N_f \left(2r_k\right) \qquad \text{with } k = \left[{}^{int}_{gm}, {}^{int}_{mb}, {}^{int}_{bl}, l\right] \tag{C.9}$$

$$A_{s,\text{module}} = \pi L_f d_{\text{module}} \tag{C.10}$$

Table C.1: The thickness, cross-sectional area and the volume are provided for all compartments. Values for the cross-sectional area and volume are given with respect to the whole module. Note that for these calculations the thickness of the biofilm d_b was assumed to be 190 µm.

Compartment	Width in geometry[a]	µm	Cross-sectional area	mm^2	Volume	mL
Gas	$\frac{1}{2}d_i$	170	$A_{c,g}$	49.936	V_g	19.974
Membrane	d_m	110	-	-	V_m	34.221
Biofilm	d_b	190	-	-	V_b	98.489
Liquid	d_l	425	$A_{c,l}$	1003.8	V_l	401.51

a) There is an imposed symmetry axis in the gas and liquid phase, so only one of the halves of these compartments are used in the geometry.

Table C.2: The radial position and the surface areas of the interfaces and symmetry axes are tabulated. Note that the thickness of the biofilm d_b was assumed to be 190 µm. Values for the surface areas are given with respect to the whole module.

Axis	Location	Position (µm)	Surface area	m^2
Gas symmetry axis	0	0	-	-
Gas-membrane interface	r_{gm}^{int}	170	$A_{s,gm}^{int}$	0.2350
Membrane-biofilm interface	r_{mb}^{int}	280	$A_{s,mb}^{int}$	0.3870
Biofilm-liquid interface	r_{bl}^{int}	470	$A_{s,bl}^{int}$	0.6497
Liquid symmetry axis	r_l	895	$A_{s,l}$	1.8868

For the whole module, the volume-specific surface area a was calculated by dividing the surface area of the membrane by the total shell volume to be 774 m^{-1}. The outer surface area of the module was calculated to be 0.0528 m^2 (Equation C.10). This value indicates that the fibres cause an increase in surface area of 733% compared to the module outer surface area.

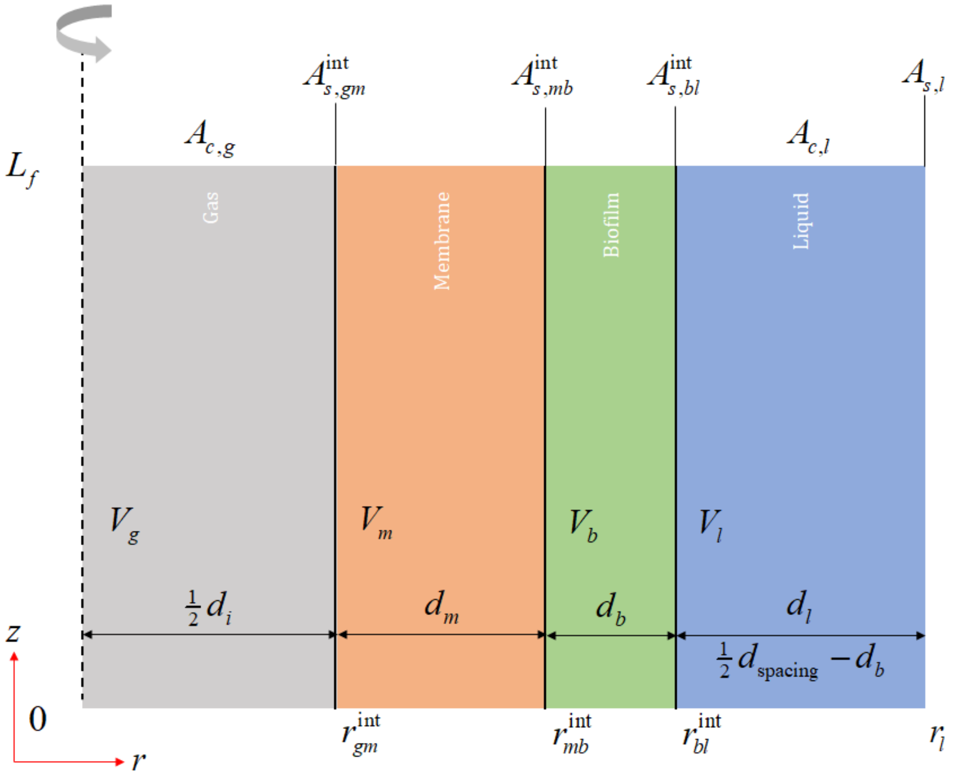

Figure C.1: Schematic representation of the model geometry. The symbols of the membrane specific parameters used are depicted at their location.

D

Model parameter calculations

D.1. Gas parameters

The Reynolds number in the gas phase is calculated using Equations D.1 and D.2. In this formula, the density and viscosity values are valid for the syngas mixture. For density, this is a component-averaged value (Equation D.3), while for gas mixture viscosity an equation was proposed by Wilke (1950) (Equation D.4), which is well-known for its simplicity compared to other gas mixture viscosity theories (such as Reichenberg's) and gives just slightly different results (Reid et al., 1987).

$$v_g = \frac{F_{g,in}}{A_{c,g}} = \frac{400\,\mathrm{mL\,min^{-1}}}{49.936\,\mathrm{mm^2}} = 0.13\,\mathrm{m\,s^{-1}} \tag{D.1}$$

$$Re_g = \frac{\rho_{g,av} v_g d_i}{\eta_{g,av}} = \frac{1.68\,\mathrm{kg m^{-3}} \times 0.13\,\mathrm{m s^{-1}} \times 340 \times 10^{-6}\,\mathrm{m}}{1.1 \times 10^{-5}\,\mathrm{Pas}} \approx 6.7 \tag{D.2}$$

$$\rho_{g,av} = \sum_{i=1}^{n} \left(\rho_{g,i} \times \omega_{g,i}\right) = 1.68\,\mathrm{kg m^{-3}} \tag{D.3}$$

$$\eta_{g,av} = \sum_{i=1}^{n} \frac{\eta_{g,i}}{1 + \frac{1}{x_{g,i}} \sum\limits_{j=1, j\neq i}^{j=n} x_{g,j}\phi_{ij}} = 1.1 \times 10^{-5}\,\mathrm{Pas} \quad \text{with} \quad \phi_{ij} = \frac{\left(1 + \left(\frac{\eta_{g,i}}{\eta_{g.j}}\right)^{1/2} \left(\frac{M_j}{M_i}\right)^{1/4}\right)^2}{\left(\frac{4}{\sqrt{2}}(1 + \frac{M_i}{m_j}\right)^{1/2}} \tag{D.4}$$

The initial composition of the syngas mixture is derived from Munasinghe and Khanal (2010) from the fluidized bed air blown gasification processes, after assuming 100% methane desorption (Table D.1). Densities of all gaseous compounds are calculated using the ideal gas law (Equation D.5), thus assuming an ideal mixture, while viscosities are calculated with Sutherland's formula at $37°C$ (Equation D.6) and values from Table D.1 (Sutherland, 1893).

In cases where only CO was fed, the density and viscosity were calculated with the same procedure and were derived to be $1.63\,\mathrm{kg m^{-3}}$ and $1.822 \times 10^{-5}\,\mathrm{Pas}$, respectively.

$$\rho_{g,i} = \frac{n}{V} M_i = \frac{p_g}{RT} M_i \tag{D.5}$$

$$\eta_{g,i} = \eta_0 \frac{T_0 + C_{S,i}}{T + C_{S,i}} \left(\frac{T}{T_0}\right)^{\frac{3}{2}} \tag{D.6}$$

Table D.1: Values used for several calculations in the gas phase. The producer gas mole fractions as provided by Munasinghe and Khanal (2010) are given and the syngas composition after methane removal. Next to this, the constants used for the calculation of the compound-specific viscosity (Crane, 1999) and the diffusivity values (Seader et al., 2011; Fuller et al., 1966) are provided.

Compound	$x_{g,i,\text{prodgas}}$	$x_{g,i,\text{syngas}}$	C_S (-)	T_0 (K)	η_0 (mPa.s)	$\sum_V$ (-)
CO	0.14	0.1505	118	288.15	0.01720	18.9
CO_2	0.20	0.2151	240	293.15	0.01480	26.9
H_2	0.09	0.968	72	293.85	0.00876	7.07
N_2	0.50	0.5376	111	300.55	0.01781	17.9
H_2O	-	-	-	-	-	13.1
Ethanol	-	-	-	-	-	50.36
CH_4	0.07	-	-	-	-	-

Maxwell-Stefan diffusion coefficients were subsequently calculated. As all compounds in the gas phase are present in the same order of magnitude, diffusion coefficients are calculated relative to the other compounds in the gas phase, according to Equation D.7 and described by Fuller et al. (1966). In this formula, pressure p must be in atm, temperature T in Kelvin, while $M_{i,j}$ is a term for the molar masses of two compounds and Σ_V the molecular diffusion volume (dimensionless).

The calculated Maxwell-Stefan diffusion coefficients (Table D.2) were averaged for each compound based on the gas phase composition. This was done according to Equation D.8. These values all were in the same order of magnitude, around $1 \times 10^{-5}\,\mathrm{m^2\,s^{-1}}$. After evaporation of ethanol and water, it was assumed that these gasses do not influence the viscosity of the gas phase. The molecular diffusion volume of ethanol was calculated based on the atomic diffusion volumes of the individual atoms in ethanol.

$$D_{i,j} = \frac{0.00143\,T^{1.75}}{p M_{i,j}^{1/2} \left(\sum_{V_i}^{1/3} + \sum_{V_j}^{1/3}\right)^2} \quad \text{with} \quad M_{i,j} = \frac{2}{\frac{1}{M_i} + \frac{1}{M_j}} \tag{D.7}$$

$$D_{g,i,av} = \frac{1 - \omega_{g,i}}{\sum_{j=1}^{n} \left(\frac{x_{g,j}}{D_{i,j}}\right)} \approx 10^{-5} \tag{D.8}$$

After calculating these values, the Peclet and Graetz numbers were calculated for CO to estimate whether the flow was convection or diffusion dominated (Equation D.9 and D.10). From this analysis can be said that axial diffusion can be neglected, while radial diffusion dominates.

The pressure drop inside the fibre was calculated with the Darcy-Weisbach pressure drop equation (Brown, 2002), while describing the *fanning* friction factor with $4f = 64/Re$ (Janssen and Warmoeskerken, 2006).

$$Pe_g = \frac{\text{convection}}{\text{axial diffusion}} = \frac{L_f v_g}{D_{i,j}} = \frac{0.4\,\mathrm{m} \times 0.13\,\mathrm{m\,s^{-1}}}{1 \times 10^{-5}\,\mathrm{m^2\,s^{-1}}} \approx 5200 \tag{D.9}$$

$$Gz_g = \frac{\text{convection}}{\text{radial diffusion}} = \frac{d_\mathrm{i}^2 v_g}{L_f D_{g,\mathrm{CO},av}} = \frac{(340\,\mu\mathrm{m})^2 \times 0.13\,\mathrm{m\,s^{-1}}}{0.4\,\mathrm{m} \times 1 \times 10^{-5}\,\mathrm{m^2\,s^{-1}}} \approx 3.7 \times 10^{-3} \tag{D.10}$$

$$p_g\big|_{z=0} = \frac{64}{Re_g} \frac{L_f}{d_i} \frac{1}{2} \rho_g v_g^2 + p_g\big|_{z=L_f} = 0.0016\,\mathrm{bar} + p_g\big|_{z=L_f} \tag{D.11}$$

Table D.2: Maxwell-Stefan diffusion coefficients (in $1 \times 10^{-5}\,\mathrm{m^2\,s^{-1}}$) as calculated by Equation D.7. Temperature and pressure were imposed to be 37 °C and 1.5 bar, respectively. The average diffusion coefficients were only calculated for the syngas mixture.

$D_{i,j}$	CO	CO_2	H_2	N_2	EtOH	H_2O
CO	-	1.18	5.46	1.50	9.29	1.87
CO_2	1.18	-	4.68	1.20	7.38	1.53
H_2	5.46	4.68	-	5.57	3.59	6.38
N_2	1.50	1.20	5.57	-	9.43	1.91
EtOH	9.29	7.38	3.59	9.43	-	1.19
H_2O	1.87	1.53	6.38	1.91	1.19	-
$D_{g,i,av}$	1.5	1.2	6.0	1.6	-	-

D.2. Membrane parameters

Merkel et al. (2000) determined the solubility and diffusivity values of CO_2, H_2 and N_2 in PDMS at 35 °C. As this is close to the operating temperature of 37 °C, these numbers were assumed to be valid at 37 °C. But for intermediate calculations, the temperature of 35 °C was used.

As for solubility the units are given in $\mathrm{m^3_{(STP)}\,m_m^{-3}\,atm^{-1}}$, the gas volume at 1 atm and 25 °C was calculated (Equation D.12). With this value, the units of the solubility were converted with Equation D.13. The gas-membrane partition coefficient can then be calculated by elimination of the pressure term (Equation D.14). The diffusion coefficients were provided in Merkel et al. (2000), and were used to calculate the permeability of these compounds in PDMS (Equation D.15).

$$V_{(STP)} = \frac{RT_{(STP)}}{p_{(STP)}} = \frac{R \times 25\,^{\circ}\mathrm{C}}{1\,\mathrm{atm}} = 0.0245\,\mathrm{m^3_{(STP)}\,mol^{-1}} \tag{D.12}$$

$$c^{sol}_{m,i}\left[\frac{\mathrm{mol}}{\mathrm{m_m^3.atm}}\right] = \frac{c^{sol}_{m,i}\left[\frac{\mathrm{m^3_{(STP)}}}{\mathrm{m_m^3.atm}}\right]}{V_{(STP)}} \tag{D.13}$$

$$K^{mg}_{i} = c^{sol}_{m,i}\left[\frac{\mathrm{mol}}{\mathrm{m_m^3.atm}}\right] R\left[\frac{\mathrm{m_g^3.atm}}{\mathrm{K.mol}}\right] T\,[\mathrm{K}] = c^{sol}_{m,i} R \times 35\,^{\circ}\mathrm{C} \tag{D.14}$$

$$P_i = K^{mg}_{i} \times D_{m,i} \tag{D.15}$$

For CO, the permeability was not stated by Merkel et al. (2000). However, PermSelect® (a membrane producing company) stated the permeability of gasses (including CO) for their PDMS membranes (P^{PS}_{i}) at 25 °C (Montoya, 2010). The temperature difference was taken into account by converting the calculated permeability of N_2 to barrer and compared to the permeability of the PermSelect® membrane. Conversion to barrer was done by converting the permeability units as was proposed by Stern (1968), using Equations D.16 and D.17. The CO permeability was then retrieved by correcting using the calculated nitrogen permeability (Equation D.20). By assuming that the diffusion coefficient in the PDMS membrane of CO equals the one of N_2 (which is justified as CO has the same molecular mass as N_2, and has been proposed before in literature (Robb, 1968)), the solubility of CO in PDMS was calculated. Then the gas-membrane partition coefficient could be calculated using Equation D.14, as well as the permeability in $\mathrm{m^2\,s^{-1}}$ via Equation D.15.

$$P_{N_2} = c^{sol}_{m,N_2}\,[\mathrm{m^3_{(STP)}\,m_m^{-3}\,atm^{-1}}] \times D_{m,N_2}\,[\mathrm{m^2\,s^{-1}}] = 3.06 \times 10^{-10}\,1 \times 10^{-10}\,\frac{\mathrm{m^3_{(STP)}.m}}{\mathrm{m^2.s.cmHg}} \tag{D.16}$$

$$P_{N_2} = P_{N_2}\left[1 \times 10^{-10}\,\frac{\mathrm{cm^3_{(STP)}.cm}}{\mathrm{cm^2.s.cmHg}}\right] = \frac{P_{N_2}\left[\frac{\mathrm{m^3_{(STP)}.m}}{\mathrm{m^2.s.atm}}\right]}{1 \times 10^{-10} \times 1 \times 10^{-4}\,\frac{\mathrm{m^2}}{\mathrm{cm^2}} \times 76\,\frac{\mathrm{cmHg}}{\mathrm{atm}}} = 402.3 \approx 400\,\mathrm{barrer} \tag{D.17}$$

Table D.3: The solubility of all compounds in PDMS, gas-membrane partition coefficients, diffusion coefficients and permeability values for the membrane are tabulated. The solubility, partition and diffusivity values are calculated at 35 °C, while P_i^{PS} is determined at 25 °C. Solubility and diffusion values for CO_2, H_2 and N_2 were derived from Merkel et al. (2000), P_i^{PS} from Montoya (2010) and the values of CO were calculated based on the values of the other gasses.

Compound	$c_{m,i}^{sol}$ ($\mathrm{m^3_{(STP)}\,m_m^{-3}\,atm^{-1}}$)	$K_{m,i}^{mg}$ ($\mathrm{mol.m}_m^{-3}.(\mathrm{mol.m}_g^{-3})^{-1}$)	$D_{m,i}(35°C)$ ($\mathrm{m^2\,s^{-1}}$)	P_i ($\mathrm{m^2\,s^{-1}}$)	P_i^{PS} (barrer)
CO	0.11	0.1122	3.40×10^{-9}	3.82×10^{-10}	340
CO_2	1.29	1.333	2.20×10^{-9}	2.93×10^{-9}	3250
H_2	0.05	0.0517	1.40×10^{-8}	7.23×10^{-10}	650
N_2	0.09	0.930	3.40×10^{-9}	3.16×10^{-10}	280

$$P_{\mathrm{CO}} = P_{\mathrm{CO}}^{PS} \times \frac{P_{\mathrm{N_2}}}{P_{\mathrm{N_2}}^{PS}} = 340 \times \frac{400}{280} = 486\,\mathrm{barrer} \tag{D.18}$$

$$P_{\mathrm{CO}} = P_{\mathrm{CO}}\,[\mathrm{barrer}] \times 76 \times 10^{-14} = 3.69 \times 10^{-10}\,\frac{\mathrm{m^3_{(STP)}.m}}{\mathrm{m^2.s.atm}} \tag{D.19}$$

$$c_{m,\mathrm{CO}}^{sol} = \frac{P_{\mathrm{CO}}\left[\frac{\mathrm{m^3_{(STP)}.m}}{\mathrm{m^2.s.atm}}\right]}{D_{m,\mathrm{CO}}} = 0.109\,\frac{\mathrm{mol}}{\mathrm{m_m^3.atm}} \tag{D.20}$$

Partition values between membrane and liquid were not known so far. Therefore, these values were determined by assuming that there is also an equilibrium between gas and liquid. This gas-liquid equilibrium then determines the partition between the membrane and the liquid. The gas-liquid equilibrium can be described by the Henry coefficient (H_i^{cp}). The Henry constants for the gasses were tabulated in Sander (2015), for a temperature of 25 °C. Temperature dependency was taken into account by correcting the Henry constant using Equation D.21, with $\Delta_{sol}H$ as the dissolution enthalpy (Sander, 2015). The reference values, the dissolution enthalpy. The gas-liquid partition coefficient was calculated by correcting the the temperature-corrected Henry for the gas pressure (Equation D.22). The membrane-liquid partition coefficient was then calculated by dividing the two partition coefficients (Equation D.23). The values of the Henry constants, the temperature dependency terms, and both calculated partition coefficients were provided in Table D.4.

$$H_i^{cp}(T) = H_i^{cp,0} \times \exp\left\{\frac{-\Delta_{sol}H_i}{R}\left(\frac{1}{T} - \frac{1}{T^0}\right)\right\} \tag{D.21}$$

$$K_i^{lg} = H_i^{cp}(T)\left[\frac{\mathrm{mol}}{\mathrm{m_l^3.atm}}\right] R\left[\frac{\mathrm{m_g^3.atm}}{\mathrm{K.mol}}\right] T\,[\mathrm{K}] = H_i(T)R \times 35\,°\mathrm{C} \tag{D.22}$$

$$K_i^{ml} = \frac{K_i^{mg}}{K_i^{lg}} \tag{D.23}$$

Table D.4: The Henry coefficients at 25 °C and its temperature dependency $-\Delta_{sol}H_i.R^{-1}$ were taken from Sander (2015) and tabulated. These values were used for the calculation of the gas-liquid and membrane-liquid partition coefficients at 35 °C .

Compound	$H_i^{cp,0}$ ($\mathrm{mol\,m_l^{-3}\,atm^{-1}}$)	$-\Delta_{sol}H_i.R^{-1}$ (K)	K_i^{lg} ($\mathrm{mol.m}_l^{-3}.(\mathrm{mol.m}_g^{-3})^{-1}$)	K_i^{ml} ($\mathrm{mol.m}_m^{-3}.(\mathrm{mol.m}_l^{-3})^{-1}$)
CO	0.983	1300	2.16×10^{-2}	5.201
CO_2	33.44	2400	0.651	2.048
H_2	0.790	500	1.89×10^{-2}	2.731
N_2	0.648	1600	1.38×10^{-2}	6.752

D.3. Liquid parameters

The viscosity of water at 37 °C was calculated using Equation D.24. Parameters used for water are: $C_{\eta_A} = -24.71$, $C_{\eta_B} = 4.209 \times 10^3$, $C_{\eta_C} = 4.527 \times 10^{-2}$, $C_{\eta_D} = -3.376 \times 10^{-5}$ (Reid et al., 1987). The influence of the other dissolved compounds on the liquid viscosity was neglected. The liquid viscosity was calculated to be 0.708 mPs (Equation D.25), which is 30% lower than the water viscosity at STP (1 mPs).

$$\ln \eta_l = C_{\eta_A} + C_{\eta_B} T^{-1} + C_{\eta_C} T + C_{\eta_D} T^2 = -0.345 \tag{D.24}$$

$$\eta_l = \exp\{\eta_l\} = 7.08 \times 10^{-4}\,\mathrm{Pa\,s} \tag{D.25}$$

$$D_{l,i,0} = \frac{k_B T_0}{6\pi \eta_0 r_{p,i}} \tag{D.26}$$

$$D_{l,i}(T) = D_{l,i,0} \frac{T\eta_0}{T_0 \eta(T)} \tag{D.27}$$

$$r_{p,x} = \sqrt{\frac{0.5}{2}^2 + \frac{3.2}{2}^2} = 1.62\,\mu\mathrm{m} \tag{D.28}$$

$$c_{l,i}^{sol} = K_i^{lg} \frac{p_l}{RT} \tag{D.29}$$

The density of water was found to be equal to 993.36 $\mathrm{kg\,m^{-3}}$ at 37 °C (Janssen and Warmoeskerken, 2006) and assumed not to be affected by the presence of solutes.

Temperature dependence of the diffusion coefficients in the liquid phase was taken into account by using the Stokes-Einstein relationship (Equation D.27). The diffusion coefficients at 25 °C as tabulated in Cussler (2011) used as reference (Table D.5), as well as the water viscosity at 25 °C, which was calculated using Equation D.24. The diffusion coefficients in the biofilm were calculated by multiplying the liquid diffusion coefficient with the assumed biofilm diffusivity factor f_B of 0.8. The biomass diffusion coefficient was calculated according to Equation D.26. As *Clostridium autoethanogenum* is a rod-shaped bacterium with an average width of 0.5 µm and height of 3.2 µm (Abrini et al., 1994), the particle radius was calculated to be the distance from the centre of the rod (a cylinder) to the base-side interface using Pythagoras' theorem (Equation D.28). The diffusion coefficient was then calculated to be $1.98 \times 10^{-13}\,\mathrm{m^2\,s^{-1}}$.

The maximum solubility of the gas species was calculated according to the liquid pressure and the gas-liquid partition coefficient, according to Equation D.29.

After calculation of these parameters, the Reynolds, Peclet and Graetz number (both for CO) were calculated for the liquid flow in order to describe the governing transport phenomena. As the shell liquid flow velocity is variable and these numbers highly depend on the flow velocity, the highest possible flow rate (500 $\mathrm{mL\,min^{-1}}$), was also used for these calculations. The flow velocity was calculated in the module (Equation D.30), which was then used for the calculation of these numbers (Equations D.31, D.32 and D.33). From this analysis was found that the flow will always be in the laminar regime as the Reynolds number is very low. From the high Peclet number can be found that axial diffusion can be neglected in most cases. While the Graetz number was found that the axial convection term was 11 times larger than the radial diffusion term. This indicates that at high flow velocities, radial diffusion could become be a limiting factor for nutrient supply or for liquid mixing.

$$v_l = \frac{F_{l,mod,in}}{A_{c,l}} = \frac{400\,\mathrm{mL\,min^{-1}}}{1004\,\mathrm{mm^2}} = 8.3\,\mathrm{mm\,s^{-1}} \tag{D.30}$$

$$Re_l = \frac{\rho_l v_l 2 d_l}{\eta_l} = \frac{993.6\,\mathrm{kgm^{-3}} \times 8.3\,\mathrm{mm\,s^{-1}} \times 2 \times 495\,\mu\mathrm{m}}{7.1 \times 10^{-4}\,\mathrm{Pas}} \approx 11.5 \tag{D.31}$$

$$Pe_l = \frac{L_f v_l}{D_{l,\mathrm{CO}}} = \frac{0.4\,\mathrm{m} \times 8.3\,\mathrm{mm\,s^{-1}}}{2.71 \times 10^{-9}\,\mathrm{m^2\,s^{-1}}} = 1.22 \times 10^6 \tag{D.32}$$

$$Gz_l = \frac{d^2_{\mathrm{spacing}} v_l}{L_f D_{l,\mathrm{CO}}} = \frac{(0.123\,\mathrm{cm})^2 \times 8.3\,\mathrm{mm\,s^{-1}}}{0.4\,\mathrm{m} \times 2.71 \times 10^{-9}\,\mathrm{m^2\,s^{-1}}} = 11.5 \tag{D.33}$$

Table D.5: Diffusion coefficients of all compounds in water at 25 (obtained from Cussler (2011)) and 37 °C and biofilm and the maximum solubility of these compounds in water in water.

Compound	$D_{l,i,0}$ ($\mathrm{m^2\,s^{-1}}$)	$D_{l,i}(37°C)$ ($\mathrm{m^2\,s^{-1}}$)	$D_{b,i}(37°C)$ ($\mathrm{m^2\,s^{-1}}$)	$c^{sol}_{l,i}$ ($\mathrm{mol\,m^{-3}}$)
CO	2.03×10^{-9}	2.71×10^{-9}	2.17×10^{-9}	0.85
CO_2	1.92×10^{-9}	2.56×10^{-9}	2.05×10^{-9}	25.6
H_2	4.50×10^{-9}	6.01×10^{-9}	4.81×10^{-9}	0.74
N_2	1.88×10^{-9}	2.51×10^{-9}	2.01×10^{-9}	0.54
NH_4^+	1.64×10^{-9}	2.19×10^{-9}	1.75×10^{-9}	-
Ethanol	0.84×10^{-9}	1.21×10^{-9}	0.97×10^{-9}	-
Biomass	-	1.98×10^{-13}	-	-

E

Modelling and impact of evaporation

Evaporation of water and ethanol have been taken into account while modelling the HFM membrane reactor. However, water evaporation was mostly not taken into account due to its predictable behavior (as will be shown later). In this appendix, the calculations used for modelling evaporation of these compounds are discussed.

Ethanol evaporation

The saturation pressure of ethanol can be calculated using a modified Antoine's law (Equation E.1), while the pressure in the gas phase can be calculated using Raoult's law corrected for non-ideal liquids (Equation E.3). The Antoine constants C_{vp} used were taken from Reid et al. (1987), and are -8.51838 (A), 0.34163 (B), -5.73683 (C), 8.23581 (D).

$$\ln\left(\frac{p_{EtOH,sat}}{p_{EtOH,c}}\right) = (1-x_T)^{-1}\left(C_{vp,A,EtOH}x_T + C_{vp,B,EtOH}x_T^{1.5} + C_{vp,C,EtOH}x_T^{3} + C_{vp,D,EtOH}x_T^{8}\right) \tag{E.1}$$

$$\text{with } x_T = 1 - \frac{T}{T_{EtOH,c}} \tag{E.2}$$

$$p_i = p_{i,sat}x_{l,i}\gamma_{l,i} \tag{E.3}$$

Ethanol partition coefficients were calculated based on the calculated saturation pressure (Equation E.1) and the maximum concentration of ethanol in PDMS, $c^{max}_{EtOH,m}$ 1363 mol per m^3 PDMS (Blume et al., 1991). The liquid-gas partition coefficient was calculated as the quotient of the liquid concentration and the gas concentration (Equation E.4)). The activity coefficient will be calculated later, as that value depends on the liquid characteristics, which are location dependent. The partition between the membrane and the gas phases was calculated as a function of the maximum membrane concentration and the gas concentration at 1.5 atm (Equation E.5)). The liquid-membrane partition coefficient can then be calculated from the other two (Equation E.6)).

$$\begin{aligned} K^{lg}_{EtOH} &= \frac{c_{l,EtOH}}{c_{g,EtOH}} = RT\frac{c_{l,EtOH}}{p_{EtOH,sat}x_{l,EtOH}\gamma_{l,EtOH}} = \\ &= RT\frac{c_{l,EtOH}c_{l,H_2O}}{p_{EtOH,sat}c_{l,EtOH}\gamma_{l,EtOH}} = RT\frac{c_{l,H_2O}}{p_{EtOH,sat}\gamma_{l,EtOH}} = \frac{9721}{\gamma_{l,EtOH}} \end{aligned} \tag{E.4}$$

$$K^{mg}_{EtOH} = \frac{c_{m,EtOH}}{c_g} = RT\frac{c_{m,EtOH}}{p_g} = 23.36 \tag{E.5}$$

$$K^{ml}_{EtOH} = \frac{K^{mg}_{EtOH}}{K^{lg}_{EtOH}} = 0.0024\gamma_{l,EtOH} \tag{E.6}$$

The diffusion coefficient in water was derived in the same way as the other liquid diffusion coefficients (Appendix D.3). The diffusion coefficient in the membrane was derived from the permeation value from Blume et al. (1991) (45.000 barrer) and the calculated membrane diffusion coefficient and was calculated to be $1.46 \times 10^{-9}\,\mathrm{m^2\,s^{-1}}$. The diffusion coefficient in the gas phase was calculated based on Equation D.7). The gas diffusion coefficient in Equation E.15 is based on the average diffusion coefficient as function of the molar fractions of the other gaseous compounds.

Water evaporation

The saturation pressure of water was calculated using Antoine's law (Equation E.7). The temperature in this equation must be in degrees Celsius. The Antoine constants C_{vp} used were taken from Rodgers and Hill (1978), and are 5.16262 (A), 1716.984 (B), 232.538 (C). The pressure in the gas phase can be calculated using Raoult's law (Equation E.3).

Partition coefficients were calculated with the similar equations as the ethanol partition coefficient (Equations E.8-E.10), using the sorption value $c_{H_2O,m^{max}}$ of 210 mol water per $\mathrm{m^3}$ PDMS (Blume et al., 1991). Again, the partition values depend on the activity coefficient of water, which is dependent on the ethanol concentration. For the calculation of the liquid-gas partition coefficient, however, was assumed that the molar fraction of water in water $x_{H_2O,l}$ equals 1.

$$p_{H_2O,sat} = 10^{\,C_{vp,A,H2O} - \dfrac{C_{vp,B,H_2O}}{T + C_{vp,C,H_2O}}} = 6284\,\mathrm{Pa} \tag{E.7}$$

$$K^{lg}_{H_2O} = \frac{c_{l,H_2O}}{c_{g,H_2O}} = RT\frac{c_{l,H_2O}}{p_{H_2O,sat}x_{l,H_2O}\gamma_{l,H_2O}} = RT\frac{c_{l,H_2O}}{p_{H_2O,sat}1\gamma_{l,H_2O}} = \frac{22647}{\gamma_{l,H_2O}} \tag{E.8}$$

$$K^{mg}_{H_2O} = \frac{c_{m,H_2O}}{c_g} = RT\frac{c_{m,H_2O}}{p_g} = 3.5925 \tag{E.9}$$

$$K^{ml}_{H_2O} = \frac{K^{mg}_{H_2O}}{K^{lg}_{H_2O}} = 1.58633 \times 10^{-4}\gamma_{l,H_2O} \tag{E.10}$$

The diffusion coefficient in water was derived in the same way as the other liquid diffusion coefficients (Appendix D.3). The diffusion coefficient in the membrane was derived from the permeation value from Blume et al. (1991) (23.000 barrer) and the calculated membrane diffusion coefficient and was calculated to be $4.87 \times 10^{-9}\,\mathrm{m^2\,s^{-1}}$. The diffusion coefficient in the gas phase was calculated based on Equation D.7). The gas diffusion coefficient in Equation E.15 is based on the average diffusion coefficient as function of the molar fractions of the other gaseous compounds.

Non-ideality

Due to the presence of ethanol, the liquid phase is expected to be a non-ideal solution. In those cases, the activity coefficient γ_i of each compound needs to be taken into account while calculating the evaporation rate. For this, it is assumed that the liquid behaves as a binary mixture containing only water and ethanol. Thus, the solutes (CO, CO_2, biomass, ammonia) are expected not to affect the activity of water and ethanol in the mixture. The activity coefficients of ethanol and water are calculated using Van Laar's activity model (Equations E.11 and E.12), with interaction coefficients A_{EtOH,H_2O} and $A_{H_2O,EtOH}$ of 1.6798 and 0.9227, respectively (Perry et al., 1997).

$$\ln\gamma_{EtOH} = A_{EtOH,H_2O}\left(\frac{A_{H_2O,EtOH}x_{H_2O}}{A_{EtOH,H_2O}x_{EtOH} + A_{H_2O,EtOH}x_{H_2O}}\right)^2 \tag{E.11}$$

$$\ln\gamma_{H_2O} = A_{H_2O,EtOH}\left(\frac{A_{EtOH,H_2O}x_{EtOH}}{A_{EtOH,H_2O}x_{EtOH} + A_{H_2O,EtOH}x_{H_2O}}\right)^2 \tag{E.12}$$

Modelling

Transport from the biofilm to the membrane was modelled with a flux at the biofilm-membrane boundary in the biofilm and a concentration boundary condition in the membrane (Equations E.13 and E.14). The flux from the membrane to the gas phase was modelled as boundary condition in the membrane phase (Equation E.15, while a concentration boundary in the gas phase was imposed to account for partition again (Equation E.16). Due to restrictions in the COMSOL *transport of concentrated species* interface, this concentration was converted into a mass fraction at the interface (Equation E.17).

$$J_i^{\text{mb,int}} = -D_{m,i}\frac{dc_{m,i}}{dr} \tag{E.13}$$

$$c_{m,i}^{\text{mb,int}} = c_{b,i}^{mb,int} \times K_i^{ml} \tag{E.14}$$

$$J_i^{\text{gm,int}} = -D_{g,i}\frac{dc_{g,i}}{dr} \tag{E.15}$$

$$c_{g,i}^{\text{gm,int}} = \frac{c_{m,i}^{\text{mg,int}}}{K_i^{mg}} \tag{E.16}$$

$$\omega_{g,i}^{\text{gm,int}} = \frac{c_{g,i}^{\text{mg,int}}M_i}{\rho_g} \tag{E.17}$$

Impact of evaporation

As the incorporation of evaporation into the model increases the computational effort necessary to solve this system, it was determined whether the impact of evaporation was significant. In cases where only little amounts of ethanol or water are evaporated, then evaporation of that compound could be neglected in future studies. The metrics used to determine the impact of evaporation are the molar fraction in the lumen gas outlet (Equation E.18) and the amount evaporated as function of the module inflow rate $Y_{i,MT}$ (Equation E.19). For different values of the module inflow rate, these metrics were calculated (Figure E.1). The module inflow rate was chosen as it was expected that at low module inflow rates, the relative amount that evaporates would be large due to the high liquid residence time inside the module.

From the results (Figure E.1) can be observed that the molar fraction of water in the gas phase is always around 4%, while the molar fraction of ethanol is around 0.3%. Also the mass transfer yield of water is in a considerable order of magnitude (around 1%) at low module inflow rates, while the maximum value for ethanol is just 0.17%. This all indicates that the impact of ethanol evaporation was predicted to be much lower than that one of water. As the amount of ethanol in the gas phase is very low in all conditions, it was decided that ethanol evaporation could be neglected, while water evaporation should be taken into account.

It should be noted that the amount of water in the module outflow was not corrected for water evaporation, although under some circumstances this could be considerable amounts. Next to that, this evaporation model assumes that in all cases there is an established equilibrium (as it was assumed that Raoult's law is valid to describe evaporation) between the gas phase and the concentration in the membrane at the gas-membrane interface. However, it could also be that this equilibrium would not be reached and that the rate of evaporation would therefore be different.

$$x_i = \left. \frac{\int_0^{A_{c,g}} \frac{p_{g,i}}{p_g} \boldsymbol{u_g} \, \mathrm{d}A_{c,g}}{\int_0^{A_{c,g}} \boldsymbol{u_g} \, \mathrm{d}A_{c,g}} \right|_{x=L_f} \tag{E.18}$$

$$Y_{i,MT} = \frac{\left. \int_0^{A_{s,g}} J_{i,g}^{\mathrm{gm,int}} \, \mathrm{d}A_{s,g} \right|_{r=r_{gm}^{\mathrm{int}}}}{\left. \int_0^{A_{c,l}} c_{l,il} \boldsymbol{u_l} \, \mathrm{d}A_{c,l} \right|_{z=0}} \tag{E.19}$$

(E.20)

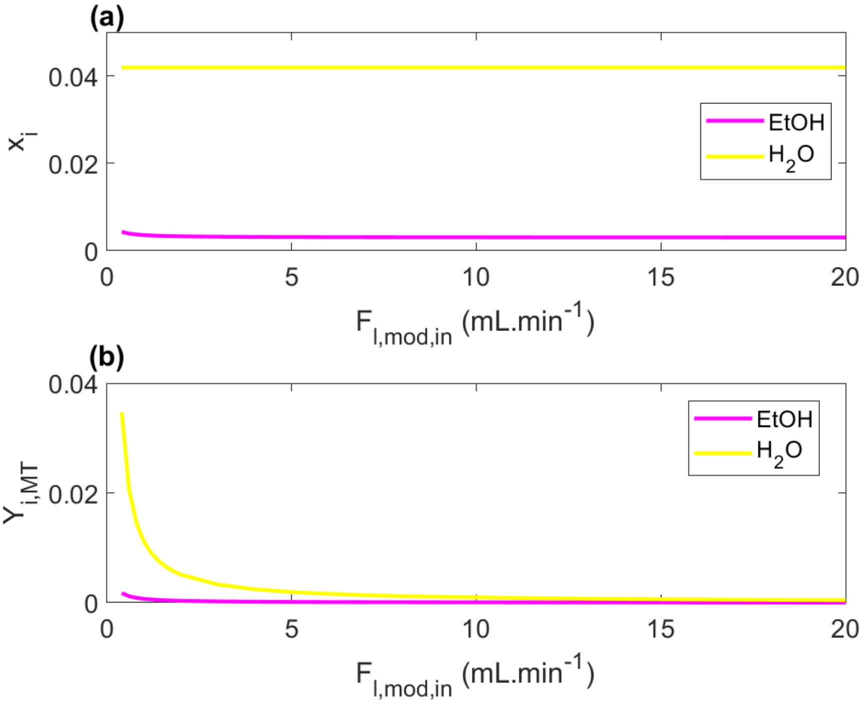

Figure E.1: For different values of the module inflow rate, (a) the mole fraction of ethanol and water in the lumen gas outlet, and (b) the evaporation mass transfer yield $Y_{i,MT}$ are plotted (results from model M_res_Flmodin). The module inflow rate was varied between 0.04 and 20 mL min^{-1}, while the other (reservoir) process parameters were kept constant, as was described in Chapter 6 and Table 6.1.

F

Stoichiometry and kinetics

F.1. Stoichiometry

To describe microbial growth, substrate consumption and product production, a black-box model of the micro-organism has been developed first, based on thermodynamic state analysis (Kleerebezem and Van Loosdrecht, 2010). This enables the derivation of the stoichiometry of catabolic and metabolic reaction of a micro-organism, which was used to model consumption and production. The analysis is based on CO-consumption and ethanol formation.

1. Calculate catabolism reaction by calculating the catabolic electron donor and acceptor reactions:
   Catabolic electron donor reaction (6x): $-1\,CO - 1\,H_2O + 1\,CO_2 + 2\,H^+ + 2\,e^-$
   Catabolic electron acceptor reaction (1x): $-2\,CO_2 - 12\,H^+ - 12\,e^- + 1\,C_2H_5OH + 3\,H_2O$
   Catabolism reaction Y_i^{cat}: $-6\,CO - 3\,H_2O + 1\,C_2H_5OH + 4\,CO_2$

2. Calculate anabolism reaction, using the catabolic electron donor reaction:
   Catabolic electron donor reaction (1.1x): $-1\,CO - 1\,H_2O + 1\,CO_2 + 2\,H^+ + 2\,e^-$
   Anabolic electron acceptor reaction (1x): $-1\,CO - 0.2\,NH_4{}^+ - 2\,H^+ - 2.2\,e^- + 1\,CH_{1.8}O_{0.5}N_{0.2} + 0.5\,H_2O$
   Anabolism reaction Y_i^{an}: $-2.1\,CO - 0.2\,NH_4{}^+ - 0.6\,H_2O + 1\,CH_{1.8}O_{0.5}N_{0.2} + 1.1\,CO_2 + 0.2\,H^+$

3. Calculate catabolic and anabolic free Gibbs energy and enthalpy change for the reactions. The values for $\Delta G^0_{f,i}$ and $\Delta H^0_{f,i}$ were taken from Kleerebezem and Van Loosdrecht (2010).

$$\Delta G^0_{R,cat} = \sum_{i=1}^{n} \Delta G^0_{f,i} \times Y_i^{cat} \qquad \Delta G^0_{R,an} = \sum_{i=1}^{n} \Delta G^0_{f,i} \times Y_i^{an} \tag{F.1}$$

$$\Delta H^0_{R,cat} = \sum_{i=1}^{n} \Delta H^0_{f,i} \times Y_i^{cat} \qquad \Delta H^0_{R,an} = \sum_{i=1}^{n} \Delta H^0_{f,i} \times Y_i^{an} \tag{F.2}$$

4. Calculate the free energy change at 37 °C, using the Gibbs-Helmholtz equation:

$$\Delta G_R^{0T} = \Delta G_R^0 \frac{T}{T_0} + \Delta H_R^0 \frac{T_0 - T}{T_0} \tag{F.3}$$

5. Calculate per reaction the concentration-dependent free energy change, while neglecting the effects of non-ideality (the activity coefficient γ_i of each compound was assumed to be 1):

$$\Delta G_R^{01} = \Delta G_R^{0T} + RT \sum_{i=1}^{n} \left(\ln(c_i) \times Y_{i,R} \right) \tag{F.4}$$

6. Get CO dissipation value from Heijnen and Van Dijken (1992):
   $\Delta G_{CO,met}^{01} = 1105\,\mathrm{kJ\,mol_x^{-1}}$

7. Calculate the catabolism rate λ_{cat}:

$$\lambda_{cat} = \frac{\Delta G_{CO,met}^{01} - \Delta G_{R,an}^{01}}{\Delta G_{R,cat}^{01}} = \frac{-1105 + 26.33}{-147.17} = 7.33 \tag{F.5}$$

8. Calculate metabolism reaction stoichiometry:

$$Y_i^{met} = \lambda_{cat} \times Y_i^{cat} + Y_i^{an} \tag{F.6}$$

The stoichiometry was calculated only for CO consumption and assuming only ethanol production. No H_2 consumption and acetate production were taken into account, as it is known that *C. autoethanogenum* is capable of producing ethanol without consuming H_2 (Xu et al., 2017; Chen et al., 2018). It is also known that LanzaTech is able to produce low amounts of acetate, so that acetate formation was neglected (Abubackar et al., 2011). Using these assumptions, H_2 and acetate were not incorporated in the stoichiometry. If it is known in what ratios H_2 and CO are consumed, and ethanol and acetate are produced, the black box model can be altered in the following ways to take H_2 consumption and acetate production into account:

9. Incorporate acetate in the stoichiometry:

   Calculate its acceptor reaction in catabolism: $-2\,CO_2 - 8\,H^+ - 8\,e^- + 1\,CH_3COOH + 2\,H_2O$

   Calculate total acceptor reaction:

$$Y_i^{acc} = Y_i^{acc,ace} + Y_{eth/ace} \times \frac{Y_i^{acc,ace}}{Y_{ace}^{acc,ace}} \tag{F.7}$$

10. Incorporate hydrogen in the stoichiometry:

    Calculate its donor reaction in catabolism: $-1\,H_2 + 2\,H^+ + 2\,e^-$

    Calculate total acceptor reaction:

$$Y_i^{don} = Y_i^{don,CO} + Y_{H2/CO} \times \frac{Y_i^{don,H2}}{Y_{CO}^{don,CO}} \tag{F.8}$$

F.2. CO-uptake kinetics

Reaction kinetics were derived from literature for different studies (Table F.1). It was chosen to use the kinetics derived by Mohammadi et al. (2014) as their model is the most representative compared to the other models and as it does not exclude maintenance. The maintenance requirement was calculated first and then with a CO uptake model, the consumption or production rate of the other metabolic reactions could be found using the Herbert-Pirt relation.

Table F.1: Comparison of kinetic data of CO-consuming *Clostridium* spp. found in literature

Study^a	μ_{max} (h^{-1})	q_{CO}^{max} ($mol_{CO}\,g_x^{-1}\,h^{-1}$)	$K_{p,CO}$ ($mol_{CO}\,m^{-3}$)	$K_{I,CO}$ ($mol_{CO}\,m^{-3}$)	Organism
[1]	-	0.0344	0.0178	0.510	*C. ljungdahlii*
[2]	0.022	-	0.078	2.0	*C. ljungdahlii*
[3]	-	0.0500	0.1	5	*C. autoethanogenum*
[4]a	-	0.0463	0.0115	0.136	*C. ljungdahlii*
[4]b	-	0.0375	0.0454	0.827	*C.* strain P11

a) [1]: Mohammadi et al. (2014), [2]: Younesi et al. (2005), [3]: Li and Henson (2019), [4]: Medeiros et al. (2019), a: cases C1 and C2, b: cases C3A,B,C.

11. Calculate the maintenance requirement at 37 °C, for anaerobic micro-organisms. The maintenance requirement depends on the temperature with an Arrhenius-type equation, with an activation energy of 69.4 kJ/mol, with a maintenance requirement of 3.3 $kJ\,mol^{-1}$ at 25 °C (Tijhuis et al., 1993):

$$\Delta G_{ms}^{0T} = 3.3 \times \exp\left(\frac{-69.4}{R}\left(\frac{1}{T} - \frac{1}{T_0}\right)\right) = 9.75\,kJ\,mol^{-1} \tag{F.9}$$

12. Calculate the maintenance flux v_{ms}:

$$v_{ms} = \frac{\Delta G_{ms}^{0T}}{\Delta G_{R,cat}^{0T}} = \frac{9.75}{-147.17} = -0.066\,mol_s\,{mol_x}^{-1}\,h^{-1} \tag{F.10}$$

13. Implement kinetic model for CO consumption from Mohammadi et al. (2014):

$$-q_{CO} = -q_{CO}^{max}\frac{c_{CO}}{K_{p,CO} + c_{CO} + \frac{c_{CO}^2}{K_{I,CO}}} \tag{F.11}$$

14. Correct maintenance flux for low CO concentrations:

$$v_{ms} = \begin{cases} q_{CO} & \text{when } q_{CO} < v_{ms} \\ v_{ms} & \text{when } q_{CO} > v_{ms} \end{cases} \tag{F.12}$$

15. Calculate growth rate, due to maintenance correction μ can be zero at low concentrations:

$$\mu = \frac{q_{CO} - v_{ms}}{Y_{CO}^{met}} \tag{F.13}$$

16. Calculate compound specific rates q_i using the Herbert-Pirt relation:

$$q_i = Y_i^{met}\mu + \frac{v_{ms}Y_{CO}^{cat}}{Y_i^{cat}} \tag{F.14}$$

The stoichiometries depend on the concentrations of the compounds present (Equation F.4). Base values for all compounds were determined as follows: for CO, CO_2 and H_2, the concentrations in the liquid at 1 atm: 0.85 $mol\,m^{-3}$, 25.7 $mol\,m^{-3}$ and 0.79 $mol\,m^{-3}$, respectively. For acetate and ethanol, the highest titers obtained by Valgepea et al. (2018) were used, 4 and 11.5 $g\,L^{-1}$ respectively. The amount of ammonium was determined by the medium used by Mohammadi et al. (2014): 1 $g\,L^{-1}$ NH_4Cl. The biomass concentration was set at 15 $g\,L^{-1}$ and the water concentration 55 $mol\,L^{-1}$.

A sensitivity analysis has been done to calculate the influence of the concentrations of these compounds on $\Delta G_{R,cat}^{0T}$ and Y_{CO}^{met} (Figures F.1a and b). Only the catabolic reactants were found to be relevant, as the

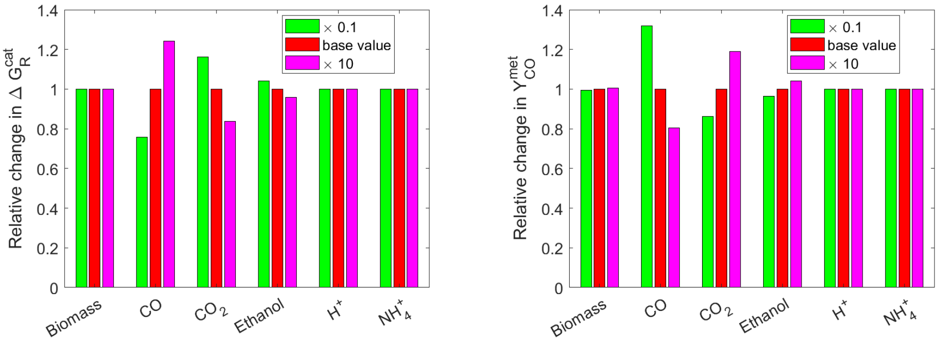

(a)

(b)

Figure F.1: Results of the sensitivity analysis on the concentrations of compounds for calculating the stoichiometry of the organism. The base value for concentrations (Table F.2) has been increased with a factor 0.1 and 10 and its effects on (a) $\Delta G_{R,cat}^{0T}$ and (b) Y_{CO}^{met} were found and tabulated as the relative change compared to the base value.

Table F.2: Key parameters used in calculations for the stoichiometry and reaction rates

	$\Delta H_{f,i}^0$ (kJ.mol^{-1})	$\Delta G_{f,i}^0$ (kJ.mol^{-1})	Concentration (mol.L^{-1})	Y_i^{cat} (mol$_i$.mol$_{eth}^{-1}$)	Y_i^{an} (mol$_i$.mol$_x^{-1}$)	Y_i^{met} (mol$_i$.mol$_x^{-1}$)	$v_{ms,i}$ (mol$_i$.mol$_x^{-1}$.h^{-1})
CO	-110.5	-137.2	0.000085	-6	-2.1	-46.060	-0.06622
CO_2	-394.1	-394.4	0.025750	4	1.1	30.407	0.044146
H_2	0	0	0.000790	0	0	0	0
CH_3COO^-	-485.8.4	-369.4	0.066667	0	0	0	0
C_2H_5OH	-288.3	-181.8	0.250000	1	0	7.327	0.011036
$NH_4{}^+$	-133.3	-79.4	0.020000	0	-0.2	-0.2	0
$CH_{1.8}O_{0.5}N_{0.2}$	-91	-67	0.609756	0	1	1.000	0
H_2O	-285.8	-237.2	55.55556	-3	-0.6	-22.580	-0.03311
H^+	0	0	1E-7	0	0.2	0.2	0
e^-	0	0	1.000000	0	0	0	0
ΔH_R^{0T} (kJ.mol^{-1})	-	-	-	-344.30	-94.32	-2616.88	-
ΔG_R^0 (kJ.mol^{-1})	-	-	-	-224.60	-54.52	-1700.76	-
ΔH_R^{0T} (kJ.mol^{-1})	-	-	-	-219.78	-52.92	-1663.84	-
ΔG_R^{01} (kJ.mol^{-1})	-	-	-	-147.22	-26.33	-1105.00	-

Gibbs free energy of metabolism is constant and the metabolic yield is normalized to the anabolic reaction. The concentration differences in CO cause significant changes on $\Delta G_{R,cat}^{0T}$ and Y_{CO}^{met}, while the concentration of CO_2 and ethanol were found to be less sensitive. Therefore, a more detailed sensitivity analysis was done to find a valid value for the CO concentration for further calculations.

In Figure F.2a, the relations between the CO concentration and $\Delta G_{R,cat}^{0T}$ and Y_{CO}^{met} are given. It can be observed that at lower CO concentrations, the Gibbs free energy difference of the catabolism becomes smaller. This causes the need for more catabolic reactions to provide the energy necessary for growth, which in turn leads to more CO consumption per mol biomass made. It has been chosen to calculate the used stoichiometry with a CO concentration of $0.08\,\mathrm{mol\,m^{-3}}$, which corresponds to a gas pressure of 0.1 atm. This value has been used as the influence of a little change in concentration does not lead to a large change in Y_{CO}^{met}, and as this is a reasonable concentration, which is expected to occur in the biofilm. Key values used for calculations and results are given in Table F.2.

The CO-uptake and growth rate were subsequently calculated. The CO-uptake rate was calculated according to the Monod equation obtained by Mohammadi et al. (2014) (Equation F.11. The growth rate depends on the metabolism stoichiometry and could be calculated after derivation of the total stoichiometry (Equation F.13). From the calculated growth rate and CO-uptake rates can be derived that the optimum of both is at a CO concentration of $0.09\,\mathrm{mol\,m^{-3}}$ (Figure F.2). At increasing concentrations, CO becomes inhibitory.

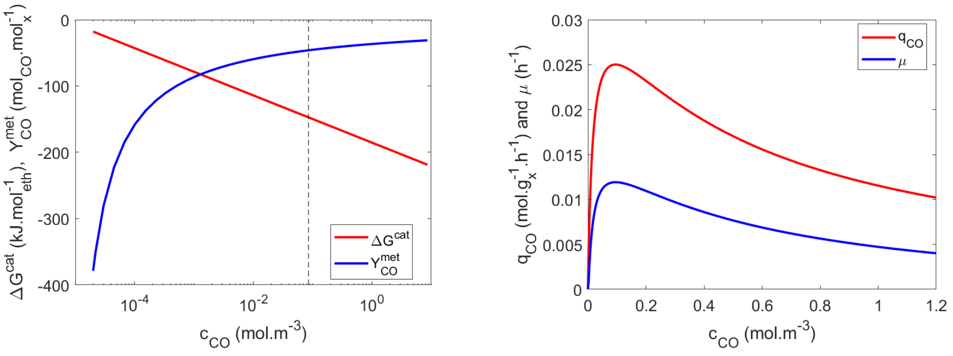

(a)

(b)

Figure F.2: (a) The catabolic Gibbs free energy and the metabolism CO stoichiometry per mol biomass (B) and the specific CO uptake rate and organism growth rate are calculated for different concentrations of CO. For a concentration of 0.08 mol m^{-3}, it has been chosen to use the obtained resulting stoichiometric values for further calculations. The specific growth and CO uptake rate were not fixed at this concentration, but are concentration-dependent in the model.

F.3. Ethanol inhibition

The kinetic model derived above has been updated by taking ethanol inhibition into account, while modelling the reservoir as this could lead to higher amounts of ethanol in the HFM module. It has been known that high ethanol concentrations can be toxic for *Clostridium* spp. Although the exact mechanism is not known, it was assumed that ethanol toxicity leads to a decrease in the CO-specific uptake rate (de Medeiros et al., 2019). This makes it able to model inhibition by adding an extra term to the CO-uptake rate relation (Equation F.11).

Several scholars investigated the impact of ethanol on the growth of *Clostridium* spp. Fernández-Naveira et al. (2016) investigated the ethanol toxicity on CO fermenting *C. carboxidivorans*. They found decreasing values for the growth rate at increased ethanol concentrations. They observed a 50% reduction in growth at a concentration of 35 $\mathrm{g_{EtOH}\,L^{-1}}$ and a 74% decrease in growth rate (compared to 1 $\mathrm{g\,L^{-1}}$). Huffer et al. (2011) examined the effect of different ethanol concentrations on the growth rate of *C. beijerinckii*. They reported that growth was still possible at high ethanol concentrations up to 65 $\mathrm{g_{EtOH}\,L^{-1}}$ on iso-butanol.

Ramió-Pujol et al. (2018) tried to examine the kinetics of ethanol inhibition on syngas fermenting organisms, they performed experiments and tried to fit the data obtained by their experiments and the experiment of Fernández-Naveira et al. (2016). However, they were not able to find a maximum ethanol concentration and their fit (a logistic inhibition curve) showed large standard errors (around 50%). Modelling the equation they obtained (Equation F.15) for the experiment of Fernández-Naviera showed that the ethanol inhibition already started at low concentrations (Figure F.3). Other experiments of Ramió-Pujol et al. (2018) showed no inhibitory effects in the range they sampled up to 15 $\mathrm{g_{EtOH}\,L^{-1}}$.

$$I_{EtOH} = \left(1 - \frac{c_{EtOH}}{c_{EtOH,\max}}\right)^{n} = \left(1 - \frac{c_{EtOH}}{35\,\mathrm{g^{-1}}}\right)^{0.926} \tag{F.15}$$

$$I_{EtOH} = \begin{cases} 1 & \text{when } c_{EtOH} < 761\,\mathrm{mol\,m^{-3}} \\ \frac{1}{1+\frac{c_{EtOH}}{K_{I,EtOH}}} & \text{when } c_{EtOH} > 761\,\mathrm{mol\,m^{-3}}, \quad K_{I,EtOH} = 217\,\mathrm{mol\,m^{-3}} \end{cases} \tag{F.16}$$

Next to this, de Medeiros et al. (2019) tried to fit data obtained by Phillips et al. (1993) to find an inhibition constant. They took inhibition of ethanol into account from a concentration of 35 $\mathrm{g\,L^{-1}}$ (761 $\mathrm{mol\,m^{-3}}$) and derived an inhibition constant of 10 $\mathrm{g\,L^{-1}}$ (217 $\mathrm{mol_{EtOH}\,m^{-3}}$), with a 95% confidence interval of 0.039 $\mathrm{mol_{EtOH}\,L^{-1}}$. In order to increase computational efficiency, Equation F.16 has been approximated using a logistic function

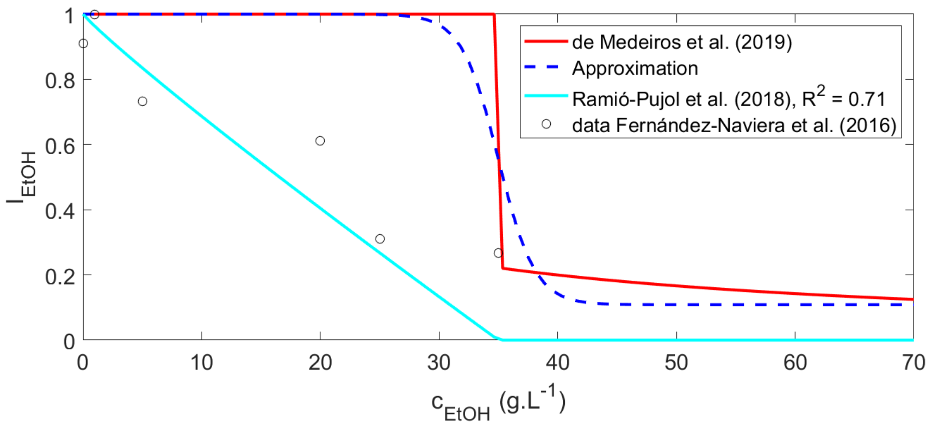

Figure F.3: For different dissolved ethanol concentrations the inhibition-terms used in the CO-uptake rate relation are calculated. The model of de Medeiros et al. (2019) (Equation F.16) is provided and the approximation used for modelling (Equation F.17). The model provided by Ramió-Pujol et al. (2018) (Equation F.15) is given as well as the data they used to fit the model, with the calculated R^2.

(Equation F.17). In the latter function, the value of 30 indicates the slope of the curve and was manually determined. With this function, a continuous curve was made so that the inhibition constant could be calculated for all concentration values. It has been modelled in COMSOL Multiphysics with a *step* function: the maximum concentration of ethanol, 35 $\mathrm{g\,L^{-1}}$ (761 $\mathrm{g_{EtOH}\,L^{-1}}$), was chosen as the center location, for the decreasing from 1 to $\frac{1}{2}K_{I,eth}$, with a transition zone of 20 $\mathrm{mol_{EtOH}\,m^{-3}}$.

In Figure F.3, the inhibition models derived from literature are depicted and compared. From this can be said that these models are not consistent, implying that further research on ethanol inhibition is necessary.

$$I_{EtOH} = 1 - \frac{1-\frac{1}{2}K_{I,eth}}{1+\exp\left(30(c_{EtOH,\max}-c_{EtOH,l})\right)} \tag{F.17}$$

The data obtained by Fernández-Naveira et al. (2016) was fitted with several inhibition functions, based on equation F.18 (Figure F.4). The ethanol inhibition constant was set to be 45 $\mathrm{g_{EtOH}\,L^{-1}}$ (978 $\mathrm{mol\,m^{-3}}$) and the exponent n was varied. With an exponent above 1, the function is non-linear and can describe the growth at lower concentrations as non-inhibitory. Next to this, this way also a linear inhibition function is derived. Linear inhibitory effects of ethanol (and other alcohols) is known in many organisms and is easy to explain and to derive from experimental data (Dagley and Hinshelwood, 1938; Pereira et al., 2016). The quality of the fit was described with the coefficient of determination R^2, which was calculated according to equation F.19. This coefficient was also calculated for the fit obtained by Ramió-Pujol et al. (2018).

$$I_{EtOH} = \begin{cases} 1-\left(\frac{c_{EtOH}}{K_{I,EtOH}}\right)^n & \text{when } c_{EtOH} < 978\,\mathrm{mol\,m^{-3}}, \quad K_{I,EtOH} = 978\,\mathrm{mol\,m^{-3}} \\ 0 & \text{when } c_{EtOH} > 978\,\mathrm{mol\,m^{-3}} \end{cases} \tag{F.18}$$

$$R^2 = 1 - \frac{\sum_{k=1}^{n}\left(y_k - f_k\right)^2}{\sum_{k=1}^{n}\left(y_k - \bar{y}_k\right)^2} \tag{F.19}$$

From the developed inhibition functions and the calculated R^2 values, it was found that the linear fit was better than the fit of Ramió-Pujol et al. (2018) (R^2 = 0.88 vs. 0.71, respectively). The functions with a higher exponent had a lower R^2 value, but are able to take non-inhibition at lower ethanol concentrations into account. From these analysis became clear that there are no proper functions to describe ethanol inhibition and that matches all experimental data. Therefore, the influence of the different inhibition functions on the

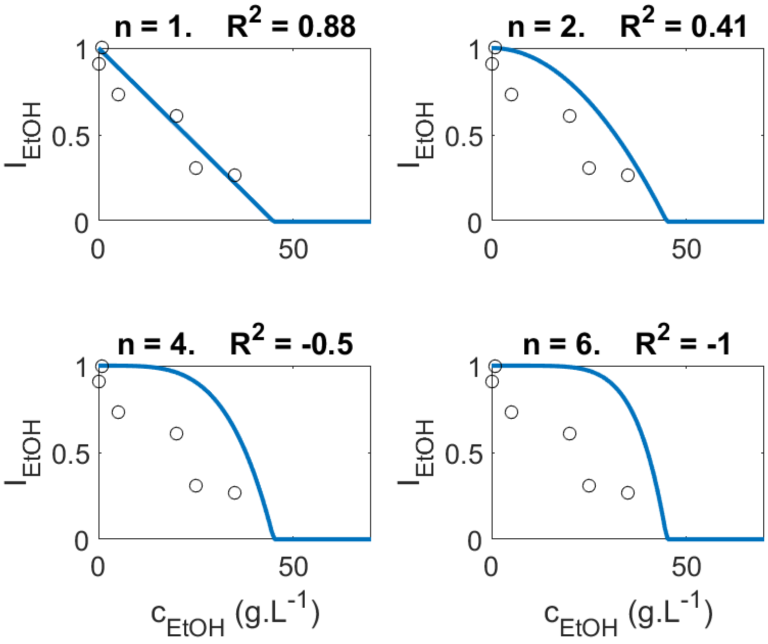

Figure F.4: For different values of n, the data derived by Fernández-Naveira et al. (2016) (plotted in circles) was fitted with Equation F.18 (blue lines). The coefficient of determination was calculated (Equation F.19) to determine the quality of the fit.

ethanol productivity and titer in the reservoir model was simulated for different values of the reservoir inflow rate, as this appeared to be the parameter which influenced the ethanol titer and productivity the most (Chapter 6).

The model of de Medeiros et al. (2019), the linear model ($n = 1$) and the model with $n = 6$ were assessed this way (Figure F.5). The reservoir flow rate was varied between 0.025 and 2 $\mathrm{mL\,min^{-1}}$. The other parameters were kept constant as explained in Chapter 6. The $n = 6$ model and the one of de Medeiros et al. (2019) did not show substantial deviations in productivity at lower flow rates, except that the model of de Medeiros et al. (2019) has a sharp change in titer when the concentration has reached 35 $\mathrm{g_{EtOH}\,L^{-1}}$. The concentrations in the $n = 6$ model increased with the same trend at decreasing flow rates up to 45 $\mathrm{g_{EtOH}\,L^{-1}}$. This can be explained as the simulations of both models reached high amounts of inhibition at mentioned concentrations.

The linear model leads to lower productivities and concentrations than the other models, but with similar trends. However, at higher reservoir flow rates, the productivities and titers do not show much deviations. At low flow rates, the differences are larger. For example, when the flow rate is 0.2 $\mathrm{mL\,min^{-1}}$, the productivity difference is 0.1 $\mathrm{g_{EtOH}\,L_{shell}^{-1}\,h^{-1}}$ and when the flow rate is 0.13 $\mathrm{mL\,min^{-1}}$ even 0.17 $\mathrm{g_{EtOH}\,L_{shell}^{-1}\,h^{-1}}$. As in the linear model inhibition is taken into account at lower ethanol concentrations, the productivity in the system decreases in cases where in the other models no or less inhibition was observed. The differences in ethanol productivity are substantial and emphasize the need for more research into ethanol inhibition of syngas fermenting *Clostridium* spp.

It has been decided to use the linear model for follow-up studies. This model is easy to use and to derive. The kinetics of the microorganism were then modelled according to Equation F.20. For different CO and ethanol concentrations, the values of $I_{CO} \times I_{EtOH}$ are plotted (Figure F.6). The inhibitory effect of ethanol is larger that the inhibitory effect of CO: The decrease in uptake due to a small concentration increase ($\frac{dq_{CO}}{dc_i}$) for ethanol is much larger for CO.

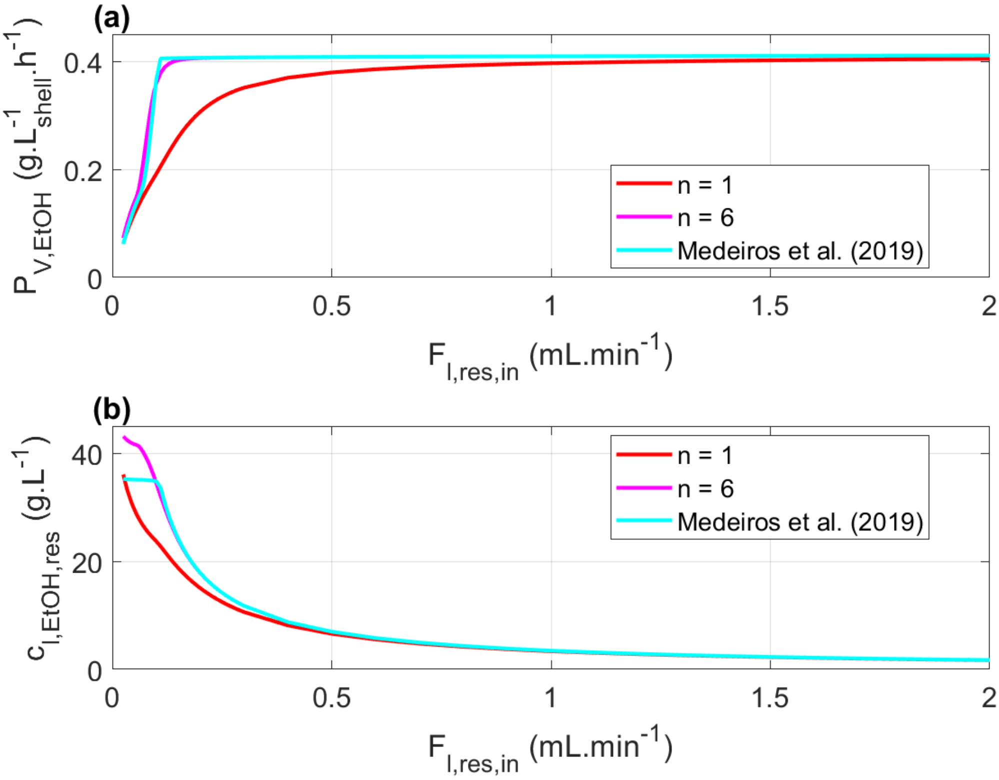

Figure F.5: For different reservoir inlet flow rates and different ethanol inhibition functions, (a) the shell volume-specific productivity in the biofilm and (b) the ethanol concentrations are plotted. The $n = 1$ and $n = 6$ inhibition functions are derived from Equation F.18, while Equation F.17 was used to model the inhibition function derived by de Medeiros et al. (2019) (M_res_Flres_Inhib).

$$-q_{CO} = -q_{CO}^{\max} I_{CO} I_{EtOH} = -q_{CO}^{\max} \frac{c_{CO}}{K_{p,CO} + c_{CO} + \frac{c_{CO}^2}{K_{I,CO}}} \left(1 - \frac{c_{EtOH}}{K_{I,EtOH}}\right) \tag{F.20}$$

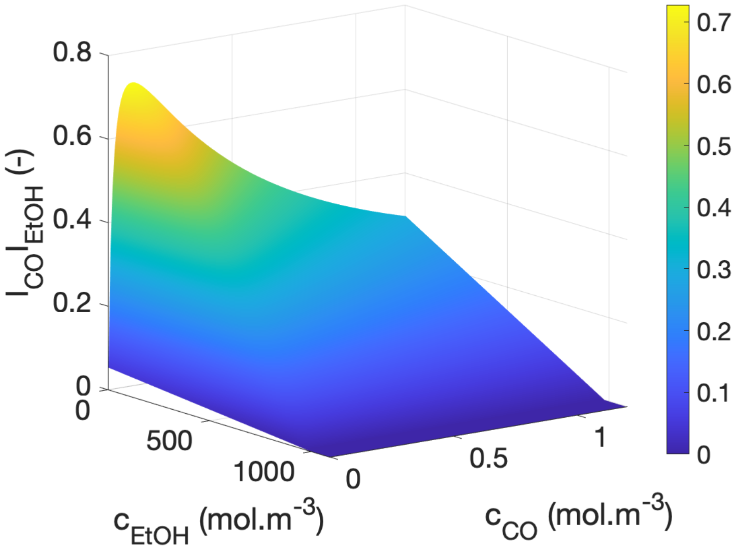

Figure F.6: The product of the two inhibition constants $I_{CO}I_{EtOH}$ was calculated for different concentrations of dissolved CO and EtOH using Equation F.20.

G

Biofilm growth and detachment

Two models have been developed to describe biofilm growth and detachment. One detachment model is based on shear stress, while the other is based on substrate limitation. These models can be used to predict the biofilm thickness in a HFM reactor and thus for designing the spacing in HFM reactor modules.

Theory

The thickness of the biofilm is the result of the biofilm growth rate and the biofilm detachment rate. In order to estimate the biofilm thickness, the biofilm length is calculated based on certain conditions. The net biofilm velocity u_b is the growth velocity $u_{b,g}$ minus the detachment velocity $u_{b,d}$. At steady-state conditions, the net biofilm velocity is zero so that the biofilm length can be regarded constant.

The biofilm growth velocity $u_{b,g}$ can be described by the growth rate of the organism in the biofilm. When an organism duplicates, a part of the biofilm is pushed away from the membrane interface (or substratum) in the direction of the liquid phase. This pushing leads to an overall grow velocity which can be described by Equation G.1. The growth velocity can therefore be calculated by integrating the specific growth rate from the membrane-biofilm interface r_{mb}^{int} to the biofilm-liquid interface r_{bl}^{int}. This model is widely used to describe biofilm growth (Horn and Lackner, 2014), even in membrane-biofilm applications (Pavasant et al., 1996).

Biofilm detachment can be caused by four physical processes: erosion, sloughing, abrasion and predator grazing (Bryers, 1987). Erosion can be described as a constant detachment process of small particles caused by shear stress. In contrast, sloughing is detachment due to removal of larger particles due to rapidly changing environmental conditions. Abrasion is the collision of solid particles with biofilm, while predator grazing is destruction of biofilms by larger organisms (Peyton and Characklis, 1993). In membrane configurations, the most frequent occurring process is erosion as the environmental conditions are more or less constant and as large solid particles (except possible detached biofilm chunks) and predators are not expected to be present (Pavasant et al., 1996). In this chapter, two detachment models are compared, the first is based on detachment by shear stress and the other by substrate limitation.

$$u_{b,g} = \int_{r_{mb}^{\text{int}}}^{r_{bl}^{\text{int}}} \mu \, \mathrm{d}r \tag{G.1}$$

A model commonly used to describe biofilm detachment caused by shear stress is the model from Rittman (1982). Their model is based on a biofilm attached to a rotor and for different levels of shear stress the detachment rate was measured. Pavasant et al. (1996) and Freitas Dos Santos et al. (1997) used that model to describe detachment of biofilms from membranes in wastewater treatment.

The shear stress σ can be described as the derivative of the liquid flow velocity in the radial direction (Equation G.2). Following the model of Rittman (1982), the detachment rate is a function of a detachment constant and the biofilm thickness, the detachment constant is a function of a biomass-specific decay rate, the biofilm thickness, the shear stress and several constants (Equation G.3). All these constants (Table G.1) are dependent on the biofilm and the physio-chemical environment. As the environmental conditions are not the comparable, the results obtained by this model are highly dependent on the assumption that the model of Rittman (1982) can be used.

$$\sigma = \eta_l \frac{\mathrm{d}\boldsymbol{u_l}}{\mathrm{d}r} \tag{G.2}$$

$$u_{d,shear} = k_d d_b \text{ with } k_d = k_{decay} + k_{d1}\left(\frac{\sigma}{k_{d2} + k_{d3}(d_b - d_{b,min})}\right)^{0.58} \tag{G.3}$$

Another model to describe biofilm detachment is the model used by Matsumoto et al. (2007) based on a maximum biofilm thickness. They and Martin et al. (2015) used this model in membrane-biofilm applications. This model is based on the assumption that at a certain biofilm thickness the biofilm detaches, so that in the end a fixed biofilm thickness is reached. This maximum biofilm is often imposed, but here it was calculated based on the maximum amount of substrate that is available. When there is no substrate (CO) available anymore, the biofilm cannot grow and detachment could occur. In reality, non-growing cells could also remain in the biofilm matrix and detachment could then occur due to other physio-chemical processes.

The maximum biofilm length is calculated by assuming that at this location in the biofilm, the characteristic time of reaction and biofilm diffusion (Appendix B) should be the same. After solving Equation G.4 for the maximum biofilm thickness, it can be used to calculate the biofilm detachment velocity as a function of the biofilm growth rate (Equation G.5).

$$\tau_{\text{reac}} = \tau_{\text{diff,rad},b} = \frac{K_{p,CO} + c_{CO,b} + \frac{c_{CO,b}}{K_{I,CO}}}{q_{CO,\text{max}} c_x} = \frac{d_{b,\text{max}}^2}{D_{b,CO}} \tag{G.4}$$

$$u_{d,\text{CO, lim}} = u_g \left(\frac{d_b}{d_{b,\text{max}}}\right)^{10} \tag{G.5}$$

Mind that this detachment model definitely leads to a certain biofilm thickness, as it is an imposed part of the model. This model is also highly dependent on the assumptions made: diffusion is limiting, the diffusion coefficient is assumed (with the imposed biomass diffusivity factor), the reaction kinetics are assumed as well as the biomass concentration. One should also note that these variables can influence each other in reality. For example, Kwok et al. (1998) found that the biomass concentration in the biofilm increases when the detachment rate increases.

The biofilm growth velocity and detachment velocity have been calculated for different biofilm thicknesses using model (M_biof_dbiof). The biofilm thickness was varied between 10 and 300 μm, with $c_{b,x} = 15\,\mathrm{g_x L^{-1}}$. This way, it can be determined whether these models could be useful and whether the assumption of a certain biofilm thickness is valid. As the growth and detachment velocities are location-specific, the average velocities at the biofilm-liquid boundary were calculated.

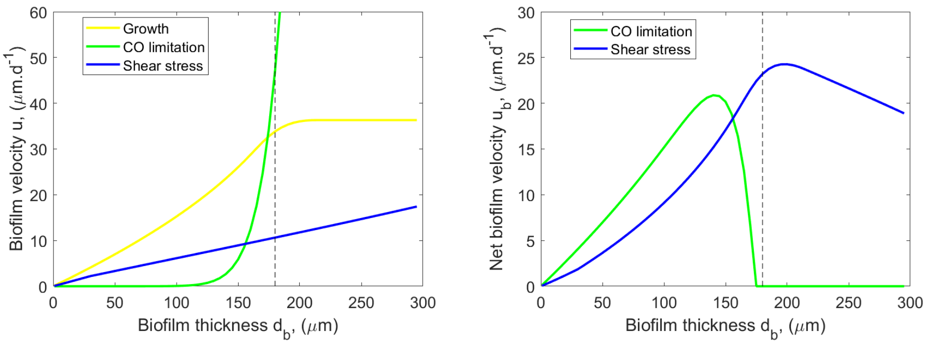

(a)

(b)

Figure G.1: For different values of the biofilm thickness, (a) the growth and detachment velocities were calculated using the shear stress and the CO limitation models as well as (b) the net growth velocity according to both models. The dashed line depicts the optimum biofilm thickness in terms of volume-specific productivity.

Results

For different biofilm thicknesses the corresponding biofilm growth velocity and detachment velocities based on the shear stress and the substrate limitation model are calculated (Figure G.1a). For both detachment models, the net velocity is calculated as well (Figure G.1b).

The biofilm growth velocity increases when the biofilm becomes thicker, which is due to the presence of more biomass that is able to grow. However, at a certain thickness $d_b = 180\,\mu\text{m}$, the growth velocity becomes lower. This is due to the fact that there will be biomass present that will not be able to grow anymore. From this point on, substrate diffusion became limiting (Figure G.1b).

From these results can be observed that detachment due to shear stress gradually increases when the biofilm becomes thicker. This can be explained by the fixed spacing in the liquid phase: For all cases the total liquid flow rate was kept constant at $200\,\text{mL}\,\text{min}^{-1}$, this means that at thicker biofilms the distance between two biofilms is smaller, which would lead to an increase in the radial gradient of the liquid velocity and thus an increase in the liquid shear stress. Remarkable is that the shear stress model gives results that will never lead to detachment of thick biofilms as their net velocity remains positive.

However, the substrate limitation model does provide clarity for thick biofilms. This biofilm detachment model describes detachment of the biofilm and the biofilm length will be maintained at the maximum biofilm thickness (which was calculated to be 174 μm). When the biofilm is thicker, detachment would occur rapidly as this is imposed in the model. As the detachment is modelled with an exponential factor of 10, the increase in detachment velocity is large at thicker biofilms.

From this analysis can be said that biofilm detachment could be modelled with the help of these functions, however their results are very dependent on the assumptions made and therefore it can be questioned whether these results are representative for reality and therefore the usefulness of these models.

Table G.1: Parameters used for calculation of detachment. The values of the process parameters used are provided as well as the constants used for Equation G.2. Other characteristics of the model are similar to the biofilm model described in Chapter 5 (M_biof_cx).

Symbol	Value	Unit	Symbol	Value	Unit	Reference
$F_{g,in}$	20	$\text{mL}\,\text{min}^{-1}$	k_{decay}	0.05	d^{-1}	Assumed
$x_{g,CO,in}$	100	%	k_{d1}	8.42×10^{-2}	d^{-1}	Rittman (1982)
$F_{l,mod,in}$	200	$\text{mL}\,\text{min}^{-1}$	k_{d2}	0.1	$\text{N}\,\text{m}^{-2}$	Rittman (1982)
$c_{b,x}$	15	$\text{kg}\,\text{m}^{-3}$	k_{d3}	4432	$\text{N}\,\text{m}^{-3}$	Rittman (1982)
			$d_{b,min}$	0.003	m	Rittman (1982)

H

Reservoir - justification of assumptions

Reservoir model assumptions

While incorporating the reservoir to the HFM module model, a lot of additional assumptions needed to be made (see list in Chapter 6). These assumptions are justified in this section.

- The reservoir is ideally mixed and in a steady-state.

This can be assumed in stationary conditions and with adequate stirring in the reservoir. Biofilm formation at the reservoir walls should be prevented. In this case the average biomass growth rate μ equals the dilution rate of the reservoir.

- Reaction in the reservoir is considered to be negligible.

The volumetric ethanol productivity in the reservoir was calculated from the results obtained and compared with these in the biofilm and the in module liquid phase. The module volume-specific ethanol productivity in the biofilm and liquid was calculated according to Equation H.1, while the reservoir-specific ethanol productivity was calculated using Equation H.2. These productivities were calculated for the different values of the reservoir inflow rate, as this parameter was observed to have effect on the concentration and productivities in the module.

$$P_{V,EtOH,k} = \int_{0}^{V_k} q_{EtOH} c_{k,x} \mathrm{d}V_k M_{EtOH} \frac{N_f}{V_{\text{shell}}} \quad \text{with} \quad k = [b, l] \tag{H.1}$$

$$P_{V,EtOH,res} = q_{EtOH} c_{x,res} M_{EtOH} \tag{H.2}$$

From the calculated productivities (Figure H.1), can be derived that only at a low reservoir inflow rates (around 0.16 $\mathrm{mL\,min^{-1}}$), high reaction rates in the liquid phase of the module and in the reservoir were observed. This is due to the accumulation of compounds at low flow rates (Figure H.1b): CO accumulates in the liquid phase, as was also observed for ethanol 6.3. The accumulated CO can then be consumed, leading to reaction in the module liquid and reservoir. At higher reservoir inflow rates, the CO does not accumulate and is consumed in the biofilm. From flow rates lower than 0.09 $\mathrm{mL\,min^{-1}}$, the productivity decreases due to increased inhibitory effects of CO and ethanol. As there is still reaction taking place in the reservoir at these low flow rates and as the productivity is half of the value of that one in the biofilm, it should be taken into account at these low flow rates. However, at increased flow rates it could be neglected. Increased reservoir flow rates could remove the accumulated CO from the reservoir, or reaction in the reservoir should be taken into account in improved versions of the model.

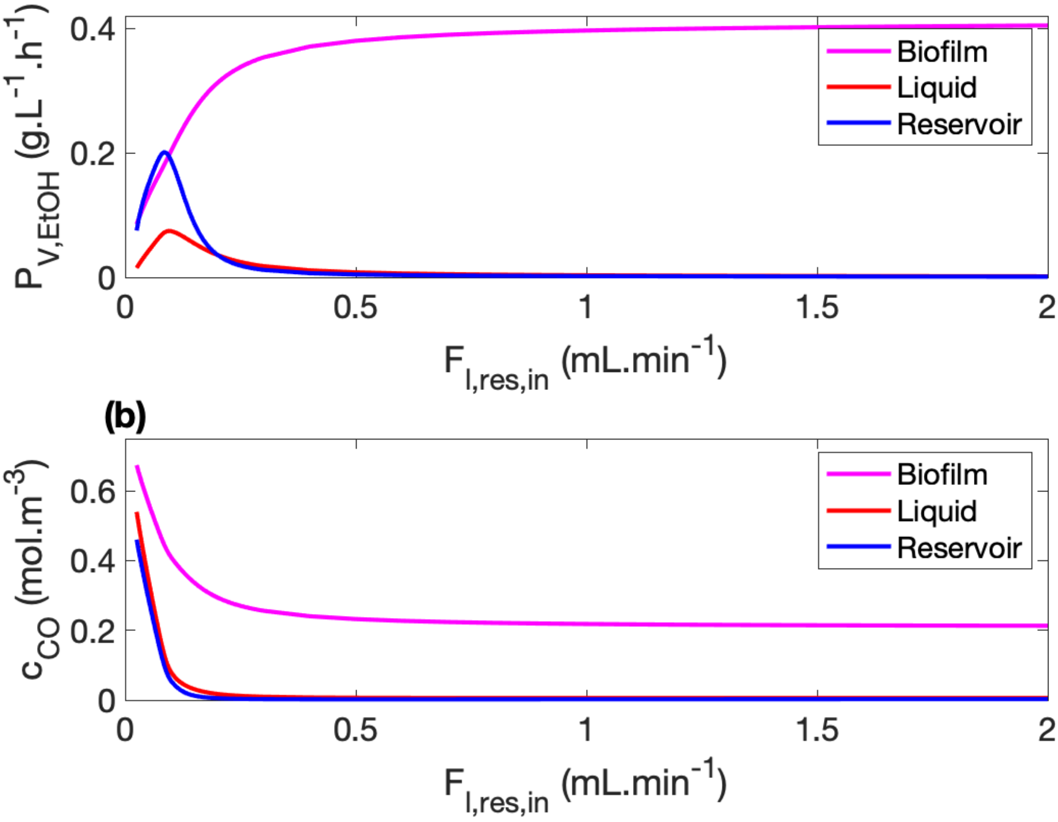

Figure H.1: For different values of the reservoir inflow rate, (a) the volume specific ethanol productivities are calculated for reaction in the biofilm, in the module liquid and in the reservoir. The volumes used for these calculations are the shell volume for the biofilm and liquid productivities and the liquid reservoir volume for the reservoir productivity. The reservoir inflow rate was varied using the same procedure as described in Chapter 6 (M_res_Flresin).

- The reservoir temperature remains constant at 37 °C.

The reservoir temperature can be controlled with the help of heat transfer equipment.

- The density of the liquid phase always equals the density of water.

The maximum concentration of ethanol obtained was around 35 $\mathrm{g\,L^{-1}}$. As the density of ethanol is lower than the one of water (789 $\mathrm{kg\,m^{-3}}$ at 20 °C vs.993.36 $\mathrm{kg\,m^{-3}}$ at 37 °C (Janssen and Warmoeskerken, 2006)), the density of the solution will become lower. However, a solution with 35 $\mathrm{g_{EtOH}\,L^{-1}}$ is estimated to have a density of 984 $\mathrm{kg\,m^{-3}}$ (Equation H.3). However, as the mixture volume is still unknown, the density of ethanol was used for that. But the resulting mixture density is just 1% below that of water and therefore this assumption was justified.

$$\rho_l = \frac{c_{l,EtOH,res}}{\rho_{mix}} \rho_{eth} + \left(1 - \frac{c_{l,EtOH,res}}{\rho_{mix}}\right) \rho_{H2O} = 984\,\mathrm{kg\,m^{-3}} \tag{H.3}$$

- The volume of the connecting pipes is neglected.

The volume of the connecting pipes was estimated according to Equation H.4. For the flow rate used (500 $\mathrm{mL\,min^{-1}}$), the average liquid velocity in the membrane module was calculated to be 6.667 $\mathrm{m\,s^{-1}}$. Assuming that the length of the pipes is 1 m and a tenfold higher liquid flow velocity through these pipes, then the pipe volume was calculated to be 0.125 L, which is 25% of the shell volume. This would lead to connecting pipes with a diameter of 1.26 cm, which is reasonable. However, this 25% is substantial for this extreme case. However, most simulations were performed at a lower flow rate (around 200 $\mathrm{mL\,min^{-1}}$), causing that the difference will become even lower.

$$V_{l,\mathrm{pipes}} = L_{\mathrm{pipes}} A_{c,\mathrm{pipes}} = L_{\mathrm{pipes}} \frac{F_{l,mod,in}}{v_{l,\mathrm{pipes}}} = L_{\mathrm{pipes}} \frac{F_{l,mod,in}}{10 v_{l,mod,in}} \tag{H.4}$$

- The reservoir inlet gas flow rate equals its outlet gas flow rate..

The volumetric gas flow rate leaving the reservoir was calculated for all simulations of the reservoir inlet gas flow rate using equation 2.39. In this equation, transport of CO, CO_2, N_2 and ethanol contributed to the corrected value of the gas outflow rate. Hereby, water evaporation was not taken into account as well as possible extra ethanol evaporation due to non-ideal behaviour. For different values of the inlet gas flow rate the outlet gas flow rate was plotted normalized according to the corresponding gas inflow rate (Figure H.5a).

In most cases the outflow rate is around 90-100% of the inflow rate. Only at very low inlet gas flow rates (between 1 and 10 $\mathrm{mL\,min^{-1}}$) the percentage is much lower, effectively the reservoir will be saturated with N_2. In these cases, this assumption could cause large problems as it is not realistic and reservoir off-gasses could therefore less accurately be predicted. However, as this is only in a small range of gas flow rates, it is justified to make this assumption in most of the cases. However, it should be noted that water and more ethanol could evaporate so that the relative amount of gas in the outlet should be somewhat higher than depicted in Figure H.5a).

- Non-ideal behaviour in the reservoir can be neglected.

As in the reservoir an ethanol-water mixture is present, non-ideal behaviour could be expected. The activity coefficient was calculated as a function of the ethanol concentration (Appendix E) and changed between 4.96 ($c_{l,EtOH,res} = 33.3\,\mathrm{g\,L^{-1}}$, when $F_{l,res,in} = 0.025\,\mathrm{mL\,min^{-1}}$) and 5.34 $c_{l,EtOH,res} = 1.72\,\mathrm{g\,L^{-1}}$, when $F_{l,res,in} = 2\,\mathrm{mL\,min^{-1}}$. So this should be taken into account when calculating the evaporation of ethanol and water. By considering the gas-liquid partition coefficient and considering the return stream after condensation, a negligible amount of ethanol is expected to be present in the gas outlet. Thus, it can be said that implementing the activity coefficient would not result in large differences in the ethanol concentration in the reactor system and can therefore be neglected.

- Water evaporation in the reservoir is neglected.

A condenser is used at the reservoir head space (at 4 °C) which returns the evaporated water (and ethanol) into the reservoir. For the gas outlet the fraction of water vapour was calculated. The water vapour pressure at at 4 °C is around at 812 Pa 812 Pa (Equation E.7). For the model with the changing reservoir gas flow rate, the influence of the water evaporation was determined. The fraction of water vapour in the gas outlet was calculated by dividing the water vapour pressure by the sum of the partial pressures in the reservoir gas outlet (which includes water) (Equation H.5). It was determined that on average, 0.82% of the gas outflow consisted of water, and could therefore be neglected in that case.

However, relative to the inflow of water to the reservoir, this could still be a substantial amount. The water evaporation rate was calculated with Equation H.5 (Figure H.5b) and divided by the reservoir inflow rate (0.2 $\mathrm{mL\,min^{-1}}$) (Figure H.5c). During operation with larger gas flow rates and low inflow rates (which

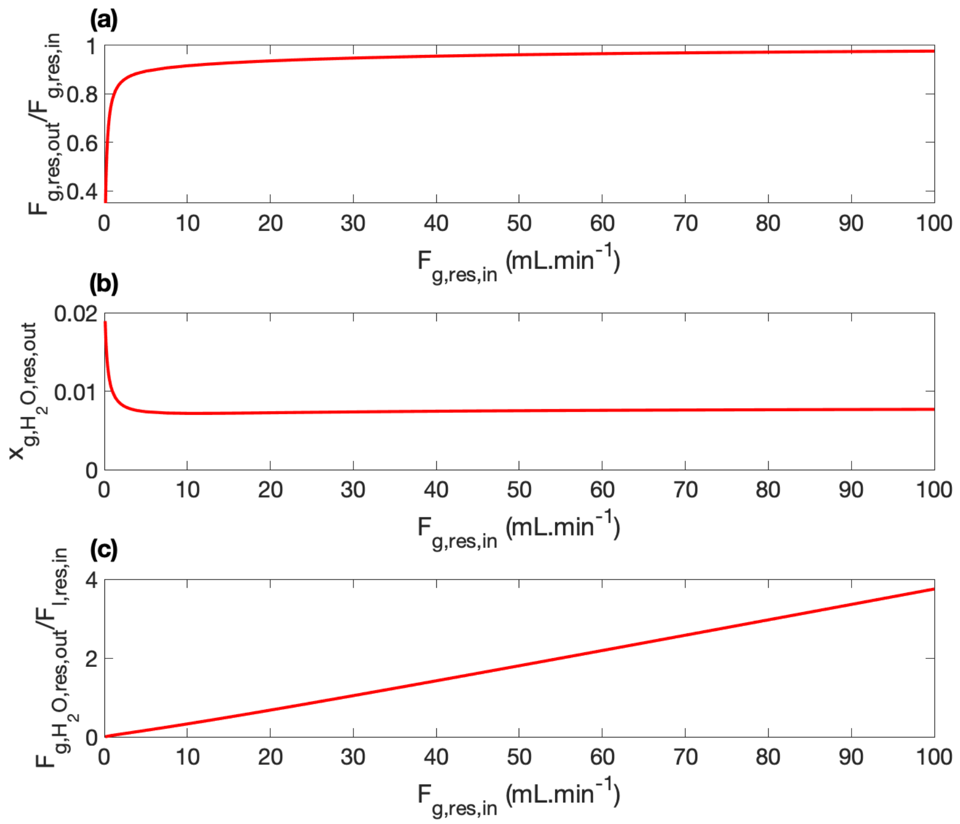

Figure H.2: For different values of the reservoir gas flow rate, (a) the amount of gas in the reservoir outflow was calculated as function of the amount in the inflow, using Equation 2.39, (b) the amount of water vapour in the reservoir gas outlet (with the condenser taken into account), and (c) the amount of water vapour in the reservoir gas outlet divided by a reservoir liquid inflow rate of 0.2 mL min^{-1}. The gas flow rate was varied using the same procedure as described in Chapter 6 (M_res_Fgresin).

is possible according to the operational window provided in Table 6.1), the water evaporation rate can almost become more than 3.5 times as large as the liquid inflow rate. This implies that during operation with low reservoir liquid inflow rates and high reservoir gas inflow rates, the volume of the reservoir needs to be controlled, even though the reservoir off-gas is condensed and returned.

$$F_{g,H_2O,res} = x_{g,H_2O,res,out} F_{g,res,out} = \frac{p_{sat,H_2O}}{\sum\limits_{i=1}^{n} p_{i,res}} F_{g,res,out} = 8.2 \cdot 10^{-3} F_{g,res,out} \tag{H.5}$$

- The volumetric mass transfer coefficient of the reservoir is assumed to be 30 h^{-1}.

This value of the volumetric mass transfer coefficient is representative for most lab-scale stirred tank reactors, which have also been used for syngas fermentation (Bredwell et al., 1999). However, the $\left(K_{L,i}a\right)_r es$ can easily be measured (by sparging with N2 and O2) and measuring the concentrations over time. For validating the model, the $\left(K_{L,i}a\right)_{res}$ should be measured and adjusted in the model.

- There is no nutrient limitation and pH can be controlled.

The ammonium requirements of the micro-organism was calculated, according to its consumption rate following the stoichiometry derived in Appendix F. This way, also the proton production rate was determined. The necessary concentration of dissolved NH_4Cl and NaOH (M_i = 53.49 and 40 g mol^{-1}) for the reservoir liquid inflow rate was calculated for different values of this inflow rate (Equation H.6) and plotted (Figure H.3).

From these results can be observed that 0.55 $\mathrm{g\,L^{-1}}$ of ammonium chloride and 0.4 $\mathrm{g\,L^{-1}}$ of sodium hydroxide are necessary to supply nutrients and to correct the pH, in the case of the maximum consumption rate that is achieved at a reservoir inflow rate of 0.08 $\mathrm{mL\,min^{-1}}$. These concentrations are achievable concerning the solubility of these compounds.

$$c_{l,i,res,in} = \left(\int_0^{V_b} q_i c_{b,x} dV_b + \int_0^{V_l} q_i c_{l,x} dV_l \right) \frac{M_i}{F_{l,res,in}} \quad \text{with} \quad i = [\mathrm{NH_4Cl}, \mathrm{NaOH}] \tag{H.6}$$

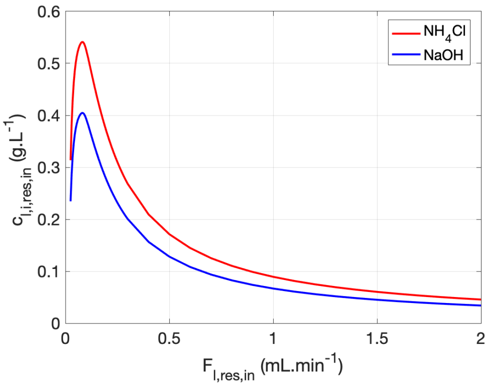

Figure H.3: For different values of the reservoir liquid inflow rate, the necessary supply of NH_4Cl and NaOH was calculated. The reservoir liquid inflow rate was varied using the same procedure as described in Chapter 6 (M_res_Flresin).

MATLAB script for solving mass balances

The MATLAB script for solving the concentrations in the reservoir liquid and partial pressure in the reservoir gas phases is given (Figure H.4). This script solves only for CO, but the resulting equations were modified for the other compounds (CO_2, N_2, ethanol). For biomass, there is no transport to the gas phase, the biomass balance was solved using the same mass balances but without transfer term to the gas phase.

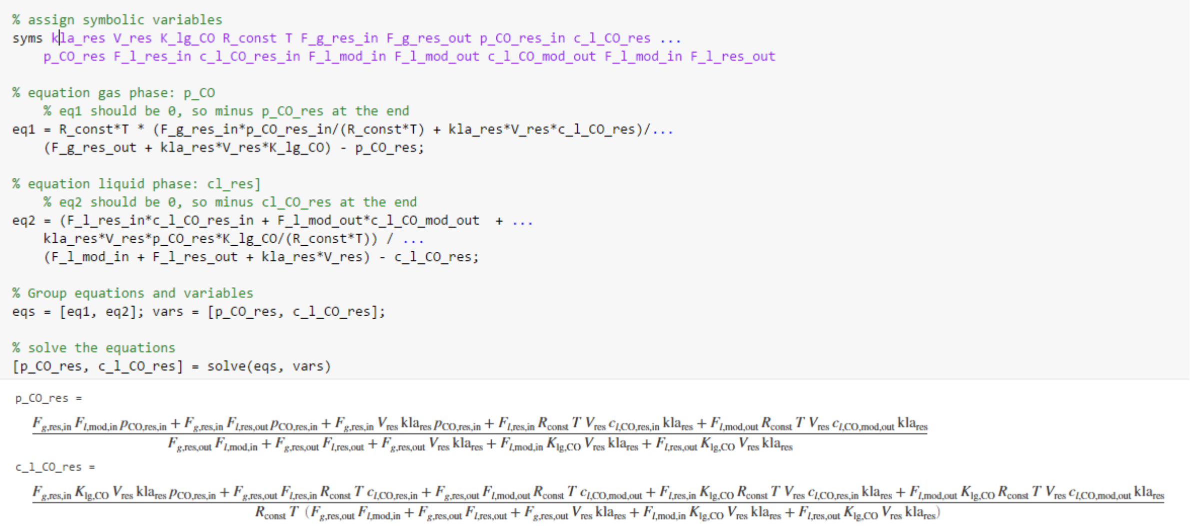

```
% assign symbolic variables
syms kla_res V_res K_lg_CO R_const T F_g_res_in F_g_res_out p_CO_res_in c_l_CO_res ...
    p_CO_res F_l_res_in c_l_CO_res_in F_l_mod_in F_l_mod_out c_l_CO_mod_out F_l_mod_in F_l_res_out

% equation gas phase: p_CO
    % eq1 should be 0, so minus p_CO_res at the end
eq1 = R_const*T * (F_g_res_in*p_CO_res_in/(R_const*T) + kla_res*V_res*c_l_CO_res)/...
    (F_g_res_out + kla_res*V_res*K_lg_CO) - p_CO_res;

% equation liquid phase: cl_res]
    % eq2 should be 0, so minus cl_CO_res at the end
eq2 = (F_l_res_in*c_l_CO_res_in + F_l_mod_out*c_l_CO_mod_out  + ...
    kla_res*V_res*p_CO_res*K_lg_CO/(R_const*T)) / ...
    (F_l_mod_in + F_l_res_out + kla_res*V_res) - c_l_CO_res;

% Group equations and variables
eqs = [eq1, eq2]; vars = [p_CO_res, c_l_CO_res];

% solve the equations
[p_CO_res, c_l_CO_res] = solve(eqs, vars)
```

```
p_CO_res =
```

$$\frac{F_{g,\mathrm{res},\mathrm{in}}\,F_{l,\mathrm{mod},\mathrm{in}}\,p_{\mathrm{CO},\mathrm{res},\mathrm{in}} + F_{g,\mathrm{res},\mathrm{in}}\,F_{l,\mathrm{res},\mathrm{out}}\,p_{\mathrm{CO},\mathrm{res},\mathrm{in}} + F_{g,\mathrm{res},\mathrm{in}}\,V_{\mathrm{res}}\,\mathrm{kla}_{\mathrm{res}}\,p_{\mathrm{CO},\mathrm{res},\mathrm{in}} + F_{l,\mathrm{res},\mathrm{in}}\,R_{\mathrm{const}}\,T\,V_{\mathrm{res}}\,c_{l,\mathrm{CO},\mathrm{res},\mathrm{in}}\,\mathrm{kla}_{\mathrm{res}} + F_{l,\mathrm{mod},\mathrm{out}}\,R_{\mathrm{const}}\,T\,V_{\mathrm{res}}\,c_{l,\mathrm{CO},\mathrm{mod},\mathrm{out}}\,\mathrm{kla}_{\mathrm{res}}}{F_{g,\mathrm{res},\mathrm{out}}\,F_{l,\mathrm{mod},\mathrm{in}} + F_{g,\mathrm{res},\mathrm{out}}\,F_{l,\mathrm{res},\mathrm{out}} + F_{g,\mathrm{res},\mathrm{out}}\,V_{\mathrm{res}}\,\mathrm{kla}_{\mathrm{res}} + F_{l,\mathrm{mod},\mathrm{in}}\,K_{\mathrm{lg},\mathrm{CO}}\,V_{\mathrm{res}}\,\mathrm{kla}_{\mathrm{res}} + F_{l,\mathrm{res},\mathrm{out}}\,K_{\mathrm{lg},\mathrm{CO}}\,V_{\mathrm{res}}\,\mathrm{kla}_{\mathrm{res}}}$$

```
c_l_CO_res =
```

$$\frac{F_{g,\mathrm{res},\mathrm{in}}\,K_{\mathrm{lg},\mathrm{CO}}\,V_{\mathrm{res}}\,\mathrm{kla}_{\mathrm{res}}\,p_{\mathrm{CO},\mathrm{res},\mathrm{in}} + F_{g,\mathrm{res},\mathrm{out}}\,F_{l,\mathrm{res},\mathrm{in}}\,R_{\mathrm{const}}\,T\,c_{l,\mathrm{CO},\mathrm{res},\mathrm{in}} + F_{g,\mathrm{res},\mathrm{out}}\,F_{l,\mathrm{mod},\mathrm{out}}\,R_{\mathrm{const}}\,T\,c_{l,\mathrm{CO},\mathrm{mod},\mathrm{out}} + F_{l,\mathrm{res},\mathrm{in}}\,K_{\mathrm{lg},\mathrm{CO}}\,R_{\mathrm{const}}\,T\,V_{\mathrm{res}}\,c_{l,\mathrm{CO},\mathrm{res},\mathrm{in}}\,\mathrm{kla}_{\mathrm{res}} + F_{l,\mathrm{mod},\mathrm{out}}\,K_{\mathrm{lg},\mathrm{CO}}\,R_{\mathrm{const}}\,T\,V_{\mathrm{res}}\,c_{l,\mathrm{CO},\mathrm{mod},\mathrm{out}}\,\mathrm{kla}_{\mathrm{res}}}{R_{\mathrm{const}}\,T\,\left(F_{g,\mathrm{res},\mathrm{out}}\,F_{l,\mathrm{mod},\mathrm{in}} + F_{g,\mathrm{res},\mathrm{out}}\,F_{l,\mathrm{res},\mathrm{out}} + F_{g,\mathrm{res},\mathrm{out}}\,V_{\mathrm{res}}\,\mathrm{kla}_{\mathrm{res}} + F_{l,\mathrm{mod},\mathrm{in}}\,K_{\mathrm{lg},\mathrm{CO}}\,V_{\mathrm{res}}\,\mathrm{kla}_{\mathrm{res}} + F_{l,\mathrm{res},\mathrm{out}}\,K_{\mathrm{lg},\mathrm{CO}}\,V_{\mathrm{res}}\,\mathrm{kla}_{\mathrm{res}}\right)}$$

Figure H.4: MATLAB script for solving the mass balances for the reservoir (Equations 2.38 and 2.41).

I

Parametric analyses - additional data

I.1. Influence of lumen gas and shell liquid pressure

CO partial pressure

The gas pressure was varied between 1 atm and 1.5 atm, with the CO inlet fraction always being 100%. It was expected that increasing the CO partial pressure would lead to higher mass transfer rates over the membrane and that would lead to higher reaction rates and thus higher productivities.

However, by increasing the gas pressure, it was observed that the productivity decreases (Figure I.1a), although slightly by $0.03\,\mathrm{g\,L^{-1}\,h^{-1}}$. This counter-intuitive phenomenon can be explained by the inhibition kinetics. At higher pressures, the CO transfer rate was indeed observed to be higher (Figure I.2). This means that more CO is available for reaction. But when more CO is converted, more ethanol is produced. As the reservoir ethanol concentration (Figure I.1b) and CO concentrations (Figure I.2c) were observed to increase, there will be more inhibition (Figure I.2b, Equation I.1) to cause a decrease in the productivity of the biofilm (Equation F.20, Figure F.6).

At a certain gas pressure, increasing the CO partial pressure does not lead to changes in the productivity or ethanol concentration. This can be explained by the maximum solubility of CO in water (Figure I.2c). When the pressure is higher than 1.35 atm, there is a difference between the relative amount of CO in the membrane and in the biofilm. In the model was imposed (with Equation 2.11) that the CO concentration in the liquid should become the maximum solubility in cases when there is more CO dissolved in the membrane than could be dissolved in the liquid.

By increasing the pressure, it was noticed that the consumption yield decreased. The decrease in consumption yield can be explained by the increased inhibition, and the increased mass transfer rate across the membrane due to the increased pressures. The total decrease in mass transfer yield is around 10% between 1.5 atm and 1 atm, which could be due to differences in driving force across the membrane. The consumption yield decreases as well with around 15%. At lower gas pressures, less CO enters the lumen than at higher pressures. Due to transfer to the gas phase, the velocity decreases inside the gas phase (Figure I.2d). At low CO pressures, the average velocity at the gas outlet is lower than at higher pressures. This lower gas velocity leads to a higher gas residence time, which could in turn lead to an increase in overall mass transfer yield.

It remains an interesting observation that increasing the pressure decreases the productivity of the organism. Additionally, the effect of another inhibition model (de Medeiros et al., 2019) was investigated for

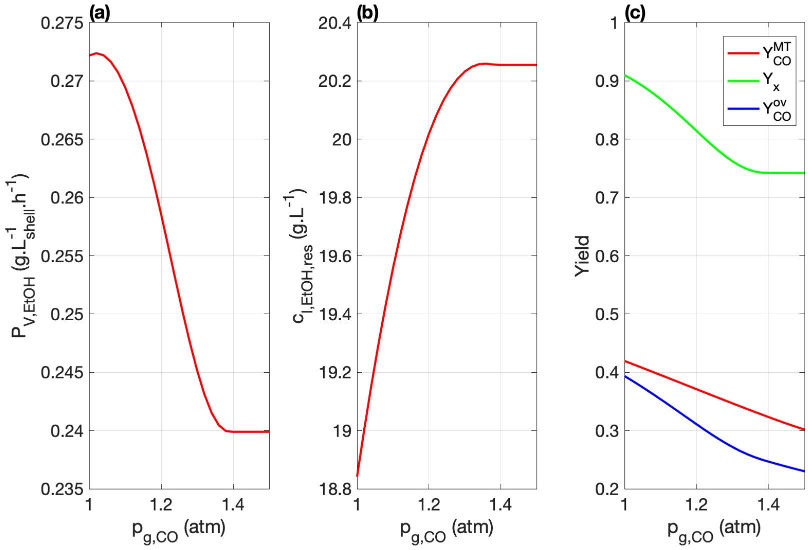

Figure I.1: For different values of the CO partial pressure in the gas phase, (a) the shell volume-specific ethanol productivity, (b) the ethanol concentration in the reservoir and (c) the different yields are calculated (M_param_Pgas). The gas pressure was varied between 1 and 1.5 bar. During these simulations other process parameters were kept constant according to their base values in Table 7.1.

this range of CO pressures (Figure I.3). Interestingly, in that case, increased gas pressures lead to increased productivities and highly increased ethanol concentrations (from 24 to 31 $\mathrm{g\,L^{-1}}$), which was expected to be due to the increased mass transfer rates. The CO can in this case be converted, which is not the case when a linear inhibition is used. These analyses prove that the inhibition model that is used can significantly influence the trends observed. As the gas pressure is a variable that can easily be adjusted, it could be used to derive which kind of inhibition model is valid for the organism (Chapter 8).

$$I_i^{av} = \frac{\int_0^{V_b} I_i \, \mathrm{d}V_b}{\int_0^{V_b} \mathrm{d}V_b} \quad \text{with} \quad i = [\mathrm{CO}, \mathrm{EtOH}] \tag{I.1}$$

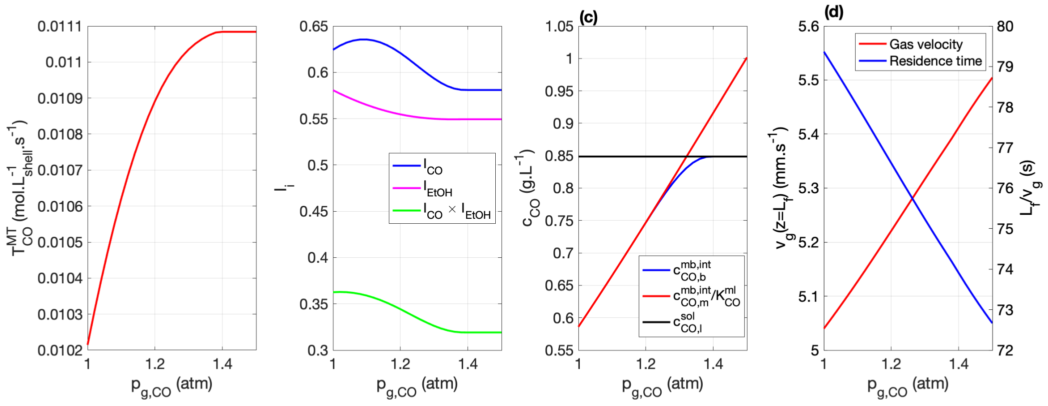

Figure I.2: Using the linear inhibition model, simulations were performed for different values of the CO partial pressure in the gas phase. (a) The CO mass transfer rate, (b) the inhibition constants of CO and ethanol, (c) the CO concentrations at the membrane biofilm interface and its solubility and (d) the gas flow velocity at the fibre outlet and the residence time, are plotted. The gas pressure was varied between 1 and 1.5 bar. During these simulations other process parameters were kept constant according to their base values in Table 7.1 (M_param_Pgas).

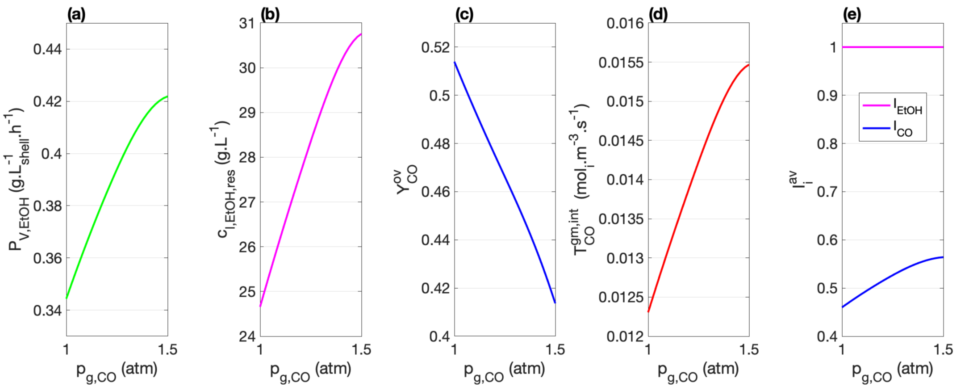

Figure I.3: Using the ethanol inhibition model of de Medeiros et al. (2019) simulations were performed for different values of the CO partial pressure in the gas phase. (a) The shell volume-specific ethanol productivity in the biofilm is calculated, (b) the concentration of ethanol in the reservoir, (c) the overall CO yield, (d) the CO mass transfer rate and the average inhibition constants for conversion in the biofilm. The gas pressure was varied between 1 and 1.5 bar, other process parameters were kept constant at their base value (Table 7.1) (M_param_Pgas_Inhib).

Liquid partial pressure

The pressure in the shell liquid phase was varied between 1 and 2 atm. The gas pressure was kept constant at 1.5 atm and 100% CO and with flow rate 20 mL min^{-1}. It was expected that higher liquid pressures would lead to a higher solubility of the dissolved gasses and therefore lead to higher concentrations of CO. This would therefore lead to more CO consumption and thus a higher productivity.

In contrast, there was a small decrease in the productivity observed (0.03 g L^{-1} h^{-1}) after increasing the pressure up to 1.2 atm. This slight increase in productivity also causes a decrease of the ethanol concentration from 20.25 to 19.3 g L^{-1} (Figure I.4a and b). The productivity and titer decrease imply that another compound than ethanol must be inhibitory in this case. Due to the increased liquid pressure, the solubility of CO in liquid increases and consequently, at increasing pressures up to 1.2 atm, the concentration of dissolved CO increases (Figure I.5b). This increase in CO concentration causes more inhibition and therefore hampers the productivity of the biofilm. This in turn leads to a decreasing ethanol concentration.

The influence of the liquid pressure on the productivity is in the same order of magnitude as the gas pressure or gas flow rate. As CO is inhibitory at higher concentrations, it can indeed be expected that, at higher CO concentrations in the biofilm, the productivity increase is smaller than increasing the pressure at lower CO concentrations. In terms of yield, there are some differences observed after increasing the liquid pressure: the consumption yield decreases with around 7%, meaning that more CO is entering the biofilm while it cannot be consumed. This means that substrate and product inhibition hamper the potential as all performance metrics decrease with increasing liquid pressures.

In order to analyse mass transfer across the membrane, the average CO concentrations along the fibre length in the membrane and biofilm were converted relative to gaseous pressures using the gas-liquid or gas-membrane partition coefficient and multiplying with RT (Figure I.5). From this can be seen that the maximum solubility indeed increases by increasing the liquid pressure (i.e. Henry's law). The concentration at the gas-membrane interface is on average around 1.32 atm, which is lower than the 1.5 bar gas pressure, due the the influx of other compounds to gas phase (water, CO_2, N_2). The dissolved amount in the biofilm then reaches the amount of CO present in the membrane when the liquid pressure is higher than 1.15 atm. Due to the membrane, there is a loss of CO pressure of 0.15 atm. By using a thinner dense membrane, this difference can be decreased, which could increase the productivity of the micro-organism when operating at higher liquid pressures.

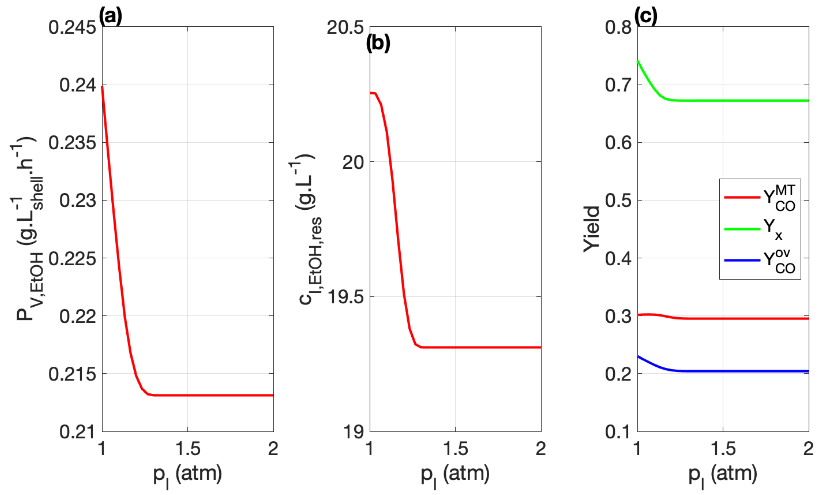

Figure I.4: For different values of the liquid pressure, (a) the shell volume-specific ethanol productivity, (b) the ethanol concentration in the reservoir and (c) the different yields are calculated (M_param_Pliq). The liquid pressure was varied between 1 and 2 atm. During these simulations other process parameters were kept constant according to their base values in Table 7.1.

One should note that it is important to take into account that at lower liquid pressures there is a large gap between the concentration in the membrane and the biofilm at the biofilm-liquid interface. This gap is due to Equation 2.11. This boundary condition was used as it is unknown whether bubble formation would occur in the liquid phase or in the biofilm. Thus, experiments should determine the validity of this boundary condition.

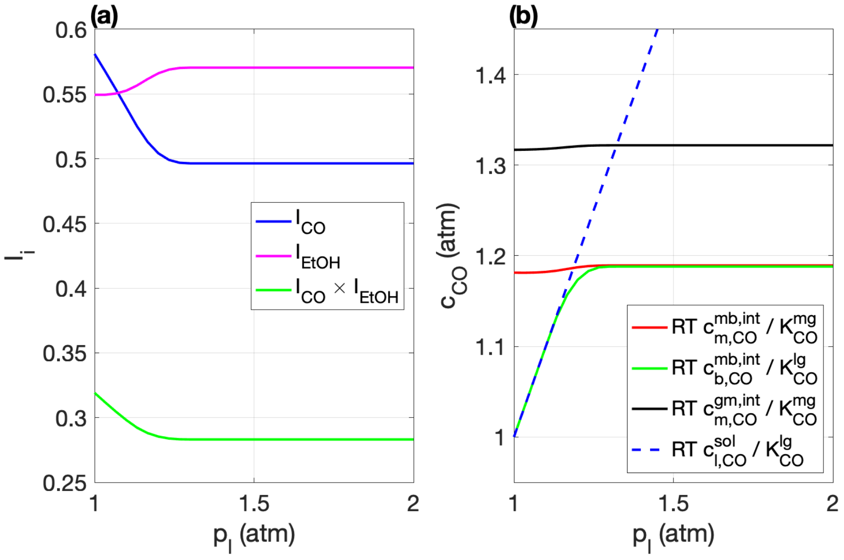

Figure I.5: For different values of the liquid pressure (a) the inhibition constants of CO, ethanol and the product of both, are plotted, as well as (b) different concentrations of CO (in atm). The red line displays the concentration at the membrane-biofilm interface in the membrane, the green one the concentration at this interface but in the biofilm, the black one is the concentration in the gas phase, while the dashed-blue line is the maximum solubility. The liquid pressure was varied between 1 and 2 atm. During these simulations other process parameters were kept constant according to their base values in Table 7.1 (M_param_Pliq).

I.2. Additional figures sensitivity analysis

In Figures I.6 and I.7, the results of the sensitivity analysis for the biofilm thickness and its biomass concentration are provided, in terms of the ethanol concentration in the reservoir and the overall CO yield. These results follow the same pattern as for the volume-specific ethanol productivity, (Chapter 7).

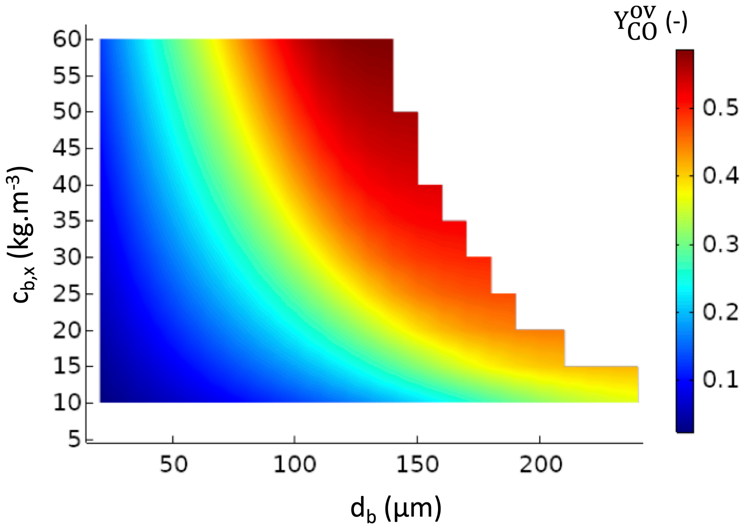

Figure I.6: Sensitivity analysis for the biofilm thickness d_b and its biomass concentration $c_{b,x}$. These parameters were varied between 20 and 240 µm, and 10 and 60 g L^{-1}, respectively. The overall CO yield was calculated for each simulation (Equation 7.3. During these simulations, the process parameters were kept constant at their base value (Table 7.1) (M_sens).

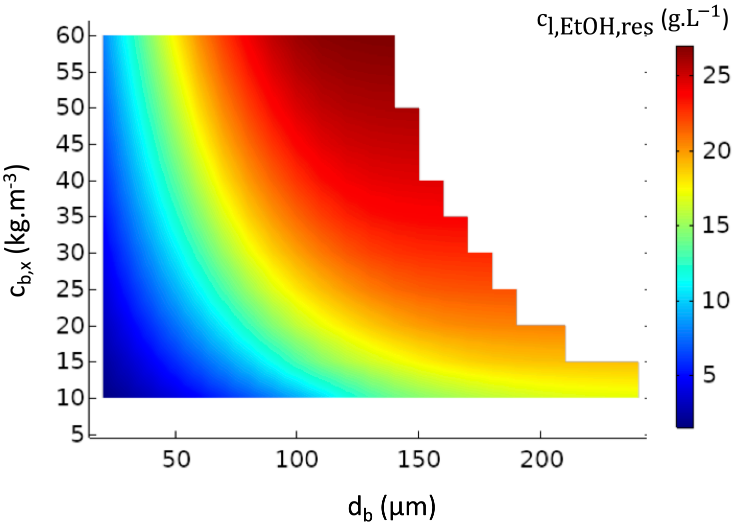

Figure I.7: Sensitivity analysis for the biofilm thickness d_b and its biomass concentration $c_{b,x}$. These parameters were varied between 20 and 240 µm, and 10 and 60 g L^{-1}, respectively. The ethanol concentration in the reservoir was calculated for each simulation. During these simulations, the process parameters were kept constant at their base value (Table 7.1) (M_sens).